ADSORPTION OF SIMPLE MOLECULES ON GRAPHITE: A COMPUTER SIMULATION STUDY—

by

© Michael Allan Moller, B.Sc.

A Thesis

Submitted to the School of Graduate Studies

in Partial Fulfilment of the Requirements

for the Degree

Doctor of Philosophy

McMaster University

(September 1988)

SIMPLE MOLECULES PHYSISORBED ON GRAPHITE

DOCTOR OF PHILOSOPHY (1988) McMASTER UNIVERSITY

Hamilton, Ontario

TITLE: Adsorption of Simple Molecules on Graphite: A Computer Simulation Study

AUTHOR: Michael Allan Moller, B.Sc. (University of Waterloo)

SUPERVISOR: Professor Michael L. Klein

NUMBER OF PAGES: xiii, 147

Abstract

The structure and dynamics of monolayers of the simple hydrocarbon molecules CH_4, C_2H_4 and C_2H_6, physisorbed on graphite, have been explored by computer simulation, along with the behavior of corrugated bilayer systems of the dipolar molecules CH_3F and CH_3Cl on Xe/graphite.

The simulations found that the corrugation of the surface can have a strong effect on the monolayer structures of these molecules. The experimentally observed phases of C_2H_6 and CH_3F were found to be stabilized by the surface corrugation, though C_2H_4 and CH_3Cl were not. The structure of CH_3Cl/Xe/graphite was found to be an array of vertically aligned anti-ferro ordered pairs of molecules arranged in rows on the surface, while CH_3F/Xe/graphite formed zig-zag chains lying flat on the surface.

The dynamics of these layer systems was also examined. In each case, the calculated power spectra agreed well with experiment, and showed strong evidence for translation-rotation coupling in the monolayers. The motions of CH_3F and CH_3Cl were particularly coupled to the motions of the underlying Xe layer.

Simulations of the melting of ethylene suggest a novel mechanism: the molecules create locally enhanced density fluctuations necessary for melting by standing up from the surface, smearing the transition, and making it appear continuous.

Calculated diffusion constants in the liquid phase for methane on graphite agreed well with experiment. Similar calculations of liquid ethylene did not agree as well with experiment, possibly because of an inadequate potential.

Acknowledgements

I would like to express my appreciation to my supervisor, Dr. M. L. Klein, who has helped me tremendously throughout my thesis study with his enthusiasm and support, and for his much needed assistance with the more difficult aspects of the theory.

Other people I would like to acknowledge for their help are Shuichi Nosé and Roger Impey, who taught me the details of the molecular dynamics technique, Séamus O'Shea for his help with the corrugated surface potential, and the late Professor J.A. Morrison, who was like a second supervisor to me.

I would like to give my heartfelt thanks to my wife, Carol, whose support and encouragement kept me going when it was tough.

Finally, I would like to express my gratitude to the National Sciences and Engineering Research Council and the Ontario Government, for their financial assistance, in the form of scholarships.

for my parents

Contents

List of Tables

List of Figures

Chapter 1

Introduction

The topic of adsorption of atoms and molecules on surfaces is divided into the two broad classes of physisorption and chemisorption. In general terms, they can be described as follows. Physisorption is reversible and the strengths of the bonds between the adsorbate molecules and the substrate are of the order of those exhibited between the adsorbate molecules in their condensed phases. In contrast, chemisorptive bonding is much stronger, being comparable to the bonding between the atoms of a molecule, and is specific to the chemical species (only certain molecules can chemisorb onto certain substrates). This bonding makes it irreversible, where adsorption and/or desorption results in chemical changes in either the adsorbate or the substrate. For example, adsorbed O_2 on carbon, when heated, does not desorb. Instead, a mixture of CO and CO_2 is released. The distinction between these two types of adsorption is only clear in their extremes, and a system can show a mixture of physisorptive and chemisorptive behavior. Research on adsorbed layers has tended

to concentrate on these extremes, in order to facilitate their understanding.

All substrates have structure, whether it be the arrangement of their atoms on exposed crystal faces or the arrangement of the crystals themselves. This heterogeneity makes both types of adsorption site-preferential, in that the possible adsorption sites have a range of energies; the sites of lowest energy being preferred. These sites, then, create barriers to lateral motion between them. In the case of chemisorption, these barriers are high, and in the limit of low adsorbed layer density (coverage), the system can be approximated by a two-dimensional (2-D) lattice gas. In contrast, the barriers to lateral motion in a physisorbed system are low, and at low coverage, it can be approximated by a 2-D ideal gas. At higher coverages, the interactions between adsorbed molecules become important. In general, for physisorbed layers, they are greater in magnitude relative to the interactions with the substrate than for chemisorbed layers, and thus more important in determining their structure than in chemisorbed layers. In both cases, the mean square displacements of the adsorbed molecules normal to the surface are often small enough that a 2-D approximation for these systems is reasonable.

The relatively weak interaction between a physisorbed layer and its substrate means that its molecules are essentially unchanged from their states in three-dimensional (bulk) systems. This makes physisorption particularly interesting, for physisorbed monolayers not only behave essentially as 2-D systems, but have phases corresponding to solids, liquids and gases of bulk systems. Phenomena such as crystal growth and phase transitions (eg: melting), are easier to understand in such 2-D systems than in bulk. Also, simpler mathematical models can be used to describe

these phenomena in 2-D.

Therefore, for the study of a pseudo 2-D physisorbed system, the ideal substrate would have the following characteristics. It would only weakly interact with the adsorbate, it would be flat, and it would be homogeneous (a single plane extending infinitely in 2-D). Perhaps the substrate which comes closest to this description is graphite. Its layered structure leads to the exposure of mainly a single crystal face (the basal plane), making it a nearly homogeneous substrate, even in powder form. Also, natural single crystals of graphite are available which have few defects and large surface area. The graphite basal plane also has a small corrugation (it is nearly flat), reducing the effect of the substrate on the properties of the physisorbed layer. Finally, graphite is easy to model, either as a flat or corrugated surface, since the simulation can be done on a single perfect crystal face, without it being too different from the experiment. It would not be easy to simulate a surface with defects (pores, steps), since the small system size in simulations precludes a good sampling of defect size distributions. For these reasons, graphite is one of the most often used substrates in physisorption studies.

Single layers of rare gases adsorbed on graphite have already been extensively studied[1,2,3]. A number of studies, both experimental and simulation, have been carried out on such gases as Ar[4], Kr[5] and Xe[6]. Small polyatomic molecules, due to their extra degrees of freedom (rotations), have more interesting dynamics than rare gas systems. For example, one can examine the coupling between translations and rotations. Modelling of small molecules can be simplified by assuming they are rigid, since their intramolecular motions are decoupled from the intermolecular mo-

tions. The high frequencies of the former require a very small time step in simulation, and since they have little effect on the latter, they are often omitted from a model. Linear molecules, for example N_2, CO, C_2H_2[7] and O_2[8], have already been well studied, so this thesis will look at small non-linear molecules adsorbed on graphite.

Hydrocarbons are a natural choice for adsorption studies, because their hydrogen atoms have a large cross-section for incoherent neutron scattering. Also, the deuterated forms have a large cross-section for coherent neutron scattering. This is important in an adsorbed layer, where the scattering signal is weak, due to the small number of scatterers, as compared to a bulk sample. In other experimental techniques, this problem can be overcome by the use of an enhanced incident beam or detection system. For example, X-ray scattering can be performed using a synchrotron source. Low energy electron diffraction (LEED), and atom-beam diffraction techniques only examine the top layer of a system (although in LEED there is a small contribution from the second layer), so these methods are commonly used to study physisorbed layers. Therefore, it is possible to get good experimental data on hydrocarbon layers, which can be complemented by and compared to simulation.

Computer simulation molecular dynamics (MD), or Monte Carlo (MC) calculations are particularly suited to the study of physisorbed molecular systems. Such simulations can give additional details about the structures of the various phases which are not readily obtainable from diffraction experiments. In combination with scattering and thermodynamic experiments, computer simulation is a powerful technique for the study of physisorbed systems.

As a result, this thesis reports simulation results for a number of small hy-

drocarbons physisorbed on graphite. The molecules chosen for study were: CH_4, C_2H_4, C_2H_6, CH_3F and CH_3Cl. Each of these molecules has special interest specific to itself, but they also fit into a larger theme: increasing dimensionality and complexity but with a strong similarity in interaction potential and size. In this way, the subtle differences in properties of adsorbed layers due to molecular shape could be examined.

There has been a significant amount of effort, both experimental and theoretical, to characterize the phases of simple molecules adsorbed on graphite, and to construct the corresponding phase diagrams. To date a wide variety of structures have been identified. Much of this diversity in structure is due to the shape of the adsorbed molecule, and molecules with similar shapes often produce similar structures and similar phase diagrams. For example, small, non-spherical molecules such as N_2[9], C_2H_4[10], C_2H_6[11], C_2N_2[12] and C_6H_{14}[13] all form herringbone structures on graphite at low coverages. For molecules with strong multipolar interactions like N_2 and C_2N_2, the herringbone structure arises from the electrostatic quadrupole-quadrupole interactions, whereas for the hydrocarbons, it is a consequence of the aspherical shape.

In general, these structures are not only dependent on the shape of the molecules, but also on the relative strengths of the intermolecular and molecule-surface potentials. However, it is surprising that the herringbone structure is by far the most common for non-spherical molecules[14]. Therefore, it is of interest to try and rationalize these structures in terms of the fundamental interactions between molecules, and in this thesis, this is has been done through the use of computer sim-

ulation. The organization of the thesis is as follows: computer simulation techniques and interaction potentials are outlined in Chapter 2. The results for each molecule of interest are presented in separate chapters: methane/graphite in Chapter 3, ethylene/graphite in Chapter 4, ethane/graphite in Chapter 5, and then methyl fluoride and methyl-chloride on Xe/graphite in Chapter 6. A brief summary and some conclusions are presented in Chapter 7.

Chapter 2

Computer Simulation Technique

2.1 Introduction

This chapter presents a brief outline of the computer simulation technique used in this thesis, namely molecular dynamics. Molecular dynamics is only one of several simulation techniques currently in use by theoreticians. Its advantage over such techniques as Monte Carlo is that it can be used to study both static and dynamic properties of a system, with only one major assumption: the form of the interaction potentials, both intermolecular and molecule-surface. These potentials are discussed in detail in the second half of the chapter.

The MD computer program used in this project was originally written by Shuichi Nosé[10] for ethylene on a flat model of graphite. In this project, therefore, the program was modified to include the graphite corrugation. This is discussed in detail in Sections 2.3.2 and 2.3.3.

2.2 Molecular Dynamics

The MD technique has been summarized in detail in a number of excellent review articles[15,16,17,18,19] and a recent monograph[20]. The basic idea of MD is to determine the properties of a system by explicitly calculating the motions of all its particles. Essentially, the task is to solve Newton's equations of motion for an N-particle system. In systems of chemical interest, N is greater than 2, so the equations cannot be solved analytically. Instead, one must use a numerical procedure to integrate the equations of motion. There are several different procedures available, and each has its advantages and disadvantages. The choice depends on the type of molecule to be simulated, and on the characteristics of the computer to be used. The following section is a brief overview of the various algorithms currently in use.

2.2.1 Integration Techniques

If one considers a system of interacting particles such as rare gas atoms, then a MD simulation of this system involves the solution of the second-order differential equation

$$m_i \frac{\mathrm{d}^2 \mathbf{r_i}}{\mathrm{d}t^2} = \sum_{j \neq i} \mathbf{F}(r_{ij}), \qquad r_{ij} = |\mathbf{r_i} - \mathbf{r_j}| \tag{2.1}$$

for each particle, where m_i is the mass of particle i, $\mathbf{r_i} = (x_i, y_i, z_i)$ is its position, and $\mathbf{F}(r_{ij})$ is the force exerted on i by particle j at a distance of r_{ij}. These equations can be integrated stepwise forward in time, using a time interval Δt. Therefore, after n integration steps, the evolution of the system will have been followed for a time $t^n = n(\Delta t)$. The initial positions and velocities can be specified in a number of

ways. In this thesis, the starting positions were chosen so as to reproduce a particular solid structure, depending on the molecule to be studied. The velocities were chosen randomly, but were constrained to the Maxwell-Boltzmann velocity distribution corresponding to the temperature of interest.

A simple solution for the equations of motion would be a Taylor series relating the positions of the particles at step $n+1$ ($\mathbf{r}_i^{n+1}$) to their positions at step n ($\mathbf{r}_i^n$), adjusted for their velocities ($\mathbf{v}_i^n$) and for the net force acting on them at step n:

$$\mathbf{r}_i^{n+1} = \mathbf{r}_i^n + \mathbf{v}_i^n \Delta t + \frac{1}{2}\mathbf{f}_i^n (\Delta t)^2 \tag{2.2}$$

$$\mathbf{v}_i^{n+1} = \mathbf{v}_i^n + \mathbf{f}_i^n \Delta t \tag{2.3}$$

where $\mathbf{f}_i^n = \sum_{j \neq i} \mathbf{F}^n(r_{ij})/m_i$, and $\mathbf{F}^n(r_{ij})$ is the value of $\mathbf{F}(r_{ij})$ at step n. This method assumes the net forces on the particles remain constant throughout their moves from $\mathbf{r}_i^n$ to $\mathbf{r}_i^{n+1}$, and therefore requires a very small timestep Δt to get accurate trajectories. One solution to this problem is to use a better expansion:

$$\mathbf{r}_i^{n+1} = 2\mathbf{r}_i^n - \mathbf{r}_i^{n-1} + \mathbf{f}_i^n (\Delta t)^2 \tag{2.4}$$

$$\mathbf{v}_i^n = (\mathbf{r}_i^{n+1} - \mathbf{r}_i^{n-1})/2\Delta t \tag{2.5}$$

obtained from addition of the Taylor series expansions for $\mathbf{r}_i^{n+1}$ and $\mathbf{r}_i^{n-1}$. This method is known as the Verlet algorithm[21]. The calculation of the velocities in the Verlet algorithm is one step behind the calculation of the positions. This could be a problem in constant pressure simulations, which require both the positions and velocities at the same time. Recent modifications to the Verlet algorithm have successfully overcome this problem[22,23].

The Verlet algorithm is second-order in Δt. However, it is equivalent to a third-order method, since in the expansion, the term in $(\Delta t)^3$ vanishes. Available higher order methods include the Runge-Kutta and the predictor-corrector. In MD simulations, the calculation of the force is by far the most laborious part, so methods which require more than one force evaluation per step are not very practical. This eliminates the Runge-Kutta and multiple step predictor-corrector techniques. The most efficient of these higher order algorithms is the so-called Gear algorithm[24], which is a predictor-corrector with only a single force evaluation per step.

In the Gear algorithm of order w, using the Nordsieck or *N-representation*, the positions of the particles and their w time derivatives at step n are kept in the computer memory in a column vector:

$$\underline{\mathbf{r}}_i^n = (\mathbf{r}_i^n, \Delta t(\dot{\mathbf{r}}_i)^n, \tfrac{1}{2}(\Delta t)^2(\ddot{\mathbf{r}}_i)^n, \ldots) \tag{2.6}$$

The algorithm moves the particles in the following manner. First, $\underline{\mathbf{r}}_i^n$ is used to calculate predicted positions and derivatives $\underline{\mathbf{s}}_i^{n+1}$:

$$\underline{\mathbf{s}}_i^{n+1} = \underline{\mathbf{A}}\,\underline{\mathbf{r}}_i^n, \tag{2.7}$$

where $\underline{\mathbf{A}}$ is a matrix of coefficients for the prediction step. The net acceleration of a particle $\mathbf{f}_i^{n+1}$ due to interaction with its neighbours is then calculated, and can be compared to $(\ddot{\mathbf{s}}_i)^{n+1}$, the predicted value of the acceleration. The difference between them is a measure of the error in the predictor step, and is used to correct the predicted position:

$$\underline{\mathbf{r}}_i^{n+1} = \underline{\mathbf{s}}_i^{n+1} + \underline{\mathbf{a}}\tfrac{1}{2}(\Delta t)^2(\mathbf{f}_i^{n+1} - (\ddot{\mathbf{s}}_i)^{n+1}), \tag{2.8}$$

where $\mathbf{a}$ is a matrix of coefficients for the correction step. The optimum values of $\mathbf{A}$ and $\mathbf{a}$ have been tabulated by Gear[24], and are also summarized in a review by Berendsen and van Gunsteren[19]. In this thesis, a fifth-order algorithm was used to calculate the centre of mass motions of the molecules.

2.2.2 Characteristics of the MD Simulation

One of the limitations to MD simulations is the available computer memory. As a result, on most modern computers, the maximum number of molecules in a simulated system using the Gear predictor-corrector algorithm is about 1000. Such a small system would exhibit strong surface effects, which might be undesirable in the simulation. In order to simulate a macroscopic system, periodic boundaries are used. In this technique, the simulation system is confined to a box surrounded by images of itself; eight of them for a pseudo-2D system. In this way, a molecule at the edge of the box is surrounded by a complete set of neighbors. Care is taken that the molecules only interact with the nearest images of their neighbors, so that they are not unduly influenced by the periodicity of the box images. Thus, a small simulation can emulate a large-scale system, without boundaries.

The other major limitation to computer simulation is execution time, which must be kept to a minimum. If all of the molecules are allowed to interact, the calculation time will be proportional to N^2, where N is the number of molecules. Since the potential between hydrocarbon molecules is the short-ranged van der Waals interaction, this potential was cut off at 10Å, beyond which the interaction was assumed to be zero. A list of neighbors within this cut-off distance was kept for each

molecule, and the net force on the molecule was calculated only from molecules on this list. The list was updated every 25 steps. In this way, the calculation time was reduced to approximately proportional to N, since each molecule now had a small, nearly fixed number of interactions. However, as a molecule enters or leaves the area within the cut-off radius of one of its neighbors, it experiences a discontinuous jump in both the potential and the force. This results in small fluctuations in the calculated total energy of the system, which should be constant in the microcanonical ensemble. These fluctuations are random, and do not affect the dynamics of the system unless the cut-off radius is set too small.

To reduce the time needed to calculate the net force on a particle, it is important to use a form of the potential which can be rapidly evaluated. One way is to use a simple form which has been fitted to the full potential. Also, with the advent of vector and parallel computers, the full potential can be approximated by a polynomial expression, which is quickly evaluated by these machines. The intermolecular potentials are discussed in more detail in Sec. 2.3.

In the extension of the MD method to rigid molecules of arbitrary shape, the interactions between molecules are assumed to be the sum of individual atom-atom potentials between the atoms of the molecules. To simplify the calculations, the positions of the individual atoms of a molecule are stored in the so-called molecule-fixed frame. The origin of the coordinate system in this frame is the centre of mass of the molecule, and the axes are chosen to coincide with the principle axes of the molecule, so that the off-diagonal elements of the moment of inertia tensor are zero. In this frame, the coordinates of the atoms are the same for each molecule (since they

are rigid), and the positions of the atoms in the space-fixed frame (the simulation box) can be easily calculated from the orientations of the molecules in the space-fixed frame. The net force acting on a molecule's centre of mass is calculated from the vector sum of the forces acting on its atoms. The equation of motion for the centre of mass is then solved as for a rare gas atom above. The rotational motions are considered separately.

In this thesis, the calculation of these motions used quaternions[25] instead of Euler angles to specify the orientation of the molecule-fixed frame for each molecule. This is because the equations of motion from Euler angles have a singularity at $\theta = 0$ which is eliminated by the use of quaternions. The quaternions are defined as follows:

$$\chi = \cos(\theta/2) \cdot \cos(\psi + \phi)/2 \tag{2.9}$$

$$\eta = \sin(\theta/2) \cdot \cos(\psi - \phi)/2 \tag{2.10}$$

$$\xi = \sin(\theta/2) \cdot \sin(\psi - \phi)/2 \tag{2.11}$$

$$\zeta = \cos(\theta/2) \cdot \sin(\psi + \phi)/2 \tag{2.12}$$

Here the Goldstein definitions of the Euler angles ϕ, θ and ψ have been used[26].

The angular velocity of each molecule was calculated in the molecule-fixed frame. The net torque acting on each molecule was calculated from the sum of the torques exerted on each atom, and used to modify the angular velocities:

$$\omega_i(t + \Delta t) = \omega_i(t) + \frac{1}{\mathbf{I_i}}\mathbf{N_i}(t)\Delta t \tag{2.13}$$

where $\mathbf{N_i}$ is the net torque acting on atom i with moment of inertia tensor $\mathbf{I_i}$, where $\mathbf{N_i}/\mathbf{I_i} = N_{i\lambda}/I_{i\lambda\lambda}$, where λ is one of the axes in the molecule-fixed frame. The angular

velocities were then used to calculate the time derivatives of the quaternions:

$$\begin{pmatrix} \dot{\xi}_i \\ \dot{\eta}_i \\ \dot{\zeta}_i \\ \dot{\chi}_i \end{pmatrix} = \frac{1}{2} \begin{pmatrix} -\zeta_i & -\chi_i & \eta_i & \xi_i \\ \chi_i & -\zeta_i & -\xi_i & \eta_i \\ \xi_i & \eta_i & \chi_i & \zeta_i \\ -\eta_i & \xi_i & -\zeta_i & \chi_i \end{pmatrix} \begin{pmatrix} \omega_{ix} \\ \omega_{iy} \\ \omega_{iz} \\ 0 \end{pmatrix} \tag{2.14}$$

where ω_{ix}, ω_{iy} and ω_{iz} represent the angular velocities about the three principal axes of molecule i. Finally, the fourth-order Gear algorithm was used to calculate the values of the quaternions at each simulation step.

Molecular dynamics simulations are not limited to the microcanonical ensemble. Indeed, it is useful to simulate systems at constant temperature, pressure, or chemical potential. The constant temperature and constant pressure techniques are described below. Simulation of the grand canonical ensemble involves adding a MC step for the addition or deletion of a molecule from the system during a MD run[27].

The technique for simulating the isobaric (constant pressure) ensemble with MD was pioneered by Andersen[28]. His formulation adds an extra degree of freedom to the simulated system by allowing it to isotropically expand or contract in response to the difference between an externally applied pressure P_{ex} and the internal pressure due to the interaction between the particles. The particle positions are scaled by the MD cell length $L = V^{1/3}$:

$$\mathbf{q_i} = \mathbf{r_i}/L, \qquad 0 \leq \mathbf{q_i} \leq 1, \tag{2.15}$$

where $\mathbf{r_i}$ is the position in real units. Since L is allowed to fluctuate, terms for its kinetic and potential energy must be included in the Hamiltonian:

$$H = \sum_i \frac{\mathbf{p_i}^2}{m_i L^2} + U(L\mathbf{q}) + \frac{p_v^2}{2W} + P_{ex}V. \tag{2.16}$$

Here, p_v is the conjugate momentum of V, so $p_v^2/2W$ represents the kinetic energy of the box fluctuations, where W is an adjustable parameter controlling the rate of fluctuation, and can also be thought of as a mass of a piston acting isotropically on the system. Also, $U(L\mathbf{q})$ is the total potential energy of the system, and is equal to the sum of the interparticle pair potentials: $U(L\mathbf{q}) = \sum_{i<j} u(r_{ij})$, where $\mathbf{F}(r_{ij}) = -\partial u(r_{ij})/\partial r_{ij}$. Here, $u(r_{ij})$ is the interaction potential between two particles i and j (see Sec. 2.3). The resulting equations of motion are:

$$\frac{d\mathbf{q_i}}{dt} = 2\mathbf{p_i}/m_i L^2 \tag{2.17}$$

$$\frac{d\mathbf{p_i}}{dt} = -\partial U/\partial \mathbf{q_i} \tag{2.18}$$

$$\frac{dV}{dt} = p_v/W \tag{2.19}$$

$$\frac{dp_v}{dt} = \frac{\sum_i \mathbf{p_i}^2}{3Vm_iL^2} - \frac{\sum_i \mathbf{q_i}\cdot(\partial U/\partial \mathbf{q_i})}{3V} - P_{ex}. \tag{2.20}$$

This method cannot be used for anisotropic systems such as solids. For such a system, the MD cell must be allowed to change its shape in response to internal stresses. This method has been worked out by Parrinello and Rahman[29,30,31,32]. Here, the vectors $\mathbf{L_1}$, $\mathbf{L_2}$ and $\mathbf{L_3}$, representing the sides of the MD cell are collected in the matrix $\mathbf{h}$, so $V = \mathbf{L_1}\cdot\mathbf{L_2}\times\mathbf{L_3} = \det \mathbf{h}$. The particle positions are scaled: $\mathbf{r_i} = \mathbf{h}\mathbf{q_i}$, where $0 \le \mathbf{q_i} \le 1$ as before, and $\mathbf{r_j}^2 = \mathbf{q_i}^t \underline{\mathbf{G}} \mathbf{q_i}$, $\underline{\mathbf{G}} = \mathbf{h}^t\mathbf{h}$, where t represents the transpose. The resulting Hamiltonian is:

$$H = \sum_i \frac{\mathbf{p_i}^t \underline{\mathbf{G}} \mathbf{p_i}}{m_i} + U(\mathbf{q}) + \frac{1}{2}W\mathrm{Tr}(\dot{\mathbf{h}}^t\dot{\mathbf{h}}) + P_{ex}V, \tag{2.21}$$

where $\dot{\mathbf{h}} = \partial\mathbf{h}/\partial t$.

The most widely used technique for constant temperature is to scale the

velocities of the particles, either every step, or when the temperature has reached some specified level either above or below the desired temperature. However, scaling the particle velocities leads to discontinuous jumps in the energy of the system. The simulations in this thesis used a different method, devised by Nosé[33,34]. As with the constant pressure technique above, an extra degree of freedom is added to the system in the form of a scaling variable. In this case, the momenta are scaled as if the system were connected to an external bath: $\mathbf{p_i} = s\mathbf{p_i}'$, where the prime denotes a variable in real units. This is equivalent to scaling the time: $dt = dt'/s$. The resulting Hamiltonian for a system of isotropic particles is:

$$H = \sum_i \frac{\mathbf{p_i}^2}{2m_i s^2} + U(\mathbf{r}) + \frac{p_s^2}{2Q} + gkT_{ex} \ln s. \tag{2.22}$$

Here, p_s is the conjugate momentum of s, $p_s^2/2Q$ is the kinetic energy of time scaling and Q is the "mass" for the scaling. Also, g represents the number of degrees of freedom in the system, and T_{ex} the temperature of the external heat bath. The resulting equations of motion are:

$$\frac{d\mathbf{q_i}}{dt} = \mathbf{p_i}/m_i s^2 \tag{2.23}$$

$$\frac{d\mathbf{p_i}}{dt} = -\partial U/\partial \mathbf{r_i} \tag{2.24}$$

$$\frac{ds}{dt} = p_s/Q \tag{2.25}$$

$$\frac{dp_s}{dt} = \left(\frac{\sum_i \mathbf{p_i}^2}{m_i s^2} - gkT_{ex} \right) / s \tag{2.26}$$

It has been shown that this method rigourously reproduces the canonical ensemble when $g = 3N + 1$[33,34]. An alternate formulation of this method, using friction coefficients, and a discussion of the significance of time scaling on the dynamics of an MD simulation can be found in an excellent review by Hoover[35].

The constant temperature and constant pressure techniques can be combined, in order to simulate the isothermal-isobaric ensemble. The resulting Hamiltonian is:

$$H = \sum_i \frac{\mathbf{p}_i' \underline{G} \mathbf{p}_i}{m_i} + U(\mathbf{hq}) + \frac{p_s^2}{2Q} + gkT_{ex} \ln s + \frac{1}{2} W \mathrm{Tr}(\dot{\mathbf{h}}' \dot{\mathbf{h}}) + P_{ex} V. \qquad (2.27)$$

Where the variables in "real" units are: $\mathbf{r}_i = \mathbf{h}\mathbf{q}_i$, $\mathbf{p}_i' = \mathbf{h}\mathbf{p}_i/s$, and $dt' = dt/s$. The equations of motion for $\mathbf{q}_i$, $\mathbf{p}_i$, $\mathbf{h}$ and s can all be solved by use of the Gear predictor-corrector algorithm in a simulation. In most of the simulations presented in this thesis, the constant temperature technique was not used, since, in the systems studied, there was no problem with large temperature fluctuations.

The stability of an MD algorithm can be estimated by calculating the value of some constant of the motion of the particles during the course of a simulation run. In each ensemble, the Hamiltonian should be conserved, and this is the property which is normally calculated for this purpose. In simulations of the microcanonical ensemble (constant N,V,E), the total energy, $E = U + E_K$, will in fact fluctuate, due to the use of cut-offs in the potential, the use of a finite time step, and because of inaccuracies in the algorithm. In general, if the cut-off is too small or the time step too large, then E (and the temperature) will tend to drift. Ideally, the value of the cut-off is chosen as small as possible and the time step is chosen as large as possible (in order to speed up the computation) without causing a drift in E. For MD simulations, fluctuations in E of less than 1 part in 10^4 are normally considered acceptable.

2.2.3 Calculation of Thermodynamic Properties

The output of an MD simulation includes the positions and momenta of its molecules as a function of time. This data can be used to calculate both static and dynamical properties of the system. Static (thermodynamic) properties are calculated at each time step during the simulation, and then averaged over the total number of steps. The temperature of the system is calculated from the average translational and rotational velocities of the molecules:

$$T = \frac{m_i \langle v_i^2 \rangle}{3k} + \frac{\sum_\lambda \langle I_{i\lambda\lambda} \omega_{i\lambda}^2 \rangle}{3k}. \tag{2.28}$$

The pressure is calculated from the virial theorem[15]:

$$PV = NkT + \frac{1}{3} \left\langle \sum_{i=1}^{N} \mathbf{r}_i \cdot \mathbf{F}_i \right\rangle. \tag{2.29}$$

It is possible to calculate the heat capacity of a constant volume MD system from the temperature fluctuations[36]:

$$\frac{\langle T^2 \rangle - \langle T \rangle^2}{\langle T \rangle^2} = \frac{3}{2N} \left(1 - \frac{3Nk}{2C_v} \right). \tag{2.30}$$

Another property of interest is the site-site radial distribution function $g_{\alpha\beta}(r)$:

$$g_{\alpha\beta}(r) = \left\langle \frac{1}{\rho^2} \sum_{i \neq j} \delta(\mathbf{r}_{i\alpha}) \delta(\mathbf{r}_{j\beta} - \mathbf{r}) \right\rangle \tag{2.31}$$

where $\mathbf{r}_{i\alpha}$ and $\mathbf{r}_{j\beta}$ are respectively, the coordinates of site (atom) α on molecule i, and site (atom) β on molecule j ($j \neq i$). This function gives the average density of atom site β at a distance r away from atom site α, normalized to ρ, the density of molecules in the system. If the sites α and β are the centres of mass of their respective molecules, then $g_{\alpha\beta}(r)$ is the radial distribution of molecules in the system.

Dynamic (time dependent) properties are determined as follows. If $A(t)$ is a property which changes with time, then its time correlation function is defined as:

$$B(t) = \frac{\langle A(t) \cdot A(0) \rangle}{\langle A(0) \cdot A(0) \rangle}. \tag{2.32}$$

In MD calculations, $B(t)$ is averaged over all molecules and starting times. The velocity autocorrelation function is especially important, for it yields information on the translational motion of the molecules. It is defined as follows:

$$Z_\alpha(t) = \frac{\langle v_\alpha(t) \cdot v_\alpha(0) \rangle}{\langle v_\alpha(0) \cdot v_\alpha(0) \rangle} \tag{2.33}$$

where $\alpha = x, y, z$ denotes the components of the center of mass velocities of the molecules. The z-direction was chosen to lie perpendicular to the surface plane. This function gives the translational diffusion coefficient:

$$D_{tr} = \frac{1}{3} \int_0^\infty Z(t) dt, \tag{2.34}$$

where $Z(t) = \Big(Z_x(t) + Z_y(t) + Z_z(t)\Big)/3$. The translational diffusion coefficient can also be obtained from the Einstein equation:

$$D_{tr} = \lim_{\Delta t \to \infty} \frac{\left\langle [\Delta \mathbf{r}_i(t)]^2 \right\rangle}{2d\Delta t}, \tag{2.35}$$

where $\Delta \mathbf{r}_i(t)$ is the displacement of the center of mass of molecule i from its starting position, and d is the dimensionality of the system. In this way, one can calculate D_{tr} from the asymptotic region of a plot of $\langle (\Delta r)^2 \rangle$ *vs* time. This plot will be curved at small t, but at large t will tend to linearity. In practice, Eq.(2.35) gives higher values of D_{tr}, since the calculation of Eq.(2.34) is cut off at a finite time, and the contribution to D_{tr} from the long-time tail in $Z(t)$ is lost. Therefore, in this work, D_{tr}

was always calculated from Eq.(2.35). The Fourier transform of $Z_\alpha(t)$, namely the power spectrum, $Z_\alpha(\omega)$, is the density of states for molecular translational vibrations with polarization in the α direction.

The rotational motion can also be studied with the corresponding autocorrelation function for angular velocity:

$$C_\lambda(t) = \frac{\langle \omega_\lambda(0) \cdot \omega_\lambda(t) \rangle}{\langle \omega_\lambda(0) \cdot \omega_\lambda(0) \rangle}. \tag{2.36}$$

Here, λ denotes the three orthogonal axes of rotation of the molecules in the molecule-fixed frame. As for translational motion, $C_\lambda(t)$ gives the rotational diffusion coefficient for rotation about axis λ:

$$D_{rot\lambda} = \frac{kTN_0}{I_{\lambda\lambda}} \int_0^\infty C_\lambda(t) dt. \tag{2.37}$$

In a solid, the Fourier transform of $C_\lambda(t)$, namely $C_\lambda(\omega)$, is the phonon density of states for rotational motion (librations). Therefore, $Z_\alpha(\omega)$ and $C_\lambda(\omega)$ can be compared to lattice dynamics calculations of the phonon densities of states for translations and rotations. The phonon density of states can be experimentally determined by incoherent inelastic neutron scattering. However, these experiments are primarily sensitive to hydrogen atom motions, due to their high scattering cross-section. Therefore, in a simulation, an ACF must be calculated (in the space-fixed frame) for the velocities of the hydrogen atoms:

$$Z_{H\alpha}(t) = \frac{\langle v_{H\alpha}(t) \cdot v_{H\alpha}(0) \rangle}{\langle v_{H\alpha}(0) \cdot v_{H\alpha}(0) \rangle} \tag{2.38}$$

in order to compare with the scattering response function, since $S(\vec{k},\omega) \sim Z_H(\omega)/\omega$, where $Z_H(\omega) = \left(Z_{Hx}(\omega) + Z_{Hy}(\omega) + Z_{Hz}(\omega)\right)/3$.

2.3 Potentials

2.3.1 Intermolecular Potential

The potential between two molecules was taken as the sum of individual atom-atom potentials between all pairs of atoms of two molecules. The molecules were assumed to be rigid, with no intramolecular degrees of freedom. Also, three-body forces were not taken into account. Instead, effective two-body potentials were used, in which the effects of three-body forces are included by fitting the potential parameters to the properties of the solid phase. Multipolar interactions were also implicitly included in the effective potentials, and also were not explicitly added to simulations of the non-polar molecules of this study. For the models of the polar molecules CH_3F and CH_3Cl, interactions between partial charges were used to mimic the multipole interactions. This is discussed in more detail in Sec. 6.2.

The exp-6 potential was used for the intermolecular interactions, and it was of the form:

$$u(r) = A\exp(-Br) - C/r^6 \qquad (2.39)$$

The interaction sites for the potential were located at the positions of the atomic nuclei in the molecules.

2.3.2 Molecule-Surface Potential

The potential between an adsorbed molecule and the surface was taken as the sum of individual atom-atom potentials between the atoms of the molecule and the carbon atoms of first layer of the graphite surface. Lower layers of graphite atoms were

approximated by an integral, and were assumed to not contribute to the corrugation. A Lennard-Jones potential was always used for the atom–surface atom interactions:

$$u(r) = 4\epsilon\left\{\left(\frac{\sigma}{r}\right)^{12} - \left(\frac{\sigma}{r}\right)^{6}\right\}. \tag{2.40}$$

When necessary, the parameters were converted to those of the exp-6 potential by requiring the potential minimum to occur at the same location and the well depths to be the same for both potentials. The minimum of the LJ potential occurs at $r_m = \sigma\sqrt[6]{2}$, and putting this into Eq.(2.39), one gets:

$$\sigma = \frac{7\ln\sigma - \ln(6C/2^{\frac{1}{6}}AB)}{B\sqrt[6]{2}}. \tag{2.41}$$

The second condition yields the result for the well depth:

$$\epsilon = -A\exp(-B\sigma\sqrt[6]{2}) + \frac{C}{2\sigma^6}. \tag{2.42}$$

The atom-surface potential was summed over all atoms in the first layer of the graphite, approximated by taking the first two terms of its Fourier expansion, from the method of Steele[37]:

$$u_s^*(\mathbf{r_i}) = V_0(z_i^*) + W(\vec{\tau}_i)V_1(z_i^*). \tag{2.43}$$

Here $\mathbf{r_i} = \vec{\tau}_i + z_i$, where z_i^* is the height of atom i above the surface in reduced units $z_i^* = z_i/a_1$, a_1 is the length of the unit cell vector for the graphite hexagons (2.46Å), $\vec{\tau}_i$ is position of atom i in the (x,y) plane relative to some reference point on the surface, and $u_s^*(\mathbf{r_i})$, V_0, W, and V_1 are defined as follows:

$$u_s^*(\mathbf{r_i}) = u_s(\mathbf{r_i})/\epsilon_i \tag{2.44}$$

$$V_0(z_i^*) = \frac{4\pi A_i^6}{a_s^*}\left(\frac{2A_i^6}{5z_i^{*10}} - \frac{1}{z_i^{*4}} - \frac{1}{d(z_i^* + 0.61d)^4}\right) \tag{2.45}$$

$$W = -2\left[\cos\frac{2\pi}{a_1}\left(x_i - \frac{y_i}{\sqrt{3}}\right) + \cos\frac{4\pi y_i}{a_1\sqrt{3}} + \cos\frac{2\pi}{a_1}\left(x_i + \frac{y_i}{\sqrt{3}}\right)\right] \tag{2.46}$$

$$V_1(z_i^*) = \frac{16\pi^3 A_i^6}{3a_s^*}\left[\frac{4\pi^3 A_i^6}{90\sqrt{3}z_i^{*5}}K_5\left(\frac{4\pi}{\sqrt{3}}z_i^*\right) - \frac{8\pi^2}{3z_i^{*2}}K_2\left(\frac{4\pi}{\sqrt{3}}z_i^*\right)\right] \tag{2.47}$$

where

$$a_s^* = a_s/a_1^2 \tag{2.48}$$

$$A_i = \sigma_i/a_1 \tag{2.49}$$

Here, a_s is the area of the unit cell for the graphite hexagons, and d is the spacing between the graphite layers (3.35Å). Figure 2.1 illustrates the graphite basal plane, and shows the definitions of the axes used here. The x-axis is defined as lying along one of the rows of graphite hexagons, and the y-axis as perpendicular to the rows. The origin of the coordinate system for positioning the atoms of the adsorbed molecules in Eq.(2.46) was taken as the center of a graphite hexagon, as illustrated in Figure 2.1.

The modified Bessel functions of the second kind $K_2(c)$ and $K_5(c)$, were evaluated by a series approximation[38] valid for large c:

$$K_\nu(c) = \sqrt{\frac{\pi}{2c}}e^{-c}\left\{1 + \frac{\mu-1}{8c} + \frac{(\mu-1)(\mu-9)}{2!(8c)^2} + \ldots\right\},\ \mu = 4\nu^2. \tag{2.50}$$

In the simulations, $6 \le c \le 60$, corresponding to 2.0Å $\le z \le$ 20Å, and the series converges after 11 terms, giving six figure accuracy at $c = 6$ ($z = 2.0$Å), eight figures at $c = 10$ ($z = 3.4$Å), and ten figures at $c = 12$ ($z = 4.1$Å). This was considered

acceptable, since V_1 is much smaller than V_0, and no atom ever approached to within 2.0Å of the surface in any of the simulations.

Effectively, the potential is split into two parts: $V_0(z_i^*)$, corresponding to the flat surface approximation, and $W(\vec{r}_i)V_1(z_i^*)$, a correction term which takes into account the corrugation of the graphite surface. Typically, the magnitude of the corrugation term is about 2% of the magnitude of V_0 for this potential. The corresponding Fourier expansion for the exp-6 potential form has recently been formulated by Belak *et al* [39], but was not used in this study.

Inclusion of the corrugation term V_1 imposes an important constraint on the system to be studied when the simulation box has periodic boundaries parallel to (x,y). To ensure that the potential is continuous at these boundaries in simulations on the corrugated surface, the boundaries of the MD cell were kept fixed, with an integral number of graphite hexagons inside the MD box.

2.3.3 Anisotropic Potential

The above method of approximating the potential does not take into account the fact that the carbon atoms of the graphite basal plane are more polarizable in the plane of the surface than normal to it. It has been estimated[40] that the actual size of the corrugation is almost double the amount given by the Steele method outlined above. Vidali and Cole[40] have derived a more realistic form for the corrugated surface potential:

$$u(\mathbf{r}) = 4\epsilon\left\{\frac{\sigma^{12}}{|\mathbf{r}|^{12}}\left[1+\gamma_R\left(1-\frac{6}{5}\cos^2\theta\right)\right]-\frac{\sigma^6}{|\mathbf{r}|^6}\left[1+\gamma_A\left(1-\frac{3}{2}\cos^2\theta\right)\right]\right\}. \qquad (2.51)$$

Here, **r** is the vector between an atom of a molecule and an atom of the surface, and θ is the angle between **r** and the surface normal.

This potential has two parameters: γ_A and γ_R. The case $\gamma_A = \gamma_R = 0$ corresponds to the isotropic potential of Eq.(2.40). The correction to the attractive part of the potential, γ_A, was derived from the polarizability of the graphite atoms[40]:

$$\gamma_A = -2(1-b)/3(1+b) \tag{2.52}$$

$$b = P_{c\perp}(1 + E_g/E_{c\|})/[P_{c\|}(1 + E_g/E_{c\perp})] \tag{2.53}$$

where E_g is the excitation energy of an atom in the molecule, $E_{c\|}$ and $E_{c\perp}$ are the excitation energies of a carbon atom in the graphite, parallel and perpendicular to the surface normal, and $P_{c\|}$ and $P_{c\perp}$ the corresponding polarizabilities. However, $E_{c\|} \simeq E_{c\perp}$, so $b \simeq P_{c\perp}/P_{c\|}$ and $\gamma_A \simeq +0.4$ is independent of the type of adsorbate. Less is known about the form of the repulsive term, so γ_R is treated as an adjustable parameter. In this study, the simulations on the corrugated surface used the value $\gamma_R = -1.05$ which was adjusted to give the correct melting temperature for N_2 on graphite[41].

The Fourier series expression for $V_1(z^*)$ has been derived from Eq.(2.51) by Joshi and Tildesley[41], and is as follows:

$$V_1(z_i^*) = \frac{16\pi^3 A_i^6}{3a_s^*}\left\{\frac{4\pi^3 A_i^6}{90\sqrt{3}z_i^{*5}}\left[K_5 + \gamma_R\left(K_5 - \frac{2\pi z_i^*}{5\sqrt{3}}K_6\right)\right] - \frac{8\pi^2}{3z_i^{*2}}\left[K_2 + \gamma_A\left(K_2 - \frac{\pi z_i^*}{\sqrt{3}}K_3\right)\right]\right\} \tag{2.54}$$

where $K_\nu = K_\nu\left(\frac{4\pi}{\sqrt{3}}z_i^*\right)$.

2.3.4 McLachlan Interaction

The parameters used in the intermolecular potentials for the molecules of this study were mainly taken from potentials fitted to their properties in the bulk. So, by directly transferring these potential parameters to the molecules of an adsorbed layer, it is tacitly assumed that the presence of the surface does not alter the intermolecular potential.

However, it is known that this is not the case for adsorbed rare gases. A rare gas atom, adsorbed on a surface, though having an average dipole moment of zero, will in general have a non-zero instantaneous dipole moment. This dipole will induce an image in the substrate (with opposite direction), and with a strength which depends on the dielectric constant of the substrate. The atom will also induce a dipole in its nearest neighbor in the adsorbed layer, also oriented in the opposite direction. These two induced dipoles, in the substrate and in the neighboring molecule, will have a net repulsive interaction. This effective 3-body force, known as the McLachlan, or substrate mediated interaction[42,43,44], weakens the adatom-adatom interactions in a monolayer by about 15%. Although theory has not yet been extended to treat molecular physisorbed systems in general, it has recently been derived for two orientations of axially symmetric molecules above the graphite basal plane[45]. Therefore, this interaction was not included in the potentials used in this work.

Figure 2.1:

Diagram of the graphite basal plane, as seen from above, with the coordinate axes used in the text. The unit cell is also indicated, by its vectors $\vec{a}_1$ and $\vec{a}_2$. The circles mark the locations of adsorption sites in the $\sqrt{3} \times \sqrt{3}$ R30° commensurate structure.

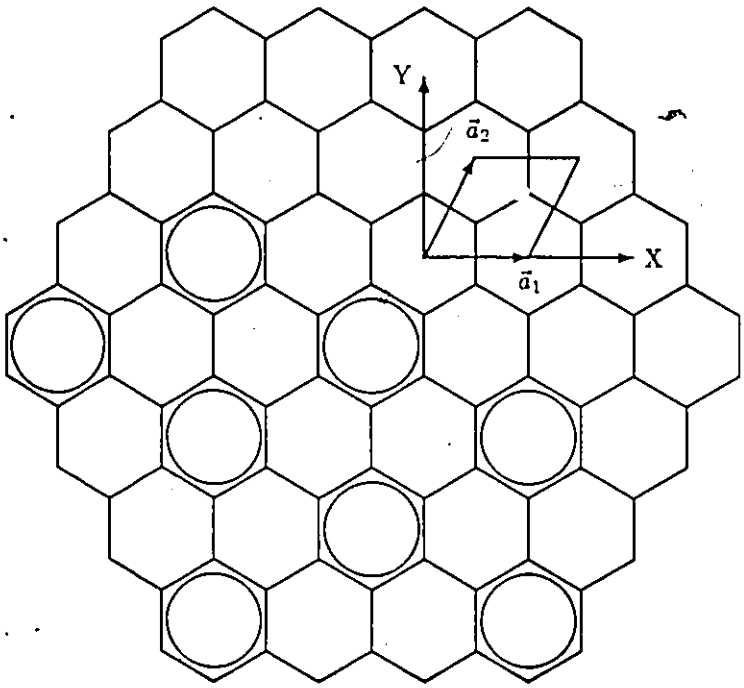

Chapter 3

Methane on Graphite

3.1 Introduction

Over the last decade, experimental and theoretical work on physisorbed overlayers has concentrated on small molecules, for example, CH_4, which is the simplest pseudo-spherical molecule. Methane has a hard-sphere diameter (4.2Å) which is intermediate between Kr (4.07Å) and Xe (4.4Å), and shows much the same behavior in an adsorbed film, but with a more complicated phase diagram in the solid form, due to the orientational degrees of freedom. Both Kr, which is smaller than the graphite crystal spacing, and Xe, which is larger, have incommensurate-commensurate (IC) phase transitions. The size of CH_4 is much closer to that of the graphite, but it too has the IC transition, which can be compared to those of the rare gases.

The phase diagram of CH_4 physisorbed on graphite has been worked out in detail by neutron[46,47,48,49] and electron diffraction[50], and is presented in

Figure 3.1. Below 50K, CH_4 forms a commensurate $\sqrt{3} \times \sqrt{3}$ R30° monolayer, called S_I. In this structure, the adsorbed molecules cover each third graphite hexagon, as illustrated in Figure 2.1, and it is used to define a coverage of 1.0 for all of the molecules of this study. In this phase, the CH_4 molecules are all resting on a tripod of hydrogen atoms, but are rotationally disordered about an axis normal to the surface. If the temperature is reduced, there is a transition at about 20K to an orientationally ordered layer[51,52]. Above 50K, the layer expands to form the so-called S_{II} phase. This phase is an incommensurate, triangular solid, whose nearest neighbor spacing varies from 4.26Å to 4.31Å depending on the temperature. The S_{II} phase melts at 57K, into a liquid phase, which transforms into a hypercritical fluid at 69K. Above a coverage of 1.0, CH_4 forms the so-called S_{III} phase, which is a triangular, compressed solid.

Some of the more recent investigations have concentrated on multilayer adsorption. Experiments have included calorimetry[53,54,55,56], neutron scattering[57], heat capacity measurements[58], and positron annihilation spectroscopy[59]. A theoretical static model calculation of the multilayers has also been reported[60].

The monolayer solid phases of CH_4 on graphite have been extensively studied by several theoretical methods, including lattice dynamics[61], MC[51], MD[62], static model calculations[63,64,65,66], and mean field theory[67].

3.2 Potentials

The potential for methane molecules adsorbed on graphite has been examined in some detail by Severin and Tildesley (ST)[62]. The parameters of this Lennard-Jones potential (see Table 3.1) were fitted to the rotational barrier heights (tunneling spectrum), the surface virial coefficient (Henry's law constant), and the isosteric enthalpy at zero coverage. As a result, interactions of the atoms of the methane molecules with the carbon atoms in the graphite (labelled C(Gr) in Table 3.1) have different potential parameters than for interaction with the carbon atoms of other methane molecules. The main feature of the ST potential is that the hydrogen atom size has been reduced, in order to approximate the increased rotation of the methane molecules due to rotational tunneling.

In this study, the CH_4 molecules were simulated in the relatively high temperature fluid phase, where the molecules act as free rotors[68], so that quantum tunneling of the rotations is not as important as in the solid. For this reason, the parameters for the intermolecular potential used here were taken from Williams[69]. The parameters for this potential (see Table 3.2) were fitted to the bulk crystal structures and lattice energies of simple hydrocarbons. These same parameters were also used for the molecule-surface potential *E(m-s)*, after conversion to the LJ form (see Table 3.3).

The methane molecules were assumed to be rigid, with a fixed C—H distance of 1.094Å. Also, the hydrogen atoms were replaced by deuterium, in order to increase the moment of inertia of the molecules to $6.428 g/mol(10^{-8}cm)^2$. In this way, the timestep could be increased to 2fs without loss of energy conservation, reducing the

Atoms	ϵ(kJ/mol)	σ(Å)
C—C	0.42568	3.35
C—H	0.19787	2.99
H—H	0.04049	2.61
C—C(Gr)	0.39643	3.30
H—C(Gr)	0.14134	2.98

Table 3.1: L-J Parameters for the Severin-Tildesley (ST) Potential

Atoms	A(kJ/mol)	B($Å^{-1}$)	C(kJ$Å^6$/mol)
C—C	311500	3.6000	2238
C—H	39380	3.6700	582
H—H	16736	3.7400	151

Table 3.2: Exp-6 Parameters for the Williams Potential

Atoms	ϵ(kJ/mol)	σ(Å)
C—C	0.38928	3.43
H—C	0.23436	2.92

Table 3.3: L-J Parameters for the Williams Potential

computer time needed for the calculations. The potential parameters for the D atoms were taken as the same as for H atoms of the Williams potential.

The simulations were performed with the corrugated surface model formulated by Steele[37], and the anisotropic potential form of Joshi and Tildesley[41]. The MD cell was fixed in size at 59.64Å×61.49Å, and there were 168 molecules, so the coverage was constant at 0.72 for all of the simulations. The system was run at five different temperatures: 50K, 55K, 60K, 65K, and 70K, in order to calculate the temperature dependence of the diffusion coefficients for both translation and rotation.

The results of the simulations are summarized in Tables 3.4 and 3.5. Typical errors in the data are: ±0.05 kJ/mol for *E(m-m)* and *E(m-s)*, ±0.03Å for $\overline{Z}_{CM}$, and ±25% for the diffusion coefficients, discussed in detail in the following section (Sec. 3.3).

The isosteric heat of adsorption at zero coverage, $q_{st}(0)$, has recently been measured by Inaba *et al.*[55] as −13.4 kJ/mol at 80K, compared to a calculated value of *E(m-s)* = −11.3 kJ/mol for a summation over only the top layer of graphite. This means that the Williams potential has underestimated the molecule-surface potential energy for methane on graphite, unlike the case for ethylene (see Ref.[10] and Sec. 4.3.3), which gave excellent agreement with $q_{st}(0)$ when only the first layer of graphite was included. From the integral approximation for the contribution of the lower layers in Eq.(2.45), and the average distance of the molecules above the surface (Table 3.4), the additional contribution was estimated to be −1.4 kJ/mol, bringing the total energy to −12.7 kJ/mol: about 5% too high. The heat of condensation of the S_I phase has been estimated from LEED isotherms[50] as Q = −16.7 kJ/mol.

T (K)	E(m-m) (kJ/mol)	E(m-s) (kJ/mol)	$\overline{Z}_{CM}$ (Å)
51.8	-3.9	-11.4	3.35
54.4	-3.9	-11.3	3.38
60.2	-3.6	-11.3	3.38
65.3	-3.5	-11.2	3.40
69.7	-3.4	-11.2	3.38

Table 3.4: Molecular Dynamics Results for Methane on Graphite

T (K)	D_{tr} (10^{-5}cm^2/s)	D_{rot} (meV)	D_{rotx} (10^{11}s^{-1})	D_{roty} (10^{11}s^{-1})	D_{rotz} (10^{11}s^{-1})
51.8	2.0	0.22	3.4	3.0	3.7
54.4	2.6	0.27	3.8	4.0	4.3
60.2	4.0	0.32	4.2	4.0	6.2
65.3	5.4	0.40	5.6	5.8	6.9
69.7	5.8	0.49	6.9	8.8	6.6

Table 3.5: MD Results for Diffusion of Methane on Graphite

Since

$$Q = H_g - E(m\text{-}m) - E(m\text{-}s) - E_K, \tag{3.1}$$

where H_g is the enthalpy of the 3-D gas, and E_K is the kinetic energy of the molecules, and, since $H_g \simeq E_K$[70], then $Q \simeq -E(m\text{-}m) - E(m\text{-}s)$, and therefore $E(m\text{-}m) \simeq -3.3$ kJ/mol from this experiment. This value is about 10% higher than the value found in the simulations, but the simulations did not include the McLachlan interaction. A recent static lattice calculation with the ST potential and including the McLachlan interaction found a value of $E(m\text{-}m) \simeq -2.9$ kJ/mol[63].

3.3 Dynamics

3.3.1 Translational Diffusion

The calculated values of the translational diffusion coefficients D_{tr} are listed in Table 3.5, and plotted in Figure 3.2 (filled circles). The value of D_{tr} was calculated from the variation of the mean square displacements of the molecules as a function of time. Figure 3.2 also shows the values of D_{tr} found from a quasi-elastic neutron scattering (QENS) study[71] of CH_4 at a coverage of $n = 0.63$ (open circles). There is excellent agreement for temperatures above 55K. This temperature represents the onset of melting (57K) in the experiments, as evidenced by the sudden jump in D_{tr}. In the simulations, the layer is already liquid at 50K.

The corresponding values of D_{tr} for a liquid ethylene layer under the same conditions (see Sec. 4.5) are plotted for comparison in Figure 3.2. Here, the filled squares represent the simulation results, and the unfilled squares represent the QENS

data[71]. As with the experimental data, D_{tr} for methane has a much greater temperature dependence than for ethylene. This result may be partly due to the different shapes of the two molecules.

3.3.2 Rotational Diffusion

The calculated values of the rotational diffusion coefficients D_{rot} are shown in Table 3.5, and plotted in Figure 3.3 (filled circles). These values were calculated from the angular velocity ACF for rotation about an axis through a C—H bond (D_{rotZ}), an axis perpendicular to Z and in the same plane as another C—H bond (D_{rotX}), and an axis perpendicular to both of the above (D_{rotY}). In their starting positions on the surface, the molecules were aligned with their Z-axes normal to the surface plane. The values for these three components of D_{rot} are listed separately in Table 3.5. The values for the components are equal to within the stated error of $\pm 25\%$, and indicate that the CH_4 molecules are free rotors in the fluid phase, confirming the experimental result[68]. If the molecules were, for example, single-axis rotors about their C—H bonds normal to the surface, one might expect D_{rotZ} to be larger than the other two. As yet, the rotational diffusion of CH_4 has not been examined experimentally.

Figure 3.3 also shows the values of D_{rot} for ethylene under the same conditions, where the filled squares represent the simulation results of Sec. 4.5, and the unfilled squares represent the QENS data[72]. Again, there is a greater temperature dependence for the methane diffusion, which indicates that it is more freely rotating than ethylene.

Figure 3.1:

Phase diagram for methane physisorbed on graphite, taken from Reference[50]. The symbols represent: liquid (L), gas (G), and hypercritical fluid (F), as well as the three solid phases: commensurate $\sqrt{3} \times \sqrt{3}$ R30° (S_I), incommensurate expanded (S_{II}) and compressed (S_{III}).

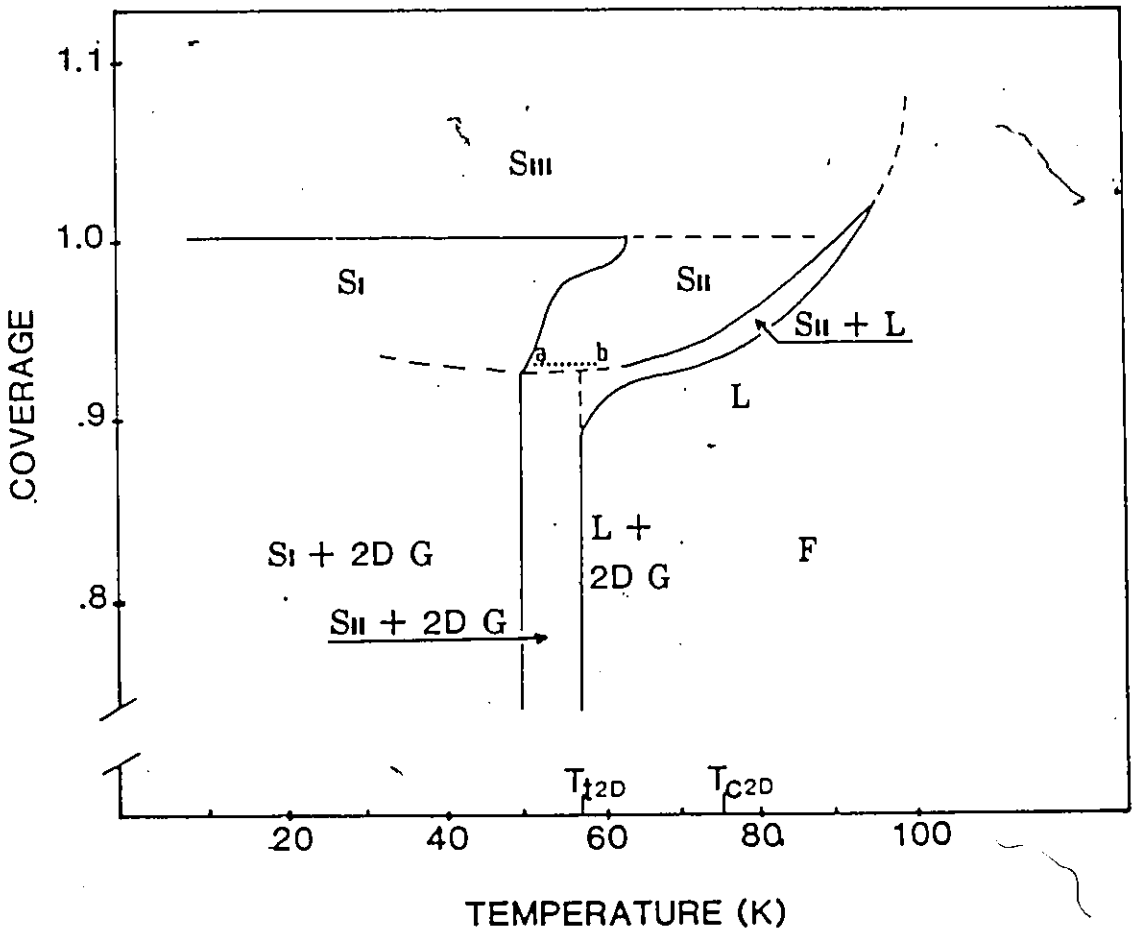

Figure 3.2:

Temperature variation of the translational diffusion coefficient for methane on graphite. Filled and unfilled circles represent the simulation and experimental data for methane, while the filled and unfilled squares represent the simulation and experimental data for ethylene.

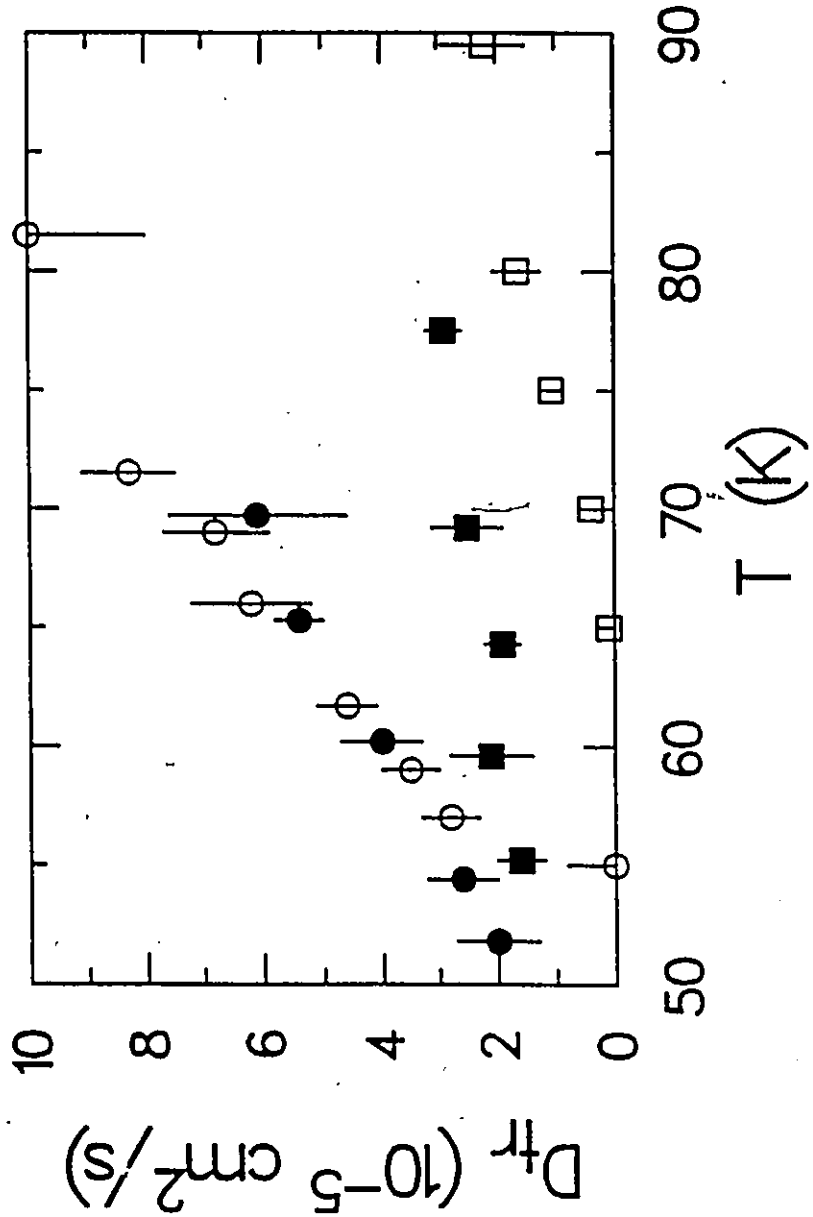

Figure 3.3:

Temperature variation of the rotational diffusion coefficient for methane on graphite. Filled circles represent the simulation data for methane, while the filled and unfilled squares represent the simulation and experimental data for ethylene.

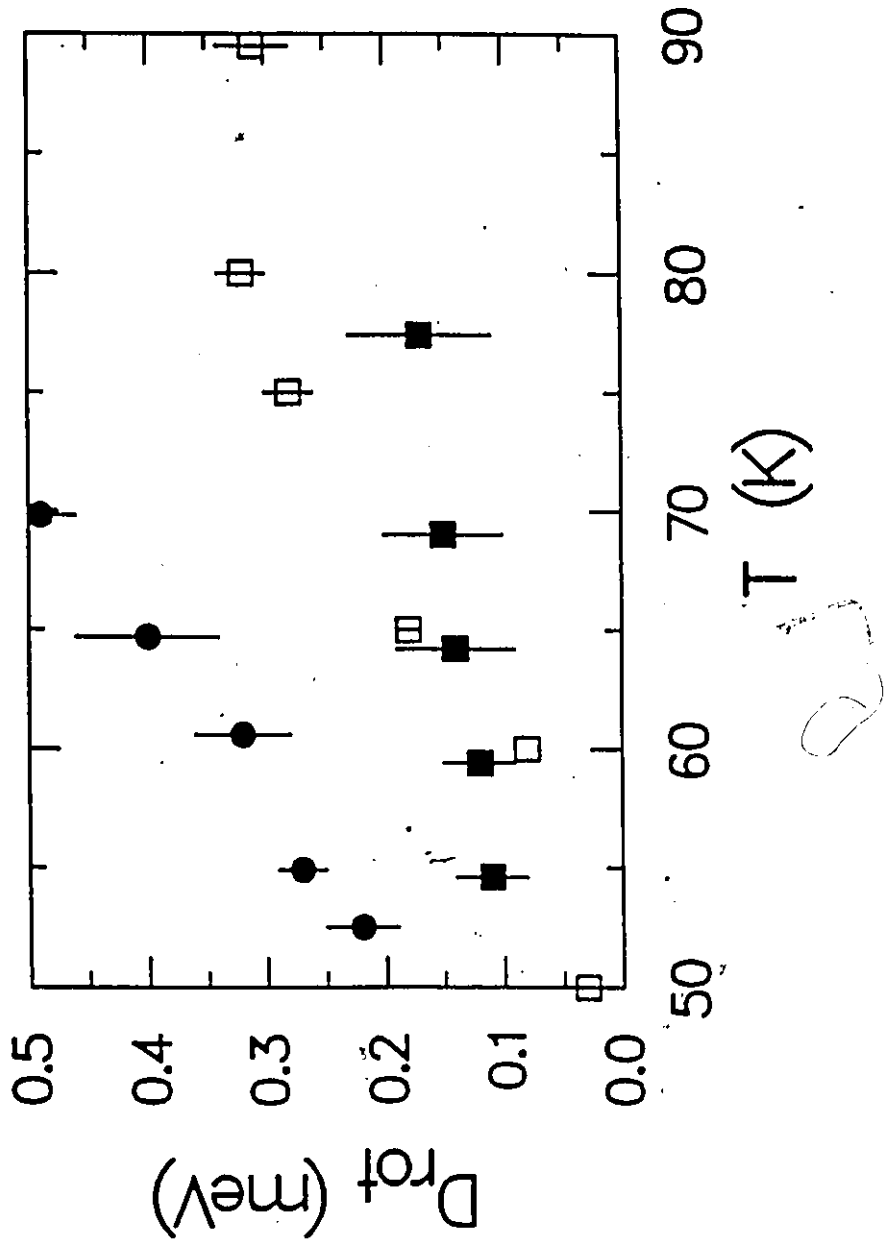

Chapter 4

Ethylene on Graphite

4.1 Introduction

Ethylene (C_2H_4), has been the object of considerable interest since the discovery of its incomplete wetting[73] and continuous melting[74] behavior on graphite. This chapter presents the results of two studies of the ethylene/graphite system. Section 4.3 reports on investigations into the low temperature structure, and Sec. 4.4 presents an attempt to model the melting transition and determine its mechanism.

4.2 Potentials

The exp-6 form (Eq. 2.39) was used to calculate the intermolecular potential *E(m-m)* for the ethylene molecules with parameters taken from Williams[69] (see Table 3.2). These parameters were also used to calculate *E(m-s)* (see Table 3.3). The variation of *E(m-s)*, as an ethylene molecule moves across the corrugated graphite surface is

about 50K for this potential. This value increases to about 95K for the anisotropic potential. The optimal configurational energy for a single molecule interacting with the graphite basal plane agrees to within a few percent of the value derived from the measured isosteric heat of adsorption extrapolated to zero coverage, $q_{st}(0)$ (see Table 4.2).

One simulation was performed using the methane potential of Severin and Tildesley (ST)[62] (see Table 3.1). The LJ parameters of this potential were converted to their equivalents in the exp-6 form (see Table 4.1) for use in the intermolecular potential.

4.3 Low Temperature Structure

4.3.1 Introduction

The various monolayer phases of ethylene adsorbed on graphite have been examined by such experimental methods as elastic and inelastic neutron scattering[75,76], synchrotron X-ray diffraction[77,78], calorimetry[74,79,80], and nuclear magnetic resonance[81,82]. The resulting phase diagram is shown in Figure 4.1.

These experiments have shown that overlayers of ethylene form three structural phases at low temperature. At coverages below $n = 0.8$ ethylene forms the so-called low density (LD) phase. Diffraction data available at the time of this study suggested a triangular lattice for this phase, with a nearest neighbor (n-n) distance of 4.65Å[75]. Subsequent to the MD simulations, new data has become available.[83] This is discussed further in Sec. 4.3.4. For $n > 1.0$, and $T < 70$K, ethylene forms

the high-density (HD) phase, which is a triangular lattice with n-n distance of 4.22Å. Calculations suggest that, in the HD phase, the C=C bonds are aligned perpendicular to the plane of the surface, while in the LD phase, the C=C bonds are aligned parallel to the plane of the surface[10]. Between $n = 0.8$ and $n = 1.0$ a two-phase (HD+LD) region exists[75,79,80]. There is also an intermediate density (ID) phase, which has a n-n distance of 4.42Å. This phase exists at high density ($n > 1.0$) for $T = 80$–85K. The arrangement of the molecules in the ID phase is not known. A variety of experiments indicate that both the LD and HD phases have a transition at about 35K from an ordered herringbone to a phase in which the molecules are rotationally disordered in the plane of the surface[81,82,79,80].

A number of MD simulations of ethylene on graphite have already been carried out with the Williams potential[10,84]. The low temperature structure and the rotator phase have been studied[10,84] with a flat surface model, which ignored the corrugation of the graphite basal plane. The calculated low temperature structure was not-in-agreement with the close-packed triangular lattice deduced from the original elastic neutron scattering measurements[75]. In particular, the structure was found to be based on a two molecule centered rectangular cell, approximately $1 \times \sqrt{2}$ rather than the $1 \times \sqrt{3}$ cell characteristic of a triangular lattice. Since these earlier calculations were performed on a flat surface model, the following MD simulations were conducted to determine if a triangular $1 \times \sqrt{3}$ structure for LD ethylene is induced by the surface corrugation of graphite.

4.3.2 MD Calculations

In order to examine the effect of the surface corrugation on the low temperature structure, MD simulations were performed on three different surface models: the flat surface, the corrugated surface, and the corrugated surface with the anisotropic potential (see Sec. 2.3.3). Simulations were also performed with two different sets of potential parameters. In most of the simulations, the Williams potential was used. One simulation was performed using the ST potential. All of the MD calculations were run at 20K for 20ps, after a short equilibration period of 5ps during which the velocities of the molecules were scaled to 20K. A timestep of 2.5fs was used, and gave excellent energy conservation. Typically, the fluctuation in the total energy was of the order of 3 parts in 10^5.

The simulations on the flat surface ($V_1 = 0$), used a system of 96 molecules which was started in a triangular lattice at a coverage of $n = 0.84$. The system was kept at constant spreading pressure by use of the 2-D analogue of the Parrinello-Rahman constant pressure technique (see Sec. 2.2.2), which meant that the sides of the box were allowed to fluctuate with time[85,86], and the system could relax to its equilibrium structure more efficiently.[10]

The simulations of the corrugated surface model ($V_1 \neq 0$) were run at constant area, because of the presence of the periodic boundary conditions (see Sec. 2.3.2). This was a serious limitation for a simulation which was supposed to allow the system to relax to its equilibrium configuration, including surface coverage. Also, if the simulation were run in a full simulation box at constant area, the resulting structure would be strongly dependent on the box shape. So, instead of using a full simulation

box, a patch of ethylene molecules was placed at the center of a box of fixed area approximately double the size of the patch. The patch contained 108 molecules in a box of dimensions $20 \times 12\sqrt{3}a$, where $a = 4.26$Å is the unit cell length for the $\sqrt{3} \times \sqrt{3}$ R30° triangular structure. The starting configuration for the molecules in this simulation was the equilibrated structure from the MD calculations on the flat surface. This was done to test the stability of the structure on the flat surface.

4.3.3 Results and Discussion

Flat Surface

The simulation on the flat surface was essentially a duplication of the previous work[10], but here the results are presented in more detail. In the present calculations, the system rapidly evolved from a triangular lattice to a lattice with a rectangular unit cell in a time of 4ps. Therefore, Table 4.2 lists averages over the last 5ps segment of the 10ps MD run. The calculated molecule-surface potential energy *E(m-s)* is very close to the experimental value of -20.3 kJ/mol[84], corrected to 20K (see Table 4.2). Figure 4.2 shows the radial distribution function G(R) for the centers of mass of the molecules. The inset shows G(Z), the distribution of the carbon atoms of the ethylene in the Z-direction, which is normal to the surface. The G(R) has its first three peaks at 4.30Å, 4.92Å and 7.05Å, which correspond to the three smallest intermolecular distances in the quasi two dimensional solid. In a triangular lattice, the first two peaks would be degenerate.

Figure 4.3(a) shows the instantaneous configuration (snapshot) of the system, seen from above, at the end of the simulation at 20K. The system forms a

Atoms	A(kJ/mol)	B($Å^{-1}$)	C(kJ$Å^6$/mol)
C—C	314635	3.6625	2132.3
C—H	146250	4.1035	501.06
H—H	29928	4.7009	45.36

Table 4.1: Exp-6 Parameters for the Severin-Tildesley (ST) Potential

Potl	Surface	T	E(m-m)	E(m-s)	Plane	a	b	n	Peak Pos
	Potl.	(K)	(kJ/mol)	(kJ/mol)	Tilt (°)	(Å)	(Å)		($Å^{-1}$)
W[a)]	Flat	21	-8.01	-20.1	62	4.92	7.05	.90	1.56, 2.55
W	Corrug	20	-7.72	-20.6	55	4.90	7.06	.91	1.56, 2.56
W	Anisotr	20	-7.69	-20.6	54	4.98	7.03	.90	1.55, 2.52
ST	Flat	21	-6.80	-20.8	13	5.35	7.35	.80	1.45, 2.35
Expt[b)]		10		-20.3[c)]	35	4.65	8.05	.84	1.57
Expt[d)]		20				5.03	7.05	.89	1.57, 2.49

a)Williams[69]

b)Data taken from Ref. [75]

c)Data taken from Ref. [84] and corrected to 20K

d)Data taken from Ref. [83]

Table 4.2: Molecular Dynamics Results for Ethylene on Graphite

stable herringbone, with individual molecules exhibiting only a small amount of rotational (librational) motion within the plane of the surface. The structure of the solid was deduced from this snapshot and from the G(R) peak positions. The ethylene molecules formed a herringbone structure, with a rectangular unit cell of dimensions 4.92Å×7.05Å, corresponding to a coverage of $n = 0.904$, or 0.0577Å^{-2}.

The C=C bonds of the molecules were aligned parallel to the surface plane, since G(Z) shows only a single peak. For the molecule at the corner of the unit cell, the molecular axis makes an angle of 30° with $\vec{a}$. The molecular axis of the molecule at the center of the cell makes an angle of -30° with $\vec{a}$, where $\vec{a}$ is the unit cell vector defined in Figure 4.4. The planes of the molecules do not lie flat (parallel to the surface), but are inclined an average of 62° from the plane of the surface. This compares to a tilt of 35°, found from static calculations[75] which had assumed a triangular lattice at a coverage of $n = 0.85$. The higher tilt is likely a consequence of the higher coverage in the simulated system. In the MD structure, the ethylene molecular axes make an angle of 60° with each other, as opposed to 90° expected for an ideal herringbone that arises from interacting point quadrupoles.

The above unit cell has a corresponding rectangular reciprocal lattice unit cell with cell lengths $|\vec{c}| = 2\pi/a = 1.28\text{Å}^{-1}$, $|\vec{d}| = 2\pi/b = 0.89\text{Å}^{-1}$. The expected neutron scattering peak positions will be combinations of $\vec{c}$ and $\vec{d}$: 1.56Å^{-1} (1,1), 1.78Å^{-1} (0,2), 2.19Å^{-1} (1,2), 2.55Å^{-1} (2,0), 2.67Å^{-1} (0,3) and 2.71Å^{-1} (2,1). The peak position of 1.56Å^{-1} agrees exactly with the experimental result[75]. However, the only other peak seen experimentally was at 2.70Å^{-1}, and these two peaks were used to index the triangular lattice at a coverage of 0.83.

In summary, these new calculations confirm that the calculated low temperature LD monolayer structure for ethylene on graphite is not triangular for this model.

Corrugated Surface

The MD simulation on the corrugated surface was run for 20ps. The motivation for this was to run long enough to allow for only local relaxation of molecular orientations and spacings. The determination of the true equilibrium structure of a patch at this temperature would likely require a prohibitively long computation.

The results of the simulation on the corrugated surface are presented in Table 4.2. Once again, *E(m-s)* is very close to the experimental value. In this case, by considering only those molecules in the center of the patch, the molecule-molecule potential energy *E(m-m)* has been adjusted to approximately eliminate the edge effects. Figure 4.2 shows the G(R) for the centers of mass, and G(Z) for the carbon atoms of the ethylene. Figure 4.3(b) is a snapshot of the system at the end of the simulation. The G(R) for the corrugated surface is virtually identical to the G(R) for the flat surface. The peaks are somewhat more spread out because of the movement of molecules at the edge of the patch. Unlike the flat surface model, G(Z) is asymmetric and displaced inward, because the ends of the ethylene molecules tend to settle into the centers of the graphite hexagons. Since the ethylene is incommensurate, the effect of the corrugation to some extent is averaged out.

The small shoulder in G(R) at about 3.85Å deserves mention. This shoulder is due to pairs of canted molecules with their molecular planes and C=C axes aligned

parallel to each other. In Figure 4.3(b), there are several pairs of molecules arranged in this way. This happens near the edge of the patch, where each molecule has an incomplete set of neighbors.

The G(R) peak positions are at 4.30Å, 4.90Å and 7.06Å. This corresponds to a centered rectangular unit cell of dimensions 4.90Å×7.06Å, which is a coverage of $n = 0.907$. It is otherwise identical to the unit cell of the flat surface simulations. From the snapshot of the system in Figure 4.3(b), it can be seen that the ethylene structure is rotated about 4° with respect to the graphite lattice. This particular structure would produce neutron scattering peaks at 1.56Å^{-1} (1,1), 1.78Å^{-1} (0,2), 2.19Å^{-1} (1,2), 2.56Å^{-1} (2,0), 2.67Å^{-1} (0,3), and 2.71Å^{-1} (2,1). Such a pattern would be indistinguishable from the pattern deduced from the flat surface simulations.

Because the structures for the flat and corrugated surfaces were so similar, it is possible that the latter calculation was not run for a sufficiently long time or that starting the corrugated surface calculations from the final flat surface structure had prejudiced the calculations. This would mean that the system had formed a metastable state, and not the ground state, as was desired. Accordingly, two new calculations were performed on the corrugated surface starting from structures which were expanded by 2% and 5% in both the X and Y directions. In both cases, the MD calculation yielded the same final structure as in Table 4.2.

Corrugated Surface (Anisotropic Potential)

The above results show that the surface corrugation had little influence on the low temperature structure of ethylene on graphite. However, recent work has demon-

strated the inadequacy of the isotropic form of the atom-surface potential, as it underestimates the size of the corrugation. Both N_2[41] and C_2H_4 (Sec. 4.4), when simulated with the isotropic atom-surface potential, have melting temperatures which are at least 9 degrees below the corresponding experimental values. Therefore, simulations were also performed with the corrugated surface and the anisotropic potential.

The results of the simulation with the anisotropic potential are shown in Table 4.2. Surprisingly, the enhanced corrugation of this potential seems to have no more effect on the ethylene structure than did the corrugation of the isotropic potential. The corrugation did not induce a triangular lattice. The G(R) and G(Z) for this system are shown in Figure 4.2. Figure 4.3(c) shows a snapshot of the system at the end of the simulation. The peak positions for G(R) are: 4.30Å, 4.98Å and 7.03Å. This corresponds to a centered rectangular unit cell of dimensions 4.98Å×7.03Å, and a coverage of $n = 0.898$. It is otherwise identical to the unit cell for the system on the corrugated surface.

This structure would produce neutron scattering peaks at $1.55Å^{-1}$ (1,1), $1.79Å^{-1}$ (0,2), $2.19Å^{-1}$ (1,2), $2.52Å^{-1}$ (2,0) and $2.68Å^{-1}$ (0,3)+(2,1). Again, this is indistinguishable from the results on the other two surfaces.

The Severin-Tildesley Potential

The agreement between the flat and corrugated surface models suggests that the monolayer structure of ethylene is really not triangular when the coverage is about 0.9. This is a higher surface density than was measured in the neutron measurements of Satija *et al.*[75]. The discrepancy between the calculated and measured density for

the LD phase may be due to to the fact that the Williams intermolecular potential is too attractive to use in an adsorbed system of ethylene. Therefore a new simulation was performed, with a much different potential[62], namely the ST potential (see Sec. 3.2). On a flat surface, the ST potential produced a herringbone with a unit cell of 5.35Å×7.35Å, which is less dense than both the experimental and earlier simulation results. Here, the molecules were all lying flat (molecular planes parallel to the surface). Therefore, the ST potential is not appropriate for ethylene adsorbed on graphite, and unfortunately does not resolve the discrepancy between the model and the original experiment.

4.3.4 Conclusion

Results of MD simulations of ethylene on graphite have been presented for both a flat surface and a corrugated surface. The corrugation appears to have little effect on the low temperature structure, even when the anisotropic surface potential was used. The calculations predicted that ethylene forms the low temperature structure shown in Figure 4.4, with a unit cell of 4.95Å×7.05Å, rotated by 4° with respect to the substrate. This would produce diffraction peaks at $1.55Å^{-1}$(1,1), $1.78Å^{-1}$(0,2), $2.19Å^{-1}$(1,2), $2.54Å^{-1}$(2,0), $2.67Å^{-1}$(0,3) and $2.69Å^{-1}$(2,1). Only peaks at $1.56Å^{-1}$and $2.70Å^{-1}$, which correspond to a triangular lattice, were seen in the original diffraction experiments at $n = 0.83$. However, in response to the above MD results, the diffraction experiments were repeated, and extended below $2.55Å^{-1}$, where new peaks were discovered at $1.76Å^{-1}$ and $2.49Å^{-1}$.[83] These peaks indicate that ethylene in fact has a rectangular unit cell, with parameters 5.03×7.05Å

(see Table 4.2), confirming the MD prediction.

The fact that the corrugation had such little effect on the structure was quite unexpected, given the large effect it had on the melting temperature (see the next section).

4.4 Melting of the Monolayer

4.4.1 Introduction

A current theory of melting in two dimensions, first proposed by Kosterlitz and Thouless[87], and further developed by Nelson and Halperin[88] and Young[89] (KTNHY), suggests that it should be continuous. This has resulted in a great deal of activity, both experimental and theoretical[90] on the subject of melting of physisorbed monolayers. In the KTNHY theory, melting is a two-stage process, the first being the unbinding of dislocations in the solid, leading to a loss of translational order, but retention of so-called bond orientational order. This kind of structure is called the hexatic phase. The second stage in the melting process is the loss of bond orientational order, marking the formation of the liquid phase.

The melting characteristics of several different physisorbed systems have been examined experimentally[91,74,92,93,94]. Thus far, there has been no clear evidence for KTNHY-type melting, and the hexatic phase has never been seen in an experiment on a physisorbed overlayer. In fact, the experiments have shown that monolayer melting is, in general, not continuous, but first-order. For example, submonolayer films of methane show a sharp first-order transition; the heat capacity peak associated

with melting is narrow and exceeds 100 k_B in height[91]. On the other hand, the behavior of the aspherical molecule ethylene (C_2H_4) is quite different. Here, melting extends over several degrees and the heat capacity peak, shown in Figure 4.5, has a maximum height of only about 2 k_B[74]. The latter observation has been interpreted as evidence for a continuous melting transition[74]. Until very recently, ethylene was the only system known to show continuous melting. In order to seek a possible microscopic explanation of this observation, a molecular dynamics (MD) study was undertaken to simulate the melting transition of ethylene on graphite.

4.4.2 Calculations

In these calculations, the same model was used for the ethylene molecules as was used in the previous section. The simulations were performed on the corrugated surface model, with the isotropic potential form ($\gamma_A = \gamma_R = 0$). Due to the constraint of the periodic boundary conditions, the simulations were performed at constant area and at two different coverages. One set of calculations employed a box with sides $13\sqrt{3}a \times 23a$, where a is the lattice constant for the graphite basal plane hexagons. There were 598 hexagons within this box. The system had $N = 168$ ethylene molecules, so the coverage was $n = 0.84$. This coverage corresponds to the experimentally determined coverage of a complete monolayer of the so-called low-density phase at temperatures just below melting. The remaining simulations were carried out with $N = 132$ molecules in a box with edges $11\sqrt{3}a \times 20a$. Since this box contained 440 hexagons, the coverage was $n = 0.90$. This was the low temperature equilibrium coverage for the Williams potential as determined in previous calculations[10] (see

also Sec. 4.3.3). Simulations were run at this coverage, when the results of the simulations at $n = 0.84$ showed a melting temperature much lower than experiment. This might have been due to the use of a coverage which was less than the equilibrium value for the model, resulting in enhanced motion of the molecules. By performing simulations at the higher coverage corresponding to the equilibrium coverage for the model, this problem could be avoided.

Experimentally, ethylene overlayers always melt from the rotationally disordered LD phase, where the C=C molecular axes are predominantly parallel to the graphite basal plane[10,75,74,76,82]. As a result, the MD calculations were initiated from ordered triangular herringbone structures with *all* C=C axes parallel to the graphite surface. In order to observe the melting, systems were prepared at temperatures ranging from 40K to 100K. In all cases, the ethylene molecules became orientationally disordered in the plane of the surface, as observed experimentally at these temperatures. A typical simulation of the $n = 0.84$ system, run for about 200ps using a time step of 2.5fs, took about 26 hours of CPU time on an IBM3090, and a similar simulation of the $n = 0.9$ system took about 22 hours of CPU time. Because of this, it was impractical to investigate a larger system size, even though finite size effects will be important for such a property as melting.

In order to locate the melting temperature, the structure amplitude

$$S(\mathbf{k}) = \left\langle \sum \cos(\mathbf{k} \cdot \mathbf{r}) \right\rangle \tag{4.1}$$

and hexagonal order parameter

$$g_6 = \left\langle \sum \cos 6\phi \right\rangle / 6 \tag{4.2}$$

were evaluated as running averages throughout each simulation. Here, **k** is one of the three smallest reciprocal lattice vectors of the triangular lattice appropriate to the surface coverage of interest, **r** is the distance between the centers of mass of two molecules and the summation is over all such pairs of molecules. Also, ϕ is the orientational angle of a nearest-neighbor bond with respect to $\vec{a}_1$ of the graphite lattice. These order parameters were calculated for each molecule in the system as the origin, and then averaged. The average was also taken over all pairs of molecules and timesteps. As defined, $S(\mathbf{k})= 1$ for a perfectly static triangular lattice and falls to near zero for a translationally disordered liquid. For perfect hexagonal orientational order, $g_6 = 1$, and also drops to near zero for random bond orientation. The value of g_6 could be used to look for the hexatic phase, since this phase would have a value of g_6 significantly larger than $S(\mathbf{k})$, which would be zero. In a solid at temperatures above zero, $S(\mathbf{k})$ and g_6 are reduced to a value less than unity by the Debye-Waller effect (thermal motions), and static disorder (dislocations). In the following discussion and figures, the structure amplitude is taken to be the average of all three $S(\mathbf{k})$ values where k= (1,0), (0,1) and (1,1).

The diffusional motions of the ethylene molecules on the surface were also studied. The translational diffusion coefficient, D_{tr} was obtained from the time dependence of the mean square displacements of the molecular centers of mass in the (x,y) plane. Rotational diffusion coefficients, D_{rot} were obtained from the appropriate angular velocity autocorrelation functions (see Sec. 2.2.3). The value of D_{rot} was calculated for rotation about axes in the molecular plane both parallel (R_X) and perpendicular (R_Y) to the C=C axis as well as rotation about an axis perpendicular

to the molecular plane (R_Z). These assignments are identical to those in the earlier simulation study on the flat surface[10]. Rotational motion about C=C (R_X) was found to be by far the most important. Other quantities monitored included the average tilt of the C=C axis away from the plane of the surface, and the configurational energies *E(m-m)* and *E(m-s)*.

4.4.3 Results

Figure 4.6 shows the time evolution of the order parameters $S(\mathbf{k})$ and g_6 at a temperature just below melting, and Figure 4.7 shows the same data at a temperature just above the melting transition, both in the system with $n = 0.90$. The slow decay of $S(\mathbf{k})$ for the simulation at $T = 63$K indicates that, close to the melting transition, long simulation trajectories (200ps) are required to establish equilibrium.

Figure 4.8 shows the temperature dependence of $S(\mathbf{k})$ and g_6 for both coverages. The values of $S(\mathbf{k})$ and g_6 were calculated every 25 steps, and were averaged over the length of the runs for times after the system had reached equilibrium, as shown by plots of $S(\mathbf{k})$ versus time. The error bars represent the standard deviations of these values. For the series with $n = 0.84$ (dots) there is a decrease in $S(\mathbf{k})$ in the region 52–60K whereas the drop occurs between 57K and 63K for the series with $n = 0.90$ (squares). This drop-off in $S(\mathbf{k})$ was used to identify the melting regions for this model at both coverages. The fluctuations increased considerably as the temperature approached the melting point. This corresponded to the formation and annealing of dislocations. The value of g_6 showed exactly the same behavior as a function of temperature as did $S(\mathbf{k})$. Unfortunately, the calculated melting regions

are somewhat lower than the experimental counterparts which are centered around 70K and 80K. This disagreement is probably due to inadequacies in the interaction potentials used in the model.

Figure 4.9 shows the temperature variation of the diffusion coefficients D_{tr} and D_{rot}. The error bars represent the standard deviation of sub-averages over 10ps segments of the total simulation time. The values of D_{tr} were taken from plots of $\langle[\Delta r]^2\rangle$ *vs* time, two examples of which are shown in Figure 4.10: one on either side of the melting temperature for the system at $n = 0.84$. The solid line represents the total mean square displacement of the molecular centres of mass, while the dashed line represents the value after subtraction of the average mean square displacement of the entire system. The figures show, that, in both cases, there is significant collective translational motion of the layer. This has also been seen in MD simulations of other systems[8], and probably represents a conversion of rotational kinetic energy to translational kinetic energy through rotation-translation coupling. In Figure 4.10 (a), near 70ps, the difference in the two curves is about 18Å^2, which corresponds exactly to a translation between two neighboring graphite hexagons. The figure may represent a very low frequency oscillation of the layer, with an amplitude of vibration of one graphite lattice spacing. It may also represent the onset of the floating transition, where the temperature is high enough that the corrugation no longer keeps the layer from moving in the plane of the surface. The figure also shows that, after subtraction of the center of mass motion, the mean square displacement did not vary with time, but reached a limiting value of about 3Å^2. This indicates that the system was a good solid at this temperature.

A line drawn through the values of D_{tr} extrapolates to zero at about 50K for $n = 0.84$ and at about 55K for $n = 0.90$. These values lie below the respective melting regions for this model and suggest that D_{tr} is continuous across the melting "transition". Recent quasi-elastic neutron scattering data are in agreement with this result but also suggest that the melting is associated with enhanced molecular rotation about R_Y and R_Z, the molecular axes perpendicular to C=C[72]. This latter observation seems to be at variance with the MD results (Figure 4.9(b)), which show little increase in D_{rotY} or D_{rotZ} through the melting transition. This discrepancy may be related to the fact that, in the experiment, the overlayer can expand on heating, whereas the calculations were carried out at fixed coverage, which would tend to restrict the motions of the molecules.

Figure 4.11 shows the temperature variation of the configurational energies *E(m-m)* and *E(m-s)*. These quantities exhibit only a small variation across the melting region. Indeed, crude estimates (by eye) of the derivatives of these curves with respect to temperature suggest a specific heat anomaly which is less than $3k_B$ in the relevant transition regions. This behavior is entirely consistent with the measured heat capacity result ($2k_B$)[74]. Calculations of C_v from Eq.(2.30) did not indicate an anomaly, due to the wide temperature spacing between the simulation points.

Even though the calculated melting temperature for this model is too low, it was apparently successful in modeling the small thermal anomaly at the melting transition[74]. Accordingly, the model was used to search for a possible microscopic explanation of this weak transition. Of all the quantities examined, only one showed any dramatic change at melting and that was the number of molecules standing up

in the $n = 0.84$ system. Figure 4.12 shows the orientational distribution function for the tilt of the C=C axis with respect to the surface plane for the simulations at $n = 0.9$ for four temperatures: 53K, 63K, 71K and 80K. This distribution was bimodal, with peaks at 0° and 80° and a well-defined minimum extending from about 15° to 65°. Based on this observation, a standing molecule was defined as one for which the C=C axis tilt exceeded 65° above the surface plane. Figure 4.13 shows a plot of the fraction of such molecules versus temperature. This quantity increased steadily in the liquid phase. In the solid phase prior to melting, random molecules were observed to stand erect and stay that way for times of order 10-20ps. This was particularly true for the $n = 0.9$ system.

The simulated systems always contained dislocations in the solid phase prior to melting. However, in view of the small size of the simulation systems employed, it was not possible to establish whether or not fluctuations involving the standing up of molecules were unequivocally correlated with the formation and motion of dislocations which, in turn, drive the melting, as in the KTNHY theory[87]. Nor can it be said that the hexatic phase was observed, since, in Figure 4.8, g_6 has the same temperature dependence as $S(\mathbf{k})$. From an inspection study of the phase space trajectories, it was evident that local density fluctuations involving standing molecules indicated the onset of melting in the system with $n = 0.84$ (see Figure 4.13). In the other system ($n = 0.90$), these fluctuations involving standing molecules persisted for longer times and on average, there were already a few molecules standing in the rotator phase solid. These can be attributed to the fact that the $n = 0.90$ system was in a compressed state, since at high temperature ($T > 40$K), this model

has an equilibrium density of 0.84[10]. In this case, the fluctuations served to relieve the stress, but the system remained solid. From this, it is concluded that the standing of molecules and the formation of associated dislocations is not alone sufficient to drive the melting. Other processes, such as movement of the molecules into interstitial sites, must be involved.

However, the melting process seems to be the same in the low density case, since the estimated heat capacity anomaly in Figure 4.11 is very close to the experimental value. Figure 4.7 shows the evolution of the structure factor as the $n = 0.90$ system goes through the melting transition. The number of standing molecules was monitored throughout this particular run. The fraction of erect molecules varied smoothly from 0.05 in the solid region ($t < 100$ps) to 0.10 in the liquid region ($t > 100$ps). The steady change in the number of erect molecules as the system proceeded through the melting transition likely means that the tilting did not drive the transition, but, since it was occurring concurrently with other mechanisms, acted to smear it. Therefore, the combination of different mechanisms make the melting appear to be continuous. In any case, the small change in *E(m-m)* at melting (Figure 4.11) confirms that the simulated transition definitely has a broad thermal anomaly at both coverages, in excellent agreement with experiment.

4.4.4 Discussion

An analysis of the MD calculations leads to the conclusion that the melting of ethylene films physisorbed on graphite is strongly influenced by molecular reorientation. The local density fluctuations which are required for melting are enhanced when

some of the molecules *stand up*, with their C=C axes perpendicular to the graphite basal plane. The previous MD study of C_2H_4/graphite on a flat surface identified translation-rotation coupling as playing an important role in the dynamics of ethylene overlayers[10]. However, the process in which molecules become erect does not appear to be related to such cooperative (collective) phenomena or a phase separation. The fluctuations seemed to occur randomly in the samples which were examined, and persisted for times of order 10-20ps. This suggests that the observed anomalous melting transition for ethylene on graphite is intimately associated with this novel process.

In conclusion, molecular dynamics has been successfully used to simulate the melting of ethylene on a corrugated graphite surface. The melting temperature of the computer model is lower than the experimental value. Two possible reasons for this come to mind. Firstly, the model has not taken into account the anisotropy of the molecule-surface potential, which, in the case of N_2 lead to an increase of 9 degrees in the melting temperature for a similar computer model[41]. Secondly, there are likely residual errors in the intermolecular potential itself. Neither of these points will likely have any bearing at all on the nature of the melting transition, which apparently is smeared out by the gradual standing up of the ethylene molecules. A similar phenomenon has been observed in MD calculations on the system O_2/graphite[8]. A recent ac calorimetry study of ethane monolayers on graphite has given evidence for a continuous melting transition for this system also[95]. Given the great similarity in size and shape between ethylene and ethane, it is possible that the same mechanism is at work in this system.

4.5 Dynamics of the Liquid Phase

4.5.1 Translational Diffusion

The dynamics of the liquid phase was examined by a number of simulations at a fixed coverage of 0.72. Five different temperatures were examined: 55K, 60K, 65K, 70K and 75K. Under these conditions, the values of D_{tr} can be directly compared to the CH_4 values of Sec. 3.3. As above, D_{tr} was calculated from the mean square displacements of the molecular centres of mass. The resulting values of D_{tr} are shown in Table 4.3, and plotted in Figure 4.14.

These values show that there is enhanced motion of the molecules, relative to the INS data[72] (unfilled squares) at low temperature. It was first speculated that this enhancement came from molecules in an adsorbed gas phase in the layer which move at high velocity between patches of liquid (or solid). These patches are present because the coverage (0.72) is less than a complete monolayer, so the system is in two-phase equilibrium (liquid + gas). Diffusion data from INS experiments do not include the contribution from this gas phase, partly because of its low density (and thus low scattering intensity), and partly because the effect is spread over a large spectral range[72]. However, when the effect of the gas phase molecules was removed from the calculation of D_{tr}, the values were only decreased by about 10%, and for the lowest temperature case, did not reduce it to solid-like values ($D_{tr} < 1.0\times10^{-5}\mathrm{cm}^2/\mathrm{s}$), or to the values from the full-layer simulation of the previous section. One possible explanation then, is that in the experiments, the patches are pinned to the substrate by inhomogeneities in the surface, an effect which was not taken into account in the

simulations.

A previous MD study of ethylene adsorbed on graphite, but on a flat surface model[10], found, in the liquid phase at $n = 0.75$ and $T = 75$K, a value of $D_{tr} = 2.8 \times 10^{-5}\text{cm}^2/\text{s}$. The corresponding value from this study on the corrugated surface is $2.5 \times 10^{-5}\text{cm}^2/\text{s}$, which is well within the stated error of $\pm 25\%$. Inclusion of the corrugation seems to have reduced the value of D_{tr} only very slightly, if at all.

4.5.2 Rotational Diffusion

The rotational diffusion coefficients D_{rot} were also calculated in the above simulations and their values are listed in Table 4.3, and plotted in Figure 4.15. The value of D_{rot} (in meV) was calculated using an average moment of inertia for ethylene of 13.623 g/mol Å^2, and the average velocity ACF of the ACFs for rotations about the principal axes. The results are very similar to the results from the simulations of the melting. There is significant rotational diffusion at low temperature, unlike the INS data (unfilled squares), which show little rotation in the solid and a sudden increase at melting. The values of the three components of D_{rot} indicate that, in the simulations, ethylene is not a free rotor, but rotates mainly about its C—C bond axis. The MD study of ethylene on a flat surface found values of: $D_{rotX} = 12.5$, $D_{rotY} = 2.0$ and $D_{rotZ} = 1.3 \times 10^{11} s^{-1}$. The corresponding values from this work on the corrugated surface (see Table 4.3) are slightly lower, but within the stated errors (25%). As was the case for D_{tr}, the corrugation had only a minimal effect on D_{rot}.

T	D_{tr}	D_{rot}	D_{rotx}	D_{roty}	D_{rotz}
(K)	(10^{-5}cm^2/s)	(meV)	(10^{11}s^{-1})	(10^{11}s^{-1})	(10^{11}s^{-1})
55.2	1.6	0.11	7.1	0.8	0.8
59.6	2.1	0.12	7.6	1.0	1.1
64.3	1.9	0.14	9.2	1.1	1.2
69.2	2.5	0.15	9.6	1.1	1.2
77.5	2.9	0.17	10.5	1.5	1.6

Table 4.3: MD Results for Diffusion of Ethylene on Graphite

Figure 4.1:

Phase diagram for ethylene physisorbed on graphite, taken from Reference [74]. The symbols locate the following phases: low-density herringbone, both ordered (OLD) and disordered (DLD) in the plane of the surface, intermediate density (ID), and high density (HD), along with liquid (L) and vapour (V) phases.

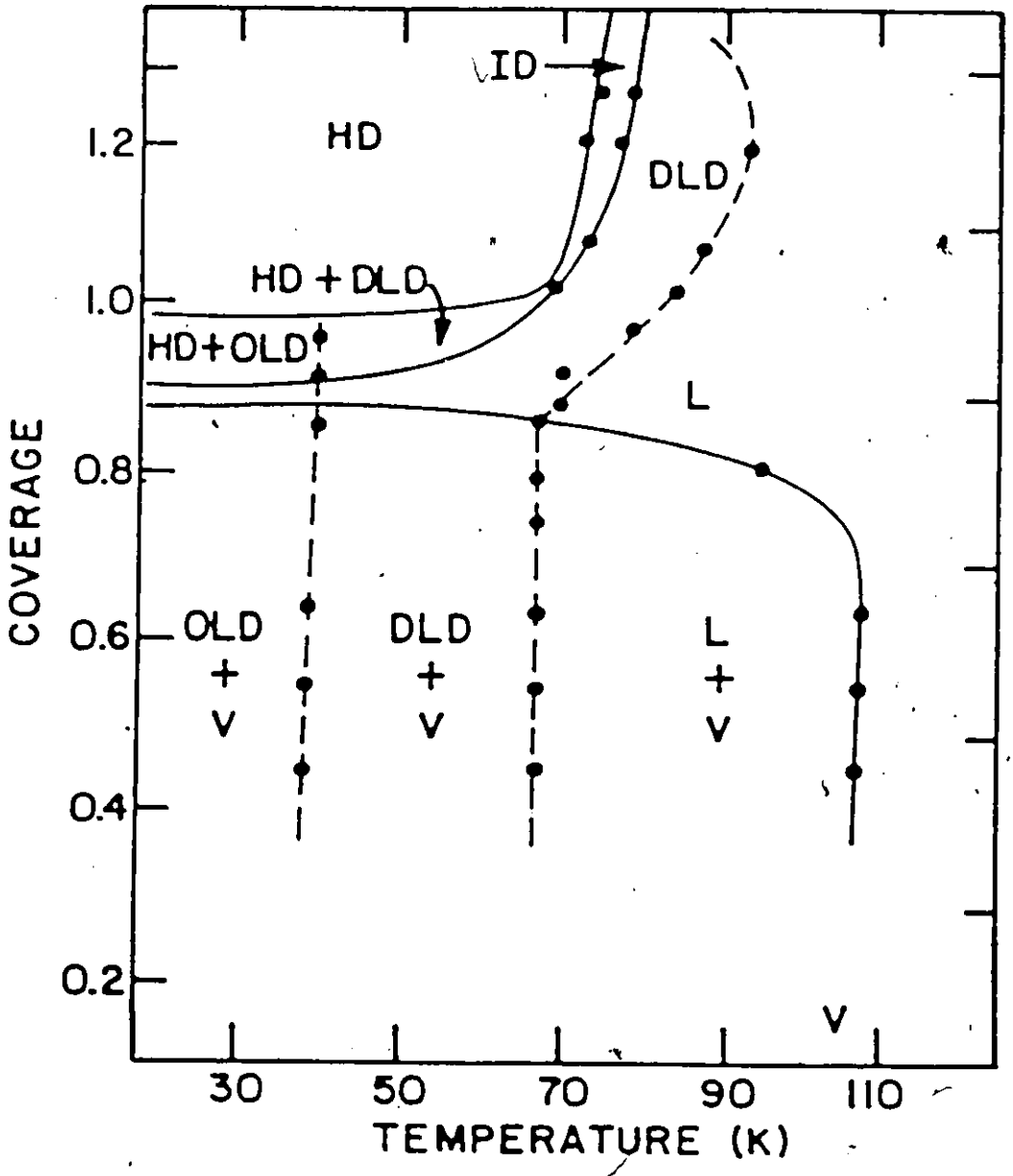

Figure 4.2:

Pair distribution function G(R) for ethylene on graphite. The inset shows the single particle distribution G(Z) for the carbon atoms of the ethylene molecules in the direction normal to the surface. The solid curve is the G(R) for the system on the flat surface, the dashed curve is for the patch on a corrugated surface, and the dotted curve is for the patch on the corrugated surface with the anisotropic potential form.

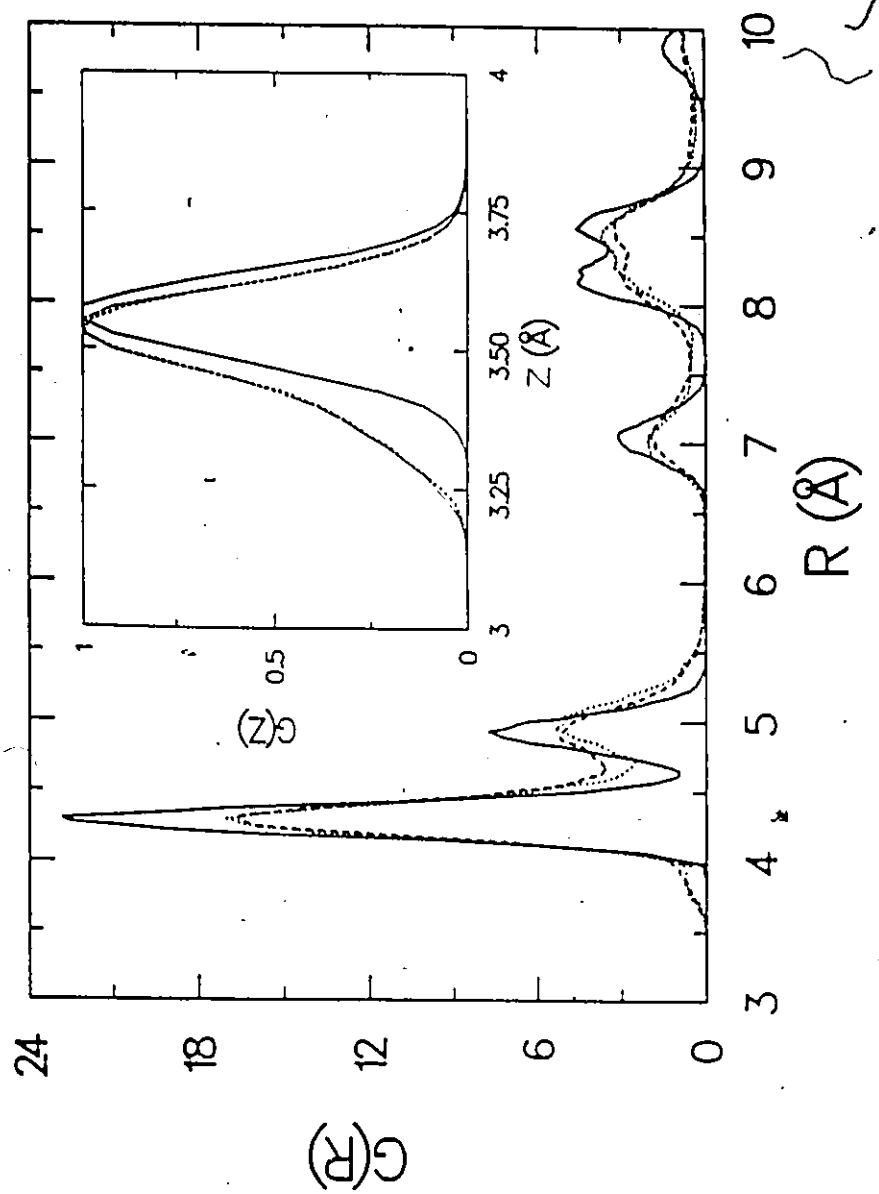

Figure 4.3:

Top views of the instantaneous configurations (snapshots) of the ethylene molecules on the three different surface models at the end of the simulation runs; (a) a section of the system on the flat surface, (b) the entire patch on the corrugated surface, and (c) the patch on the corrugated surface with the anisotropic potential model. The dots represent the positions of the carbon atoms in the first layer of the graphite.

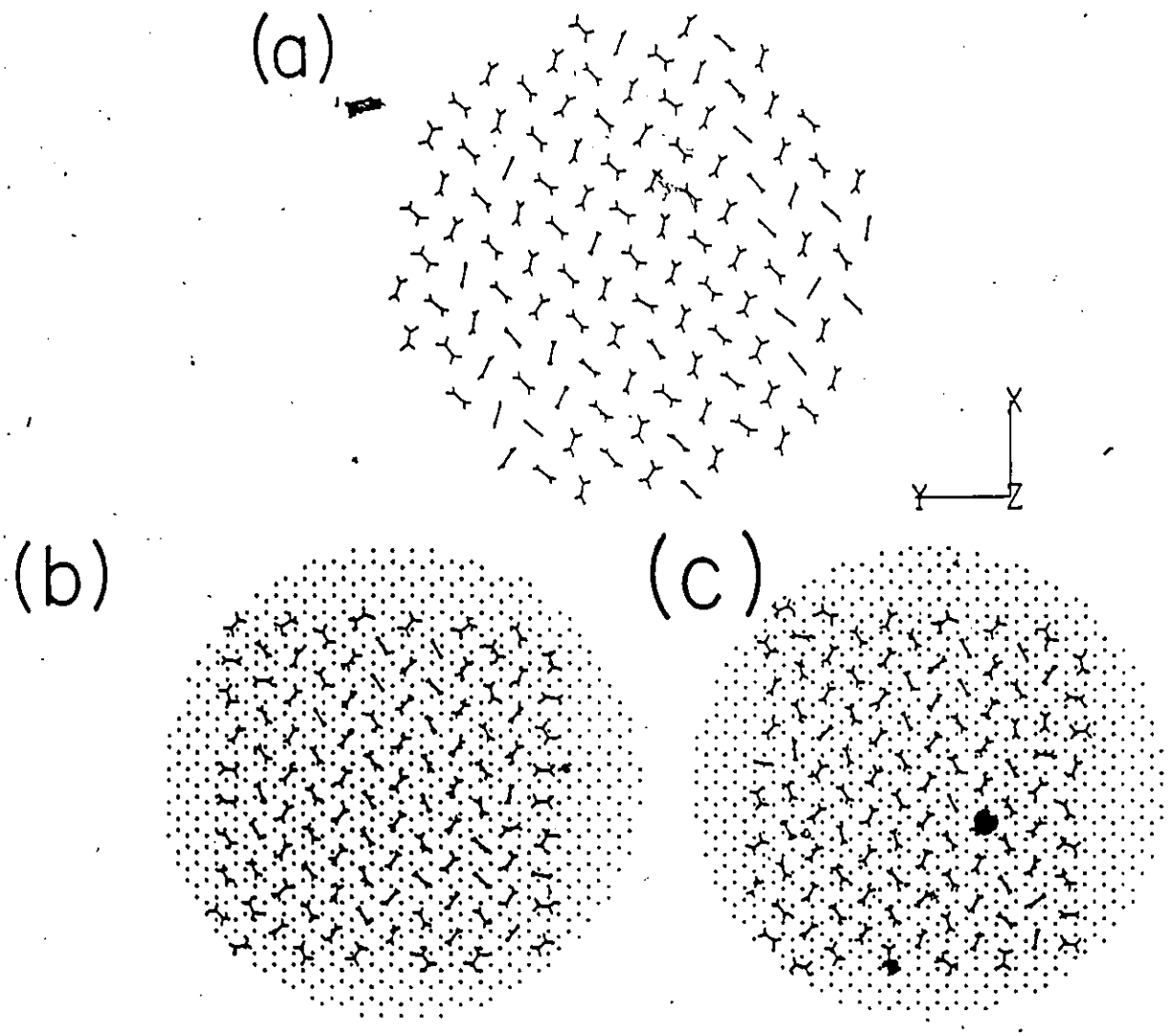

Figure 4.4:

Unit cell for low temperature ethylene on graphite as deduced from the simulations. The molecules are arranged with their C=C axes parallel to the plane of the surface, and rotated 30° with respect to $\vec{a}$. The molecular planes are canted 55° away from the plane of the surface.

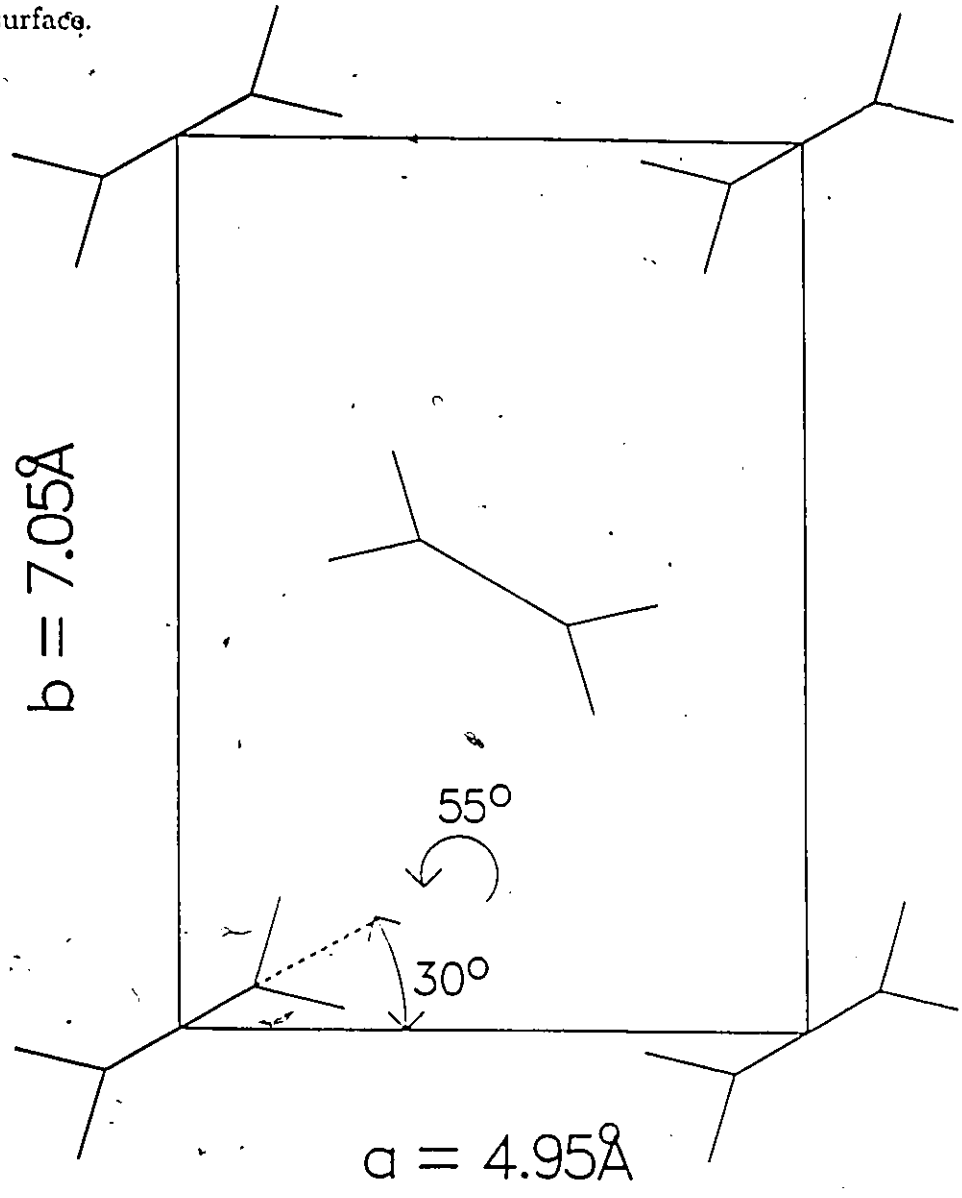

Figure 4.5:

Heat capacity scans across the melting transition for ethylene (C_2D_4) on graphite. The anomalies near 70K for $n = 0.92$ and $n = 0.98$ are due to structural transitions in the solid phase. Taken from Reference [74].

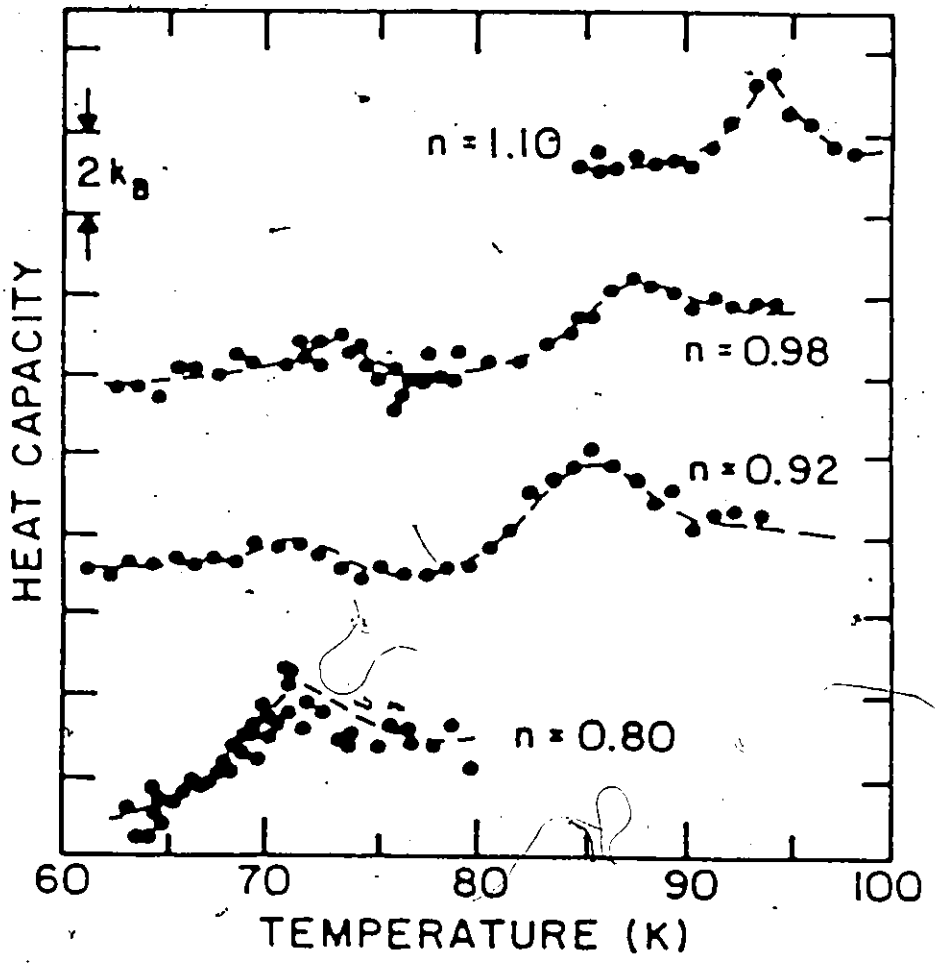

Figure 4.6:

Time evolution of the order parameters for an ethylene monolayer physisorbed on graphite at $T = 53$K and a coverage of $n = 0.9$. The upper curve (a) is the structure amplitude $S(\mathrm{k})$ and the lower curve (b) is the hexagonal order parameter g_6.

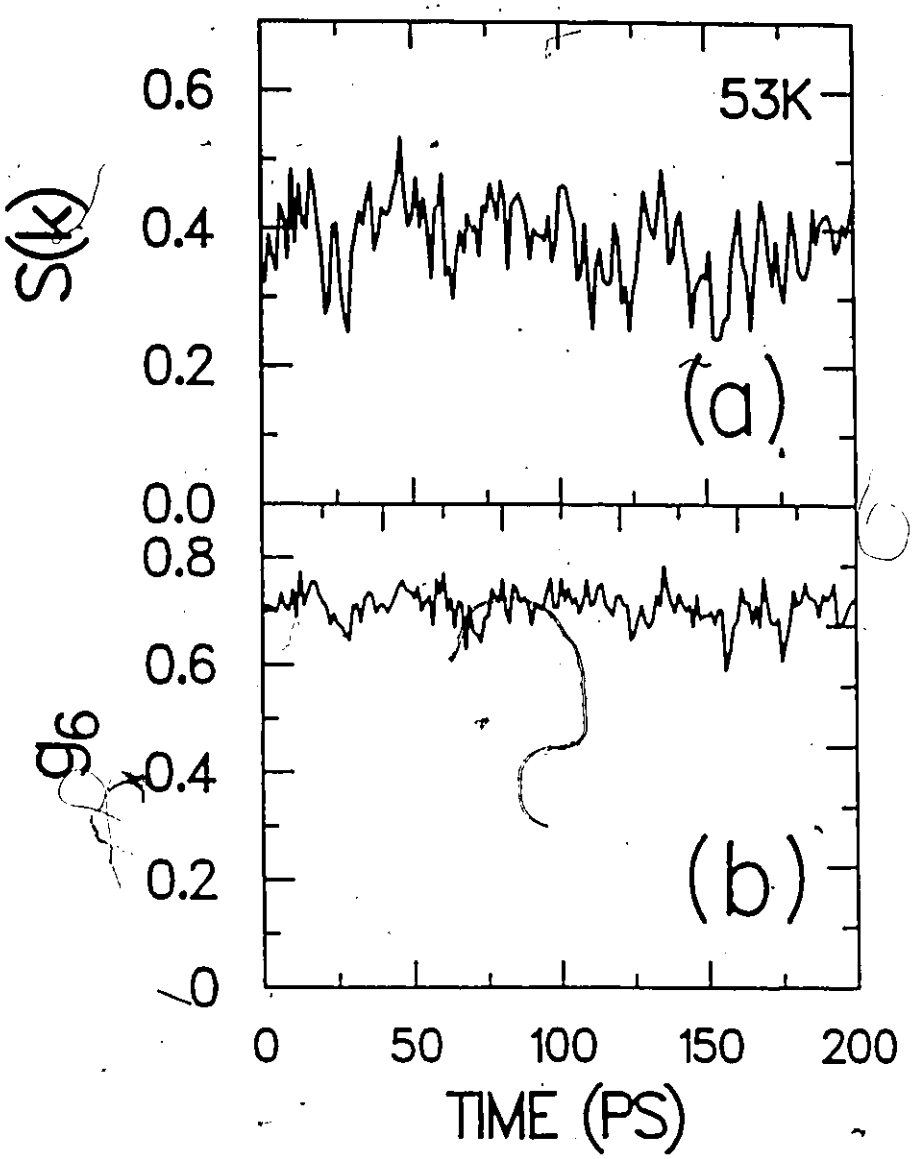

Figure 4.7:

Time evolution of the order parameters for an ethylene monolayer physisorbed on graphite at $T = 63$K and a coverage of $n = 0.9$. The upper curve (a) is the structure amplitude $S(\mathrm{k})$ and the lower curve (b) is the hexagonal order parameter g_6.

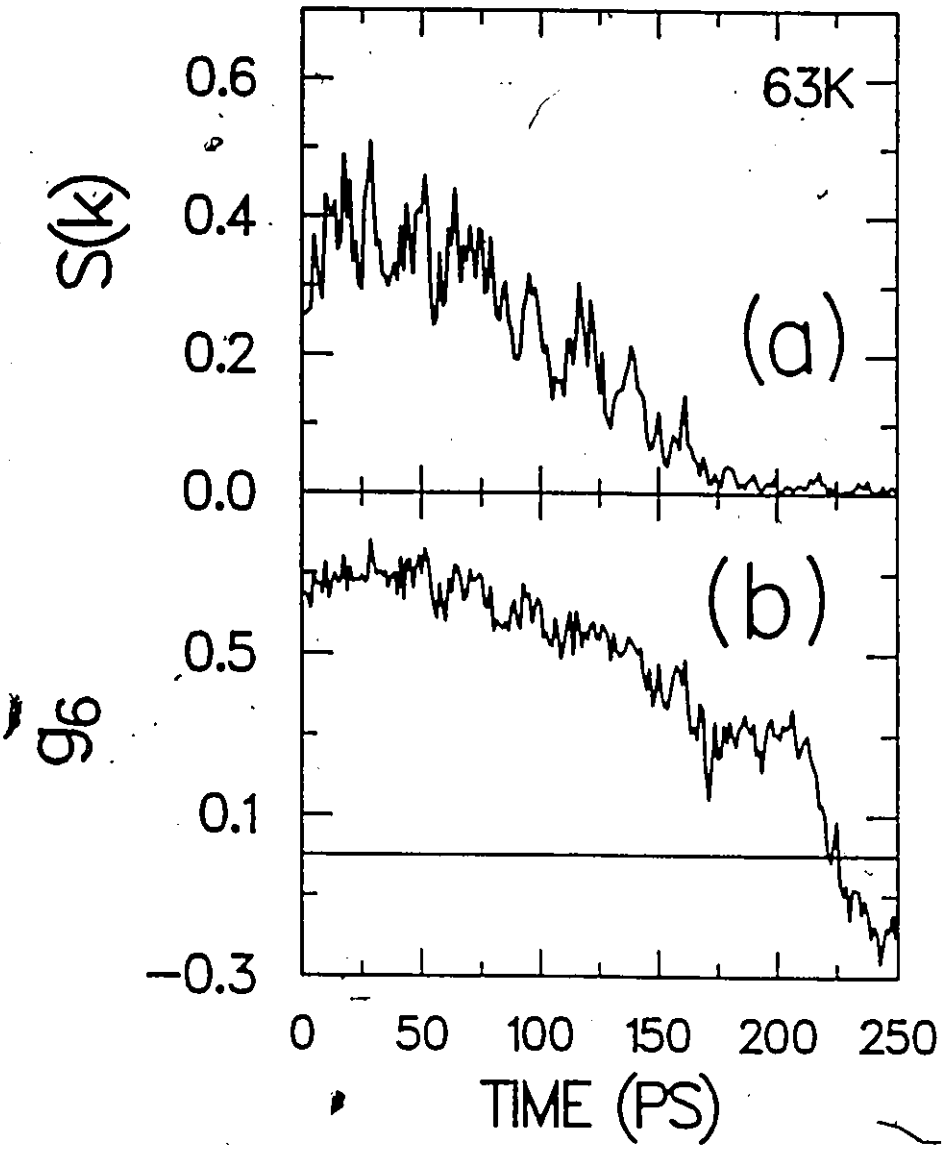

Figure 4.8:

The temperature dependence of (a) the structure amplitude $S(\mathbf{k})$ and (b) the hexagonal order parameter g_6.

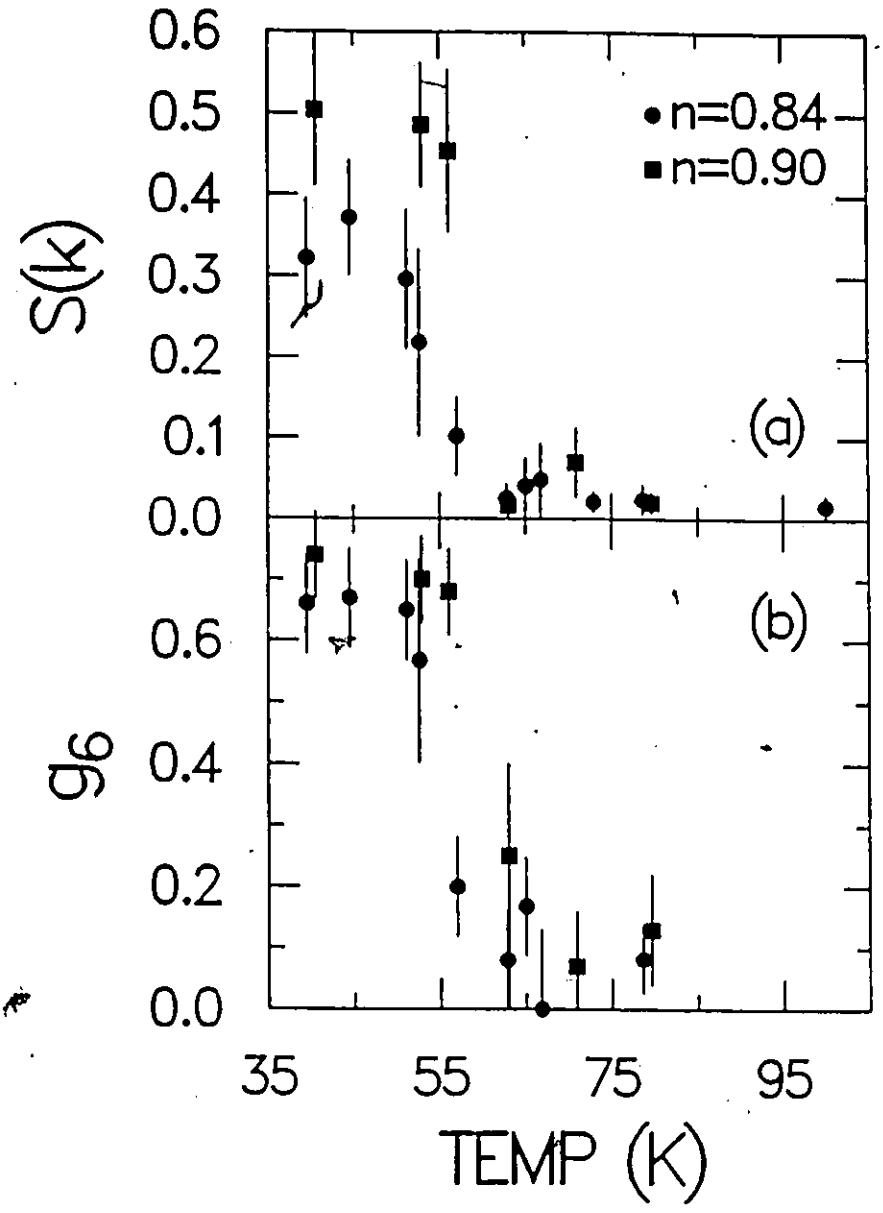

Figure 4.9:

(a) Temperature variation of the translational diffusion coefficient, D_{tr}. (b) Temperature variation of the rotational diffusion coefficients, D_{rot}, for $n = 0.84$. Symbols indicate rotation around the C=C axis (circles), and about orthogonal axes perpendicular (triangles), and parallel (crosses) to the molecular plane.

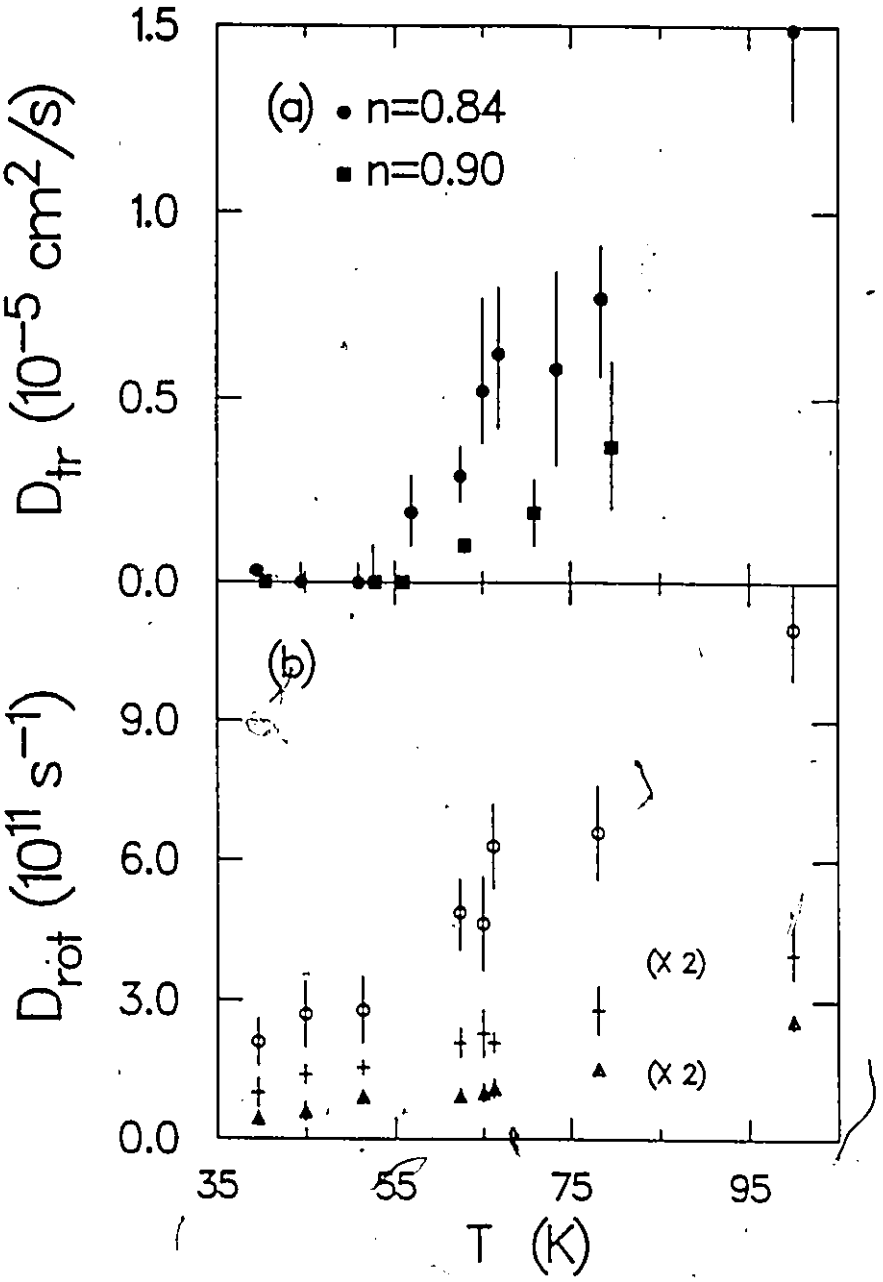

Figure 4.10:

The time evolution of the mean square displacements $\langle[\Delta r]^2\rangle$ of the centres of mass of ethylene molecules at $n = 0.84$ for (a) 53K and (b) 63K. The solid curve represents the complete $\langle[\Delta r]^2\rangle$, and the dashed curve the value after subtraction of the $\langle[\Delta r]^2\rangle$ for the centre of mass of the system.

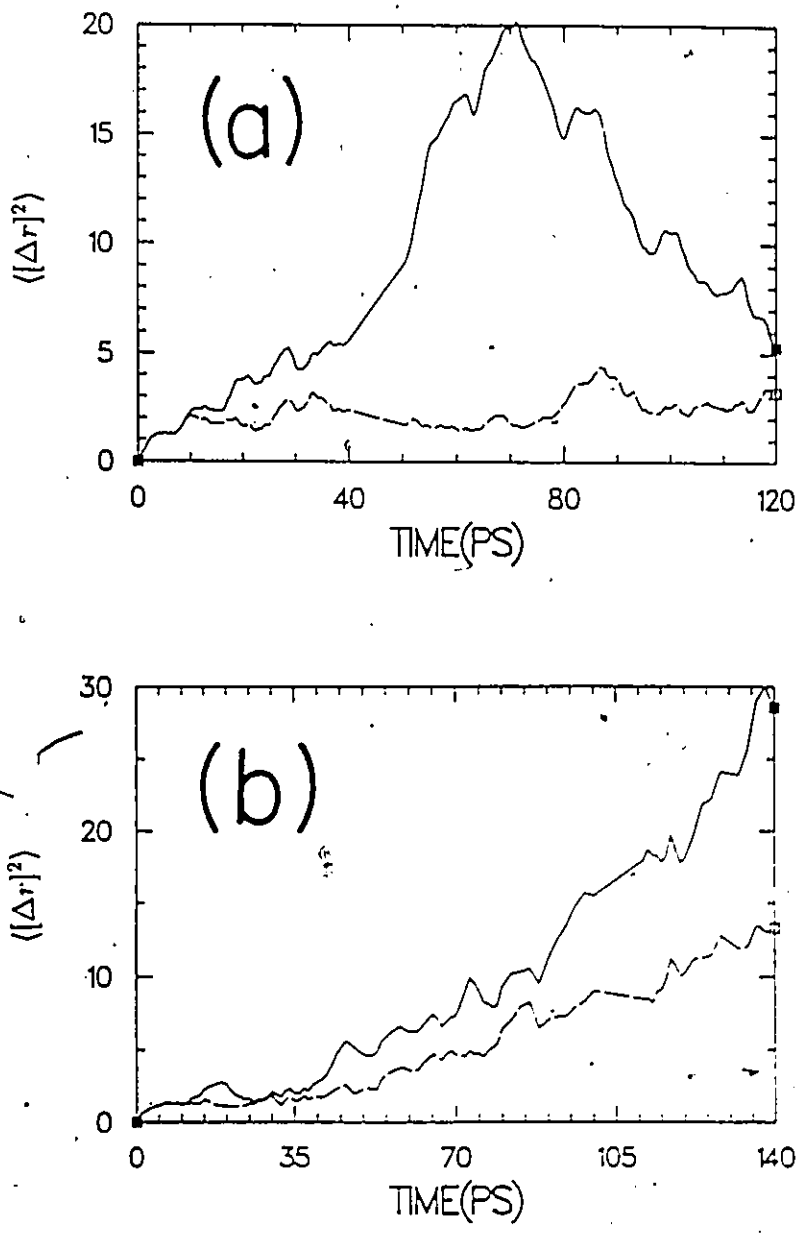

Figure 4.11:

The temperature variation of (a) the molecule-molecule (m-m) and (b) the molecule-surface (m-s) contributions to the average configurational energy, E.

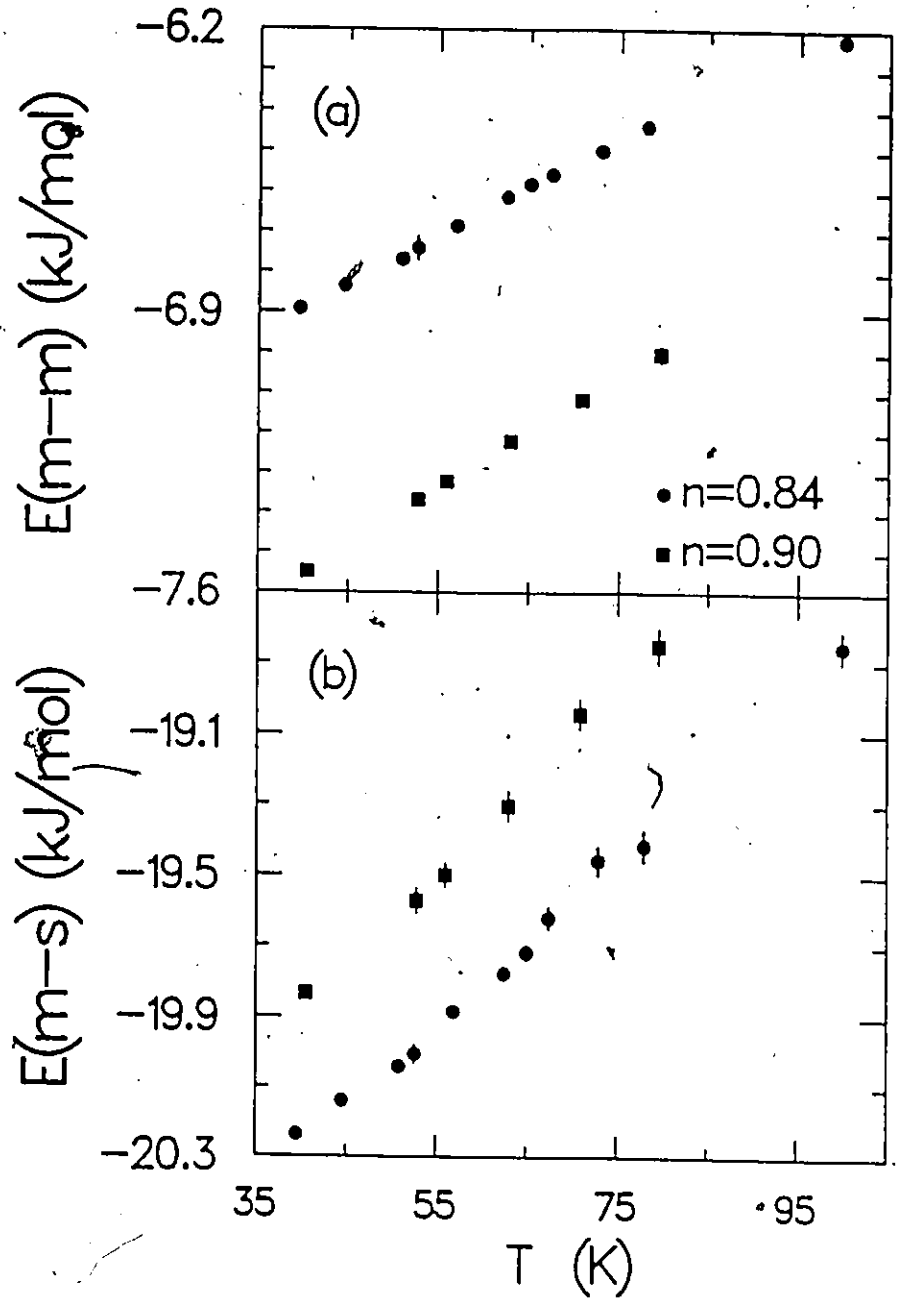

Figure 4.12:

Distribution of tilt angles for ethylene C=C axes away from the plane of the surface at $n = 0.9$ for four temperatures. The solid curve is for the simulation at 53K, the dashed curve at 63K, the chained curved at 71K, and the dotted curve at 80K. Above a tilt angle of 30°, the curves have been multiplied by a factor of 10.

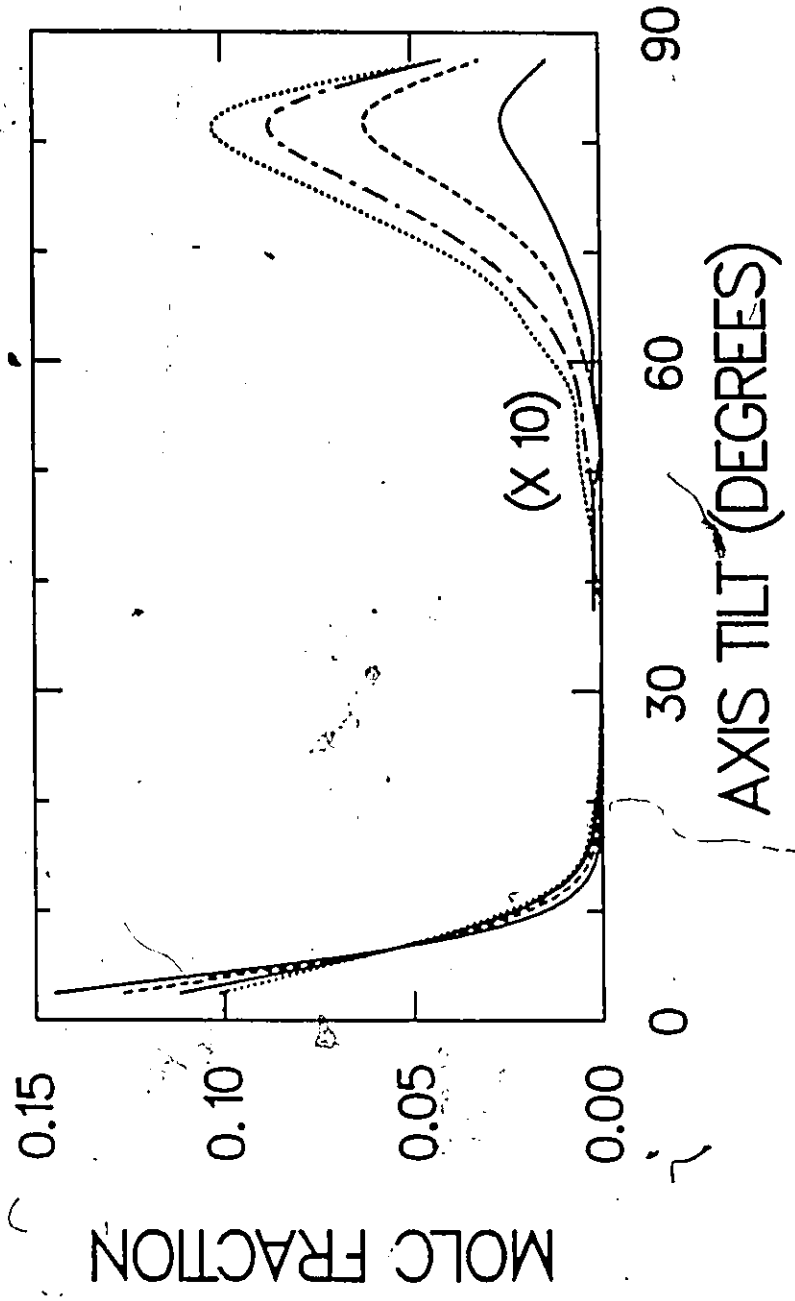

Figure 4.13:

Fraction of standing ethylene molecules (axis tilt greater than 65°) as a function of temperature.

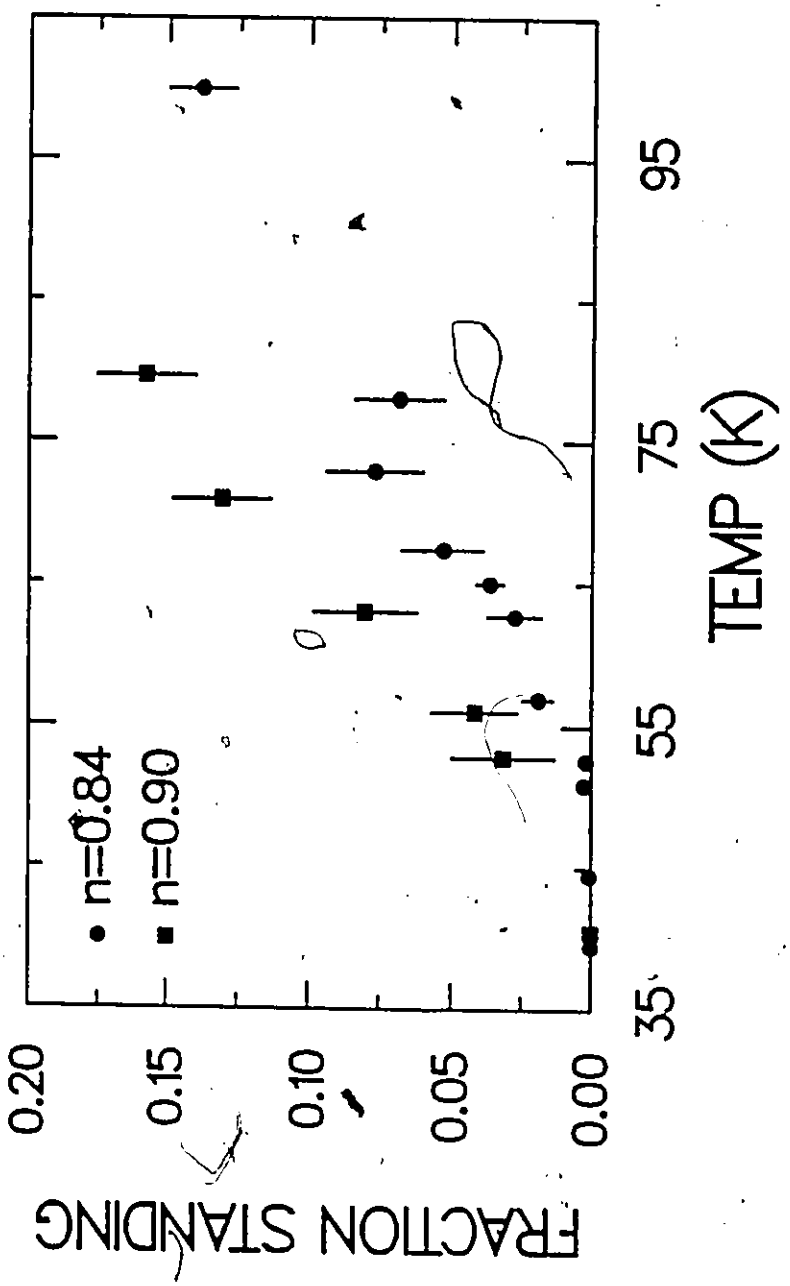

Figure 4.14:

Temperature variation of the translational diffusion coefficient for liquid ethylene physisorbed on graphite at $n = 0.72$. Filled squares represent the simulation data, while unfilled squares represent the QENS data.

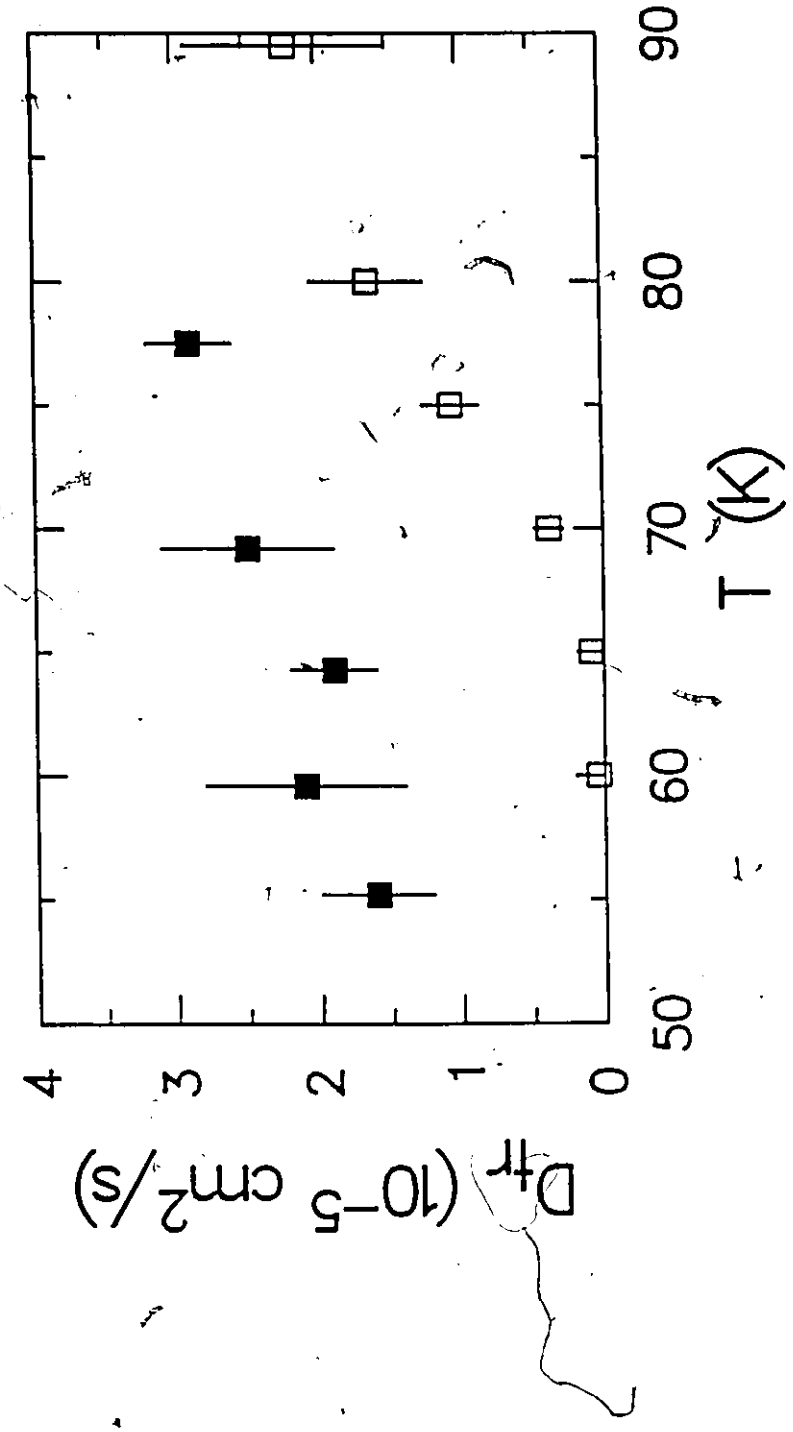

Figure 4.15:

Temperature variation of the rotational diffusion coefficient D_{rot} for liquid ethylene physisorbed on graphite at $n = 0.72$. Filled squares represent the simulation data, while the unfilled squares represent the QENS data.

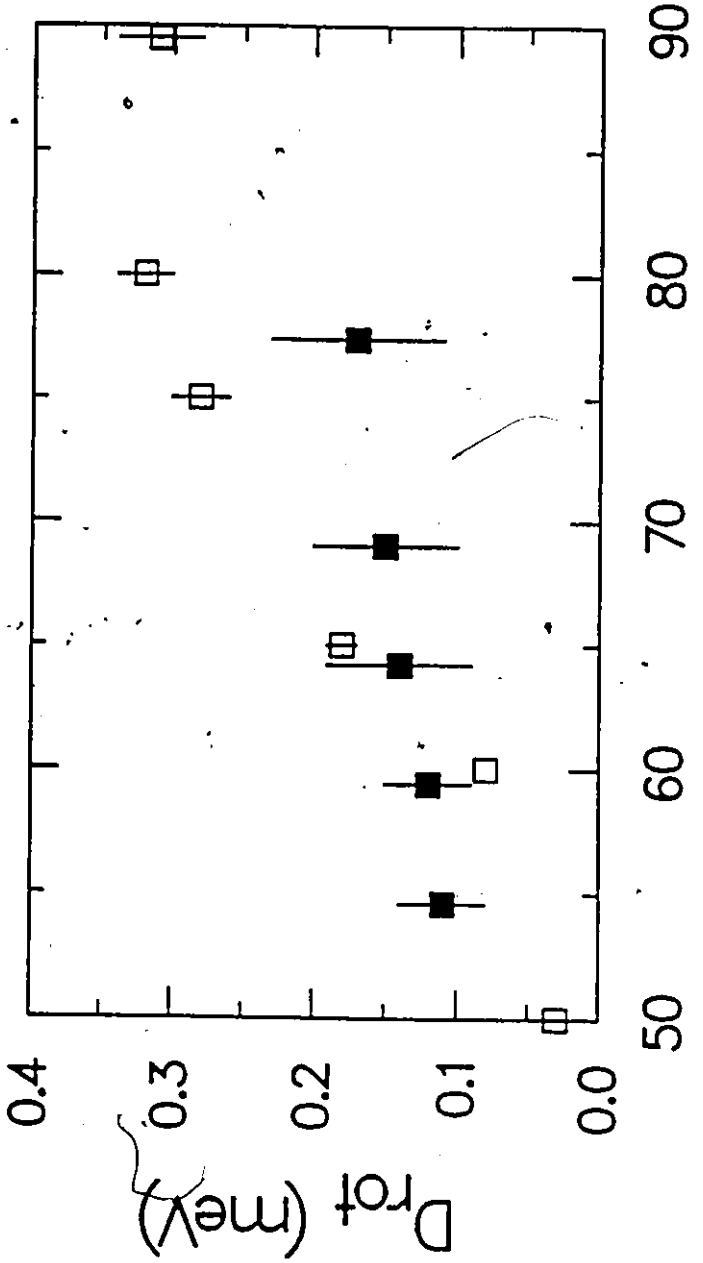

Chapter 5

Ethane on Graphite

5.1 Introduction

The ethane/graphite system has been examined by several experimental methods, including elastic neutron scattering[96,97,98,99], inelastic neutron scattering (INS)[100,101,102,103], and low energy electron diffraction (LEED)[104,105,106]. Progress has also been made theoretically, based on lattice dynamics and energy minimization techniques[99,103].

These experiments have shown that monolayers of ethane form three structural phases at low temperature ($T < 60$K), which are indicated on the phase diagram, presented in Figure 5.1. At coverages below $n = 0.75$ ethane forms the so-called S1 phase: a registered $4 \times \sqrt{3}$ herringbone. Near a coverage of 0.88, ethane forms the S2 phase. Recent LEED experiments[106] suggest that S2 is an incommensurate herringbone with a 5.24Å×7.39Å unit cell, rotated by 5.7° with respect

to the lattice vectors which describe the graphite basal plane. For $0.77 \leq n \leq 0.86$ and $0.9 \leq n \leq 1.00$, two two-phase regions (S1+S2 and S2+S3) exist[11,107]. The range of existence of the pure S2 phase is very narrow, so it is difficult to produce this phase experimentally[108]. At coverage 1.0, ethane forms the S3 phase, which has a commensurate $\sqrt{3} \times \sqrt{3}$ R30° structure.

Energy minimization calculations, using empirical pair potentials[99], suggest that, in the S3 phase, the C—C bonds are aligned perpendicular to the plane of the surface, while in the S1 and S2 phases, the C—C bonds are aligned parallel to the plane of the surface. This is very similar to ethylene on graphite (Sec. 4.3.3), which has a low-density (LD) phase with C=C bonds parallel to the surface, and a high-density phase (HD) with C=C bonds perpendicular to the surface[10,76].

A variety of experiments indicate that, like ethylene, ethane has an orientational ordering transition in the S1 solid phase near 54K, when the molecules begin to rotate about the C—C axis. The S1 phase melts at about 65K to the so-called I1 lattice fluid phase, and the S2 phase melts into a different (I2) phase.

In this study, MD was used to examine the three known solid phases. The purpose was to see if their known structures could be obtained from a simple model using pair potentials. The dynamics of the molecules were also examined, and compared with INS experiments.

5.2 Potentials

The potential parameters used for the simulations of ethane on graphite were the same as the ones used for ethylene. The low temperature structure was investigated for both the Williams and ST potentials. Since parameters of the Williams potential were fitted to bulk properties, the interaction due to the permanent moment of ethane was implicitly included. This was not the case for the ST potential, so the experimental quadrupole moment $Q_{ZZ} = -1.03 \times 10^{-26}$esu cm^2[109] was added to that potential. Ethane has a three-fold axis of symmetry, so only one of the components of the quadrupole tensor $\underline{\mathbf{Q}}$ is independent, namely Q_{ZZ}, where $Q_{ZZ} = -2Q_{XX} = -2Q_{YY}$. The effect of the surface corrugation on the low temperature structure was examined by performing simulations on both the flat and corrugated surface models. In these simulations, the corrugated model of the graphite was used with the anisotropic potential form of Eq.(2.51).

5.3 MD Calculations

The three solid phases (S1, S2 and S3) were simulated first on a flat ($V_1 = 0$) and then on a corrugated ($V_1 \neq 0$) surface. All of the MD calculations were run at 20K for 20ps, after a short (5ps) equilibration period. A timestep of 2.0fs gave excellent energy conservation in this system, where the average deviation in the total energy was less than 3 parts in 10^5.

For the series of simulations on the flat surface, each of the three solid phases was started in its experimentally determined configuration, as found by the scattering

experiments[99,104,105,106]. The simulations of the S1 phase used a system of 11×5 unit cells, or 110 molecules, while the simulations of the S2 phase had 9×6 unit cells, or 108 molecules, and the S3 phase 12×7 unit cells, or 168 molecules. The simulations on the flat surface employed the 2D analogue of the Parrinello-Rahman constant pressure technique (see Sec. 2.2), so the system could relax to its equilibrium structure and surface area[10].

As in the case for ethylene, the simulations on the corrugated surface could not be run at constant pressure, so instead of using a full simulation box, a patch of ethane molecules was placed at the center of a box of fixed area approximately double the size of the patch. The starting configurations for the molecules in these simulations were the equilibrated structures from the MD calculations on the flat surface. Likewise, the starting orientations of the molecules were the average orientations of the molecules on the flat surface.

5.4 Results

5.4.1 Structures

The MD results for the different systems and potentials are compared with each other and with the experimental results in Tables 5.1 and 5.2.

On the flat surface at constant spreading pressure, and with the Williams potential, both the S1 and S2 simulated phases evolved from the initial experimental structures to slightly different herringbones. Table 5.1 lists the MD results for the structures, based on averages over the last 10ps of the 20ps simulations. The S1

herringbone spontaneously expanded along the **a** axis and compressed along the **b** axis (see Figure 5.2), while the S2 herringbone was expanded along the **b** axis. The distortion was relatively small: about 4% in each case. The S3 phase retained the experimental structure on the flat surface, but with the C—C axes tilted slightly away from the vertical. In the absence of experimental evidence, previous workers had assumed a 90° tilt for the molecules[11,99,103]. In all of the simulations, the average center of mass height above the surface $\overline{Z}_{CM}$ was in excellent agreement with the values from energy minimization calculations[103].

The ST potential did not reproduce any of the experimental structures. Table 5.1 lists the results, and snapshots of the configurations at the end of the simulations are presented in Figure 5.4. Each of the phases transformed into denser structures than found experimentally. For S1, the molecules were aligned nearly parallel to each other, as in the δ–phase of O_2[112]. The S3 system remained triangular, but with reduced lattice vectors. The ST potential was fitted to the rotational tunnelling spectrum of CH_4/graphite, and therefore has smaller hydrogen atoms than the Williams potential. This appears to account for the increase in density in the ST simulations, and suggests that rotational tunnelling is not an important effect in ethane monolayers. It is therefore concluded that the ST potential is not appropriate for ethane, since the hydrogen atoms are too small.

The MD simulations on the corrugated surface were run for 20ps, starting from the equilibrated structures of the simulations on the flat surface. The purpose for this was to run long enough to allow for local relaxation of molecular orientations and spacing. The determination of the true equilibrium structure of a patch would

Potl	Solid	Surface	T	Axis	$\overline{Z}_{CM}$	a	b	n
	Phase		(K)	Tilt (°)	(Å)	(Å)	(Å)	
W	S1	Flat	20	12	3.59	4.41	9.48	0.75
W	S1	Corrug	26	7	3.50	4.26	9.84	0.75
ST	S1	Flat	23	12	3.56	4.12	9.29	0.82
Expt[a]	S1		40	10		4.26	9.84	0.75
Calc[b]	S1			8	3.55	3.95	9.60	0.83
W	S2	Flat	40	14	3.58	5.25	7.72	0.78
W	S2	Corrug	21	11	3.56	5.25	7.63	0.78
ST	S2	Flat	22	12	3.56	5.04	7.54	0.83
Expt[c]	S2		40	10[d]		5.24	7.39	0.81
W	S3	Flat	40	82	4.09	4.26	7.38	1.00
W	S3	Corrug	24	80	4.05	4.26	7.38	1.00
ST	S3	Flat	21	85	4.04	4.01	7.05	1.10
Expt[a]	S3		40	90[e]		4.26	7.38	1.00
Calc[b]	S3			90[e]	4.01	4.05	7.01	1.11

[a] Data taken from Ref [99].

[b] Data taken from Ref [103].

[c] Data taken from Ref [106].

[d] Data taken from Ref [110].

[e] Assumed value.

Table 5.1: MD Results for Ethane Structures on Graphite

Potl	Solid	Surface	T	E(m-m)	E(m-s)
	Phase		(K)	(kJ/mol)	(kJ/mol)
W	S1	Flat	20	-7.5	-23.5
W	S1	Corrug	26	-7.4	-24.7
ST	S1	Flat	23	-7.9	-20.1
Calc[a]	S1			-13.6	-20.8
Calc[b]					-20.3
W	S2	Flat	40	-7.7	-23.0
W	S2	Corrug	21	-7.7	-24.0
ST	S2	Flat	22	-8.0	-20.1
W	S3	Flat	40	-9.4	-18.8
W	S3	Corrug	24	-10.1	-19.2
ST	S3	Flat	21	-11.3	-16.5
Calc[a]	S3			-17.4	-17.4

[a] Data taken from Ref [103].

[b] Data taken from Ref [111].

Table 5.2: MD Results for Energies of Ethane on Graphite

likely require a prohibitively long computation, and because the patch was only about 50Å across, might not produce the same structure as experiment, where the patches are likely 1000Å across[77].

The results of the simulation on the corrugated surface are presented in Table 5.1. Figure 5.3 shows snapshots of the systems at the end of the simulations. The S1 phase spontaneously transformed from the 4.41Å×9.48Å herringbone found in the flat surface simulations to the 4.26Å×9.84Å commensurate structure, which is the same structure as found experimentally. In this case, the corrugation has stabilized the structure. The average orientations of the molecules agreed well with energy minimization calculations.[99,103] In the simulations, the molecular axes were tilted 7°±3° away from the plane of surface, compared to 10° in experiment,[99] and 8° in the energy minimization calculations.[99,103] The molecules were, on average, aligned so that they rested on a tripod of hydrogen atoms, as found experimentally.[99]

As might be expected, addition of the corrugation had little effect on the S2 structure, which is incommensurate, or the S3 structure, which was already compatible with the commensurate structure at the end of the flat surface simulation. The calculated molecular orientations for S2 were somewhat different from experiment, due to reorientation of the molecules about their C—C axes. The average axis tilt was 11°±3°, agreeing well with the experimental value of 10°,[110] but they were rotated about 20°±10° around the C—C axis away from the tripod configuration of S1. The simulations of patches on the corrugated surface, therefore, reproduced exactly the experimental structures of the S1 and S3 phases, and produced an S2 phase which was slightly different from experiment.

Examination of Figure 5.3 suggests that, at around 20K, there is little librational or rotational motion of the molecules, except for some libration about the C—C axis. This is consistent with the experimental data, which locates the onset of rotational diffusion about the C—C axis at $T = 54$K[105].

5.4.2 Energetics

There is little calorimetric data available to compare with the results for the molecule-surface potential energy, *E(m-s)*, or the intermolecular potential energy, *E(m-m)*. Bezus *et al*[113] found a zero-coverage isosteric heat of adsorption, $q_{st}(0)$, of -18 kJ/mol for ethane on graphitized carbon black at a relatively high temperature (173K). Isotherms from LEED data yield a heat of condensation for the I1 liquid phase (*cf.* Figure 5.1) of -24.7 kJ/mol[114]. This represents an upper bound for the heat of adsorption, since the heat of fusion of the S1 phase is missing. These experimental results are all greater than the MD results and the energy minimization calculations of Hansen and Taub[103]. The difference in $q_{st}(0)$ between ethylene and ethane has been measured at 1.3 kJ/mol[113]; an observation that seems reasonable, since the polarizability of ethane is larger than for ethylene[115]. In the energy minimization calculations of Battezzati *et al*[111], ethane was more strongly bound to the surface than ethylene, by about 2 kJ/mol, while for the Williams potential, the difference is about 3 kJ/mol. Since the measured and calculated values of $q_{st}(0)$ for *ethylene* were in excellent agreement[116,84], it seems unlikely that the calculated values for the Willams potential in Table 5.2 (-23.5 kJ/mol on the flat surface) will be very wrong.

Measurements of LEED isotherms yielded a heat of condensation for the S3 phase of -31 kJ/mol[114]. This compares to the calculated value of -28.2 kJ/mol for the sum of *E(m-s)* and *E(m-m)* on the flat surface, and the value -34.8 kJ/mol for the energy-minimization calculations[103].

For the simulations on the corrugated surface, the values of *E(m-s)* and *E(m-m)* (which was adjusted to approximately eliminate edge effects in the patch) are very similar to the values for the flat surface. The major difference is a slight increase of about 1 kJ/mol in the magnitude of *E(m-s)*, which represents the nestling of the molecules into the preferred adsorption sites of the corrugation.

5.5 Dynamics of the Solid Monolayer

5.5.1 Diffusion

There was no translation diffusion occurring in the solid monolayer structures at 20K, even in the patches. This was a good indication that the systems were indeed solid. The value of the translational diffusion coefficient D_{tr} calculated from the mean square displacements of the molecules over the last 10ps of the simulations was zero to within associated error. On the corrugated surface, the values of D_{rot}, calculated from the integral of $C(t)$ over time, as described in Sec. 2.2, were also found to be statistically insignificant.

5.5.2 Phonons

The dynamics of the ethane molecules (vibrational phonons and librations) were calculated from the velocity autocorrelation functions, as described in Sec. 2.2. Figure 5.5 shows the velocity ACF $Z_\alpha(t)$ and angular velocity ACF $C_\lambda(t)$ for the S1 phase. Here, λ corresponds to rotation about the molecular C—C axis (R_X), rotation about an axis perpendicular to the molecular axis, and passing through a plane containing the two carbon atoms and two of the hydrogen atoms (R_Z), and rotation about an axis perpendicular to the other two (R_Y). Translational motion in the X-direction is labelled as T_X, in the Y-direction as T_Y, and in the Z-direction as T_Z. Figure 5.5 shows that all of the motions except T_Z are uncorrelated after only 2ps. Therefore, calculations of $Z_\alpha(t)$ and $C_\lambda(t)$ were cut off at this point. In the S1 phase, the X and Y axes are aligned primarily parallel to the plane of the surface, and the Z axis is perpendicular to the surface. However, because of librational motion about the X-axis, the orientations of the molecular Y and Z axes are not constant throughout the simulations. The power spectra $Z_\alpha(\omega)$ and $C_\lambda(\omega)$ for the S1 phase are shown in Figure 5.6. These power spectra suggest the presence of translation-rotation coupling in the S1 phase. The T_Z and R_Z spectra are very similar, with a common peak at about 90cm^{-1}, indicating a coupling of the phonon and libron modes. The corresponding power spectra for the S2 and S3 phases are shown in Figure 5.7 and Figure 5.8 respectively. They also show evidence of translation-rotation coupling.

Power spectra were also calculated for the velocity autocorrelation functions of the hydrogen atom motions for comparison to the INS spectra in Figure 5.12. These spectra were measured for momentum transfer parallel ($Q_{||}$) and perpendic-

ular ($Q_\perp$) to the graphite basal plane[103]. The peaks in the INS spectra and the calculated hydrogen atom power spectra were identified by comparison with the calculated molecular translational and rotational power spectra. Table 5.3 lists the peak positions and resulting assignments.

Figure 5.9 shows the calculated spectrum $Z_H(\omega)/\omega$ for the simulations of the S1 phase on corrugated graphite. For $Q_\parallel$, the simulations reproduce well the main experimental scattering peak at 50 cm^{-1}, which corresponds to T_X, and T_Y in the simulations. The calculated peak at 160 cm^{-1} (R_X, R_Z) likely corresponds to the experimental peak at 110cm^{-1}. For $Q_\perp$, the experimental spectrum is almost identical to $Q_\parallel$. This has been attributed to the mosaic spread (random orientations of the crystallites in the sample)[103]. The calculated $Q_\perp$ is also similar to $Q_\parallel$, but includes a large peak from T_Z which is absent in the experimental spectrum. These spectra also agree well with those derived from lattice dynamics calculations, listed in Table 5.3.

Figure 5.10 shows the calculated power spectrum for the S2 phase. Although this spectrum resembles that for S1, it is not identical. As is the case for the experiments, the high frequency peaks are shifted to slightly lower frequencies compared to S1. However, unlike experiment, the low frequency peak is also shifted to lower frequency, an effect which is likely due to the lower density in the MD simulation (*cf.* Table 5.1).

Figure 5.11 shows the calculated power spectrum for the S3 phase. Now the peaks are shifted to higher frequencies, as is also seen in the experimental spectra. The latter consists of one very broad peak extending from 60 to 90 cm^{-1}, while the

Phase	Polarization	Mode	INS[a]	LD[a]	MD
S1	$Q_{\parallel}$	T_X,T_Y	55,70	50	55
		R_X,R_Z	110	120	160
	$Q_{\perp}$	R_Y	50,70		70
		T_Z	110		95
		R_X,R_Y	110	120	160
S2	$Q_{\parallel}$	T_X,T_Y,R_Z	50,70		20-70
		R_Y	100		120
		R_X			145
	$Q_{\perp}$	T_Z	50,65,100		95
		R_Y			120
		R_X			145
S3	$Q_{\parallel}$	T_X			10
		T_X,T_Y,R_{XYZ}	60,85	85,150	70,95
	$Q_{\perp}$	T_Z	70	85	85

[a] Data taken from Ref [103].

Table 5.3: Peak positions (in cm^{-1}) and assignments for INS, lattice dynamics (LD) and molecular dynamics (MD).

calculated spectrum has its main peak ($T_Y + R$) centered at 95 cm^{-1}. The calculated spectrum also has a large peak (T_X) at 10 cm^{-1}, which corresponds to a collective translation in the X-direction by the entire layer. This motion can also be seen in Figure 5.3. The presence of this peak, which is a low frequency translational phonon, is likely due to the use of a small patch of molecules. Experimentally, $Q_{\|}$ is again identical to $Q_{\perp}$, while there is a significant difference in the calculated power spectra. For perpendicular motion, the main peak, calculated to be at 83 cm^{-1}, is due to T_Z, while the shoulders are ($R_X + R_Y + R_Z$). The position of the T_Z peak exactly corresponds to that found in lattice dynamics calculations, while the calculated peak positions for the other modes are at lower frequencies (*cf.* Table 5.3).

5.6 Conclusion

Molecular dynamics simulations of ethane on graphite were performed on both a flat surface and a corrugated surface. They indicated that the surface corrugation appears to be responsible for the stability of the observed structure of the S1 phase. The calculations with the W potential yielded excellent agreement with the experimentally determined low temperature structures for S1 and S3, and also predicted a herringbone for the S2 phase. However, the calculated unit cell (5.25Å×7.63Å) for the incommensurate S2 phase was slightly expanded in the b direction from the experimental unit cell of (5.24Å×7.39Å). The calculated power spectra for the S1 and S3 phases were in good agreement with the experimental INS spectra and lattice dynamics calculations. The power spectra for the simulated S2 phase had phonon

frequencies which were too low, relative to experiment. This is likely due to the fact that the calculated structure is less dense than experiment. The success achieved for the S1 phase suggest that it will be useful to extend this MD study of the low temperature structure and dynamics to investigate phase transitions, namely the rotator transition, and particularly the melting, which recent experiments suggest may be continuous.[95]

Figure 5.1:

Phase diagram for ethane physisorbed on graphite, taken from Reference [105]. The symbols represent the following phases: commensurate herringbone (S1), incommensurate herringbone (S2), commensurate structure with C—C axes perpendicular to the surface (S3), lattice fluids (I1 and I2), as well as liquid (L) and hypercritical fluid (F).

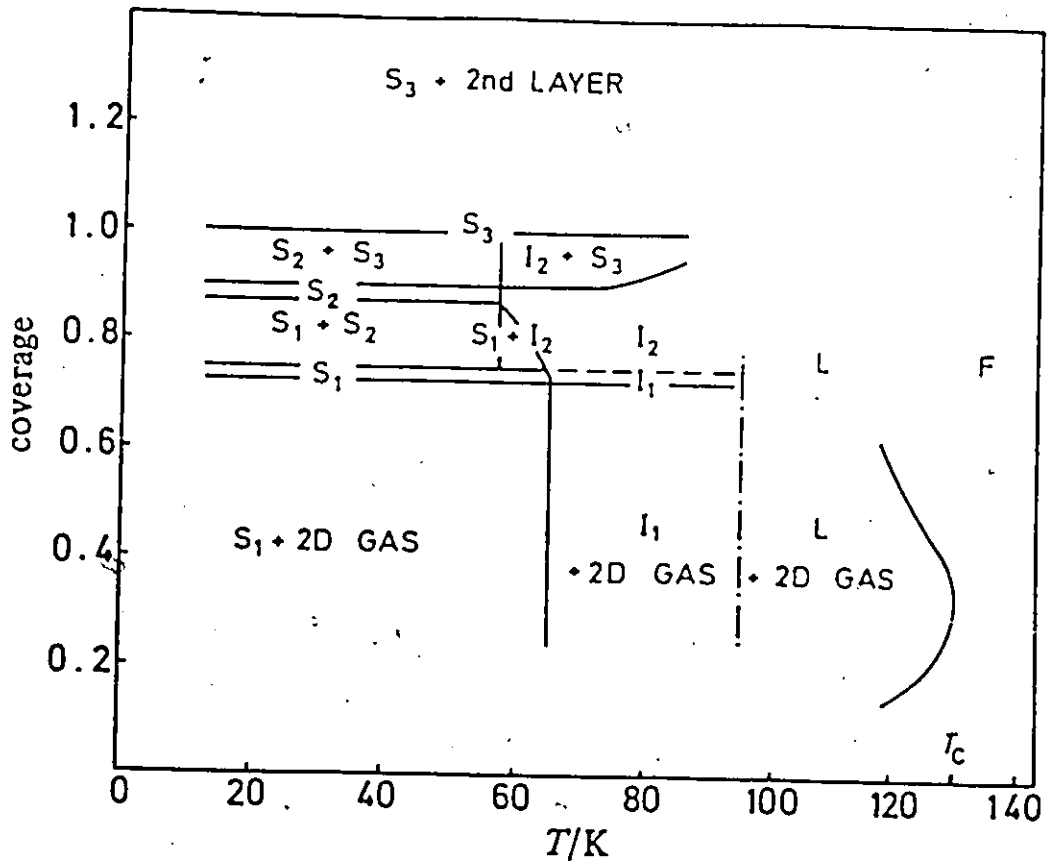

Figure 5.2:

Snapshots of ethane at the end of the simulations on the flat surface model: (a) the S1 phase, (b) S2 and (c) S3.

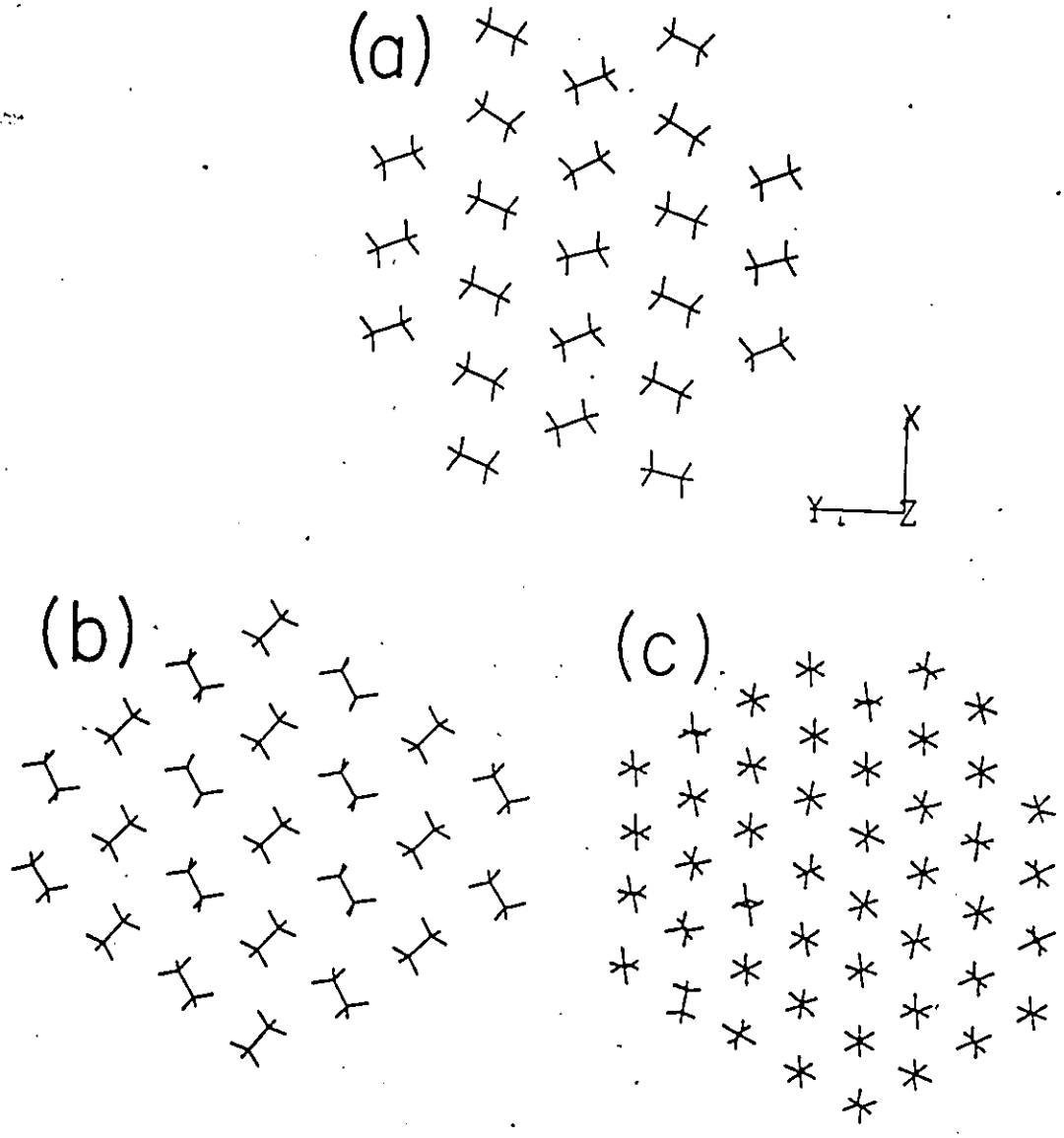

Figure 5.3:

Snapshots of ethane at the end of the simulations on the corrugated surface model: (a) the S1 phase, (b) S2 and (c) S3. The dots represent the carbon atoms in the first layer of the graphite.

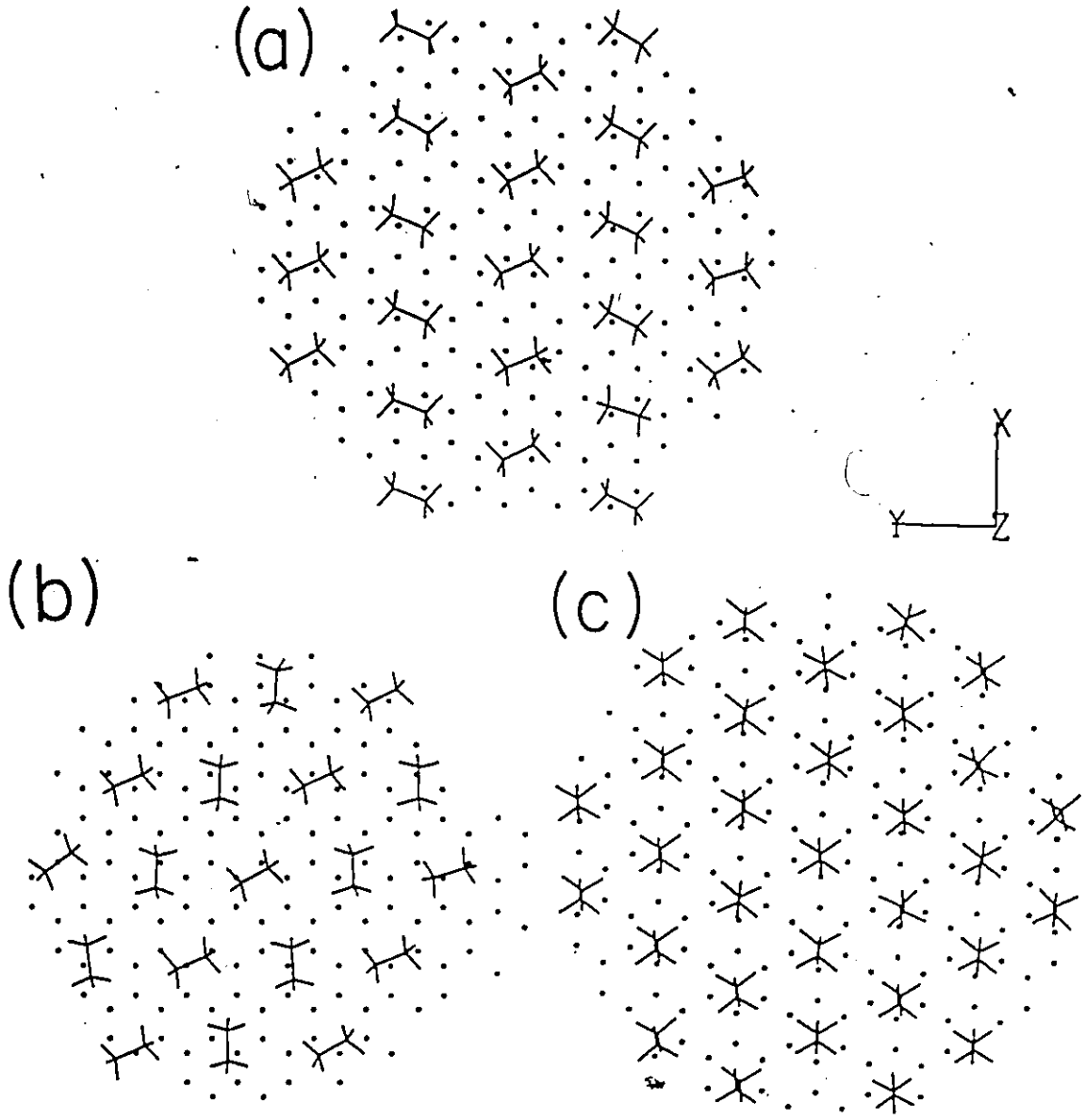

Figure 5.4:

Snapshots of ethane at the end of the simulations on the flat surface model with the ST potential: (a) the S1 phase, (b) S2 and (c) S3.

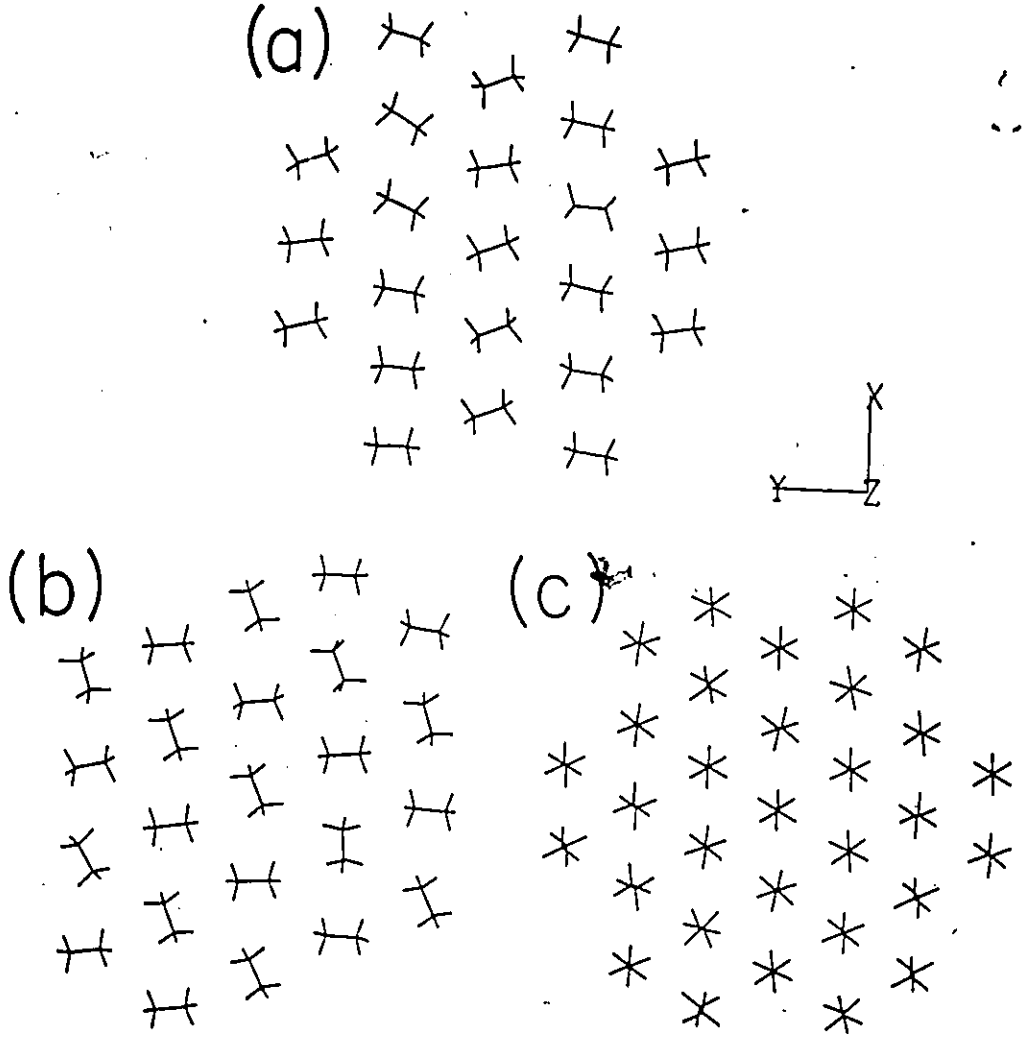

Figure 5.5:

Velocity autocorrelation functions $Z(t)$ and $C(t)$, for the S1 phase of ethane on the corrugated graphite model. The symbols designate: translational motion either parallel (T_X, T_Y) or perpendicular (T_Z) to the graphite basal plane, and rotations about the molecular C—C axis (R_X), about an axis normal to R_X and passing through a plane containing two carbon atoms and two hydrogen atoms (R_Z), and an axis normal to the other two (R_Y).

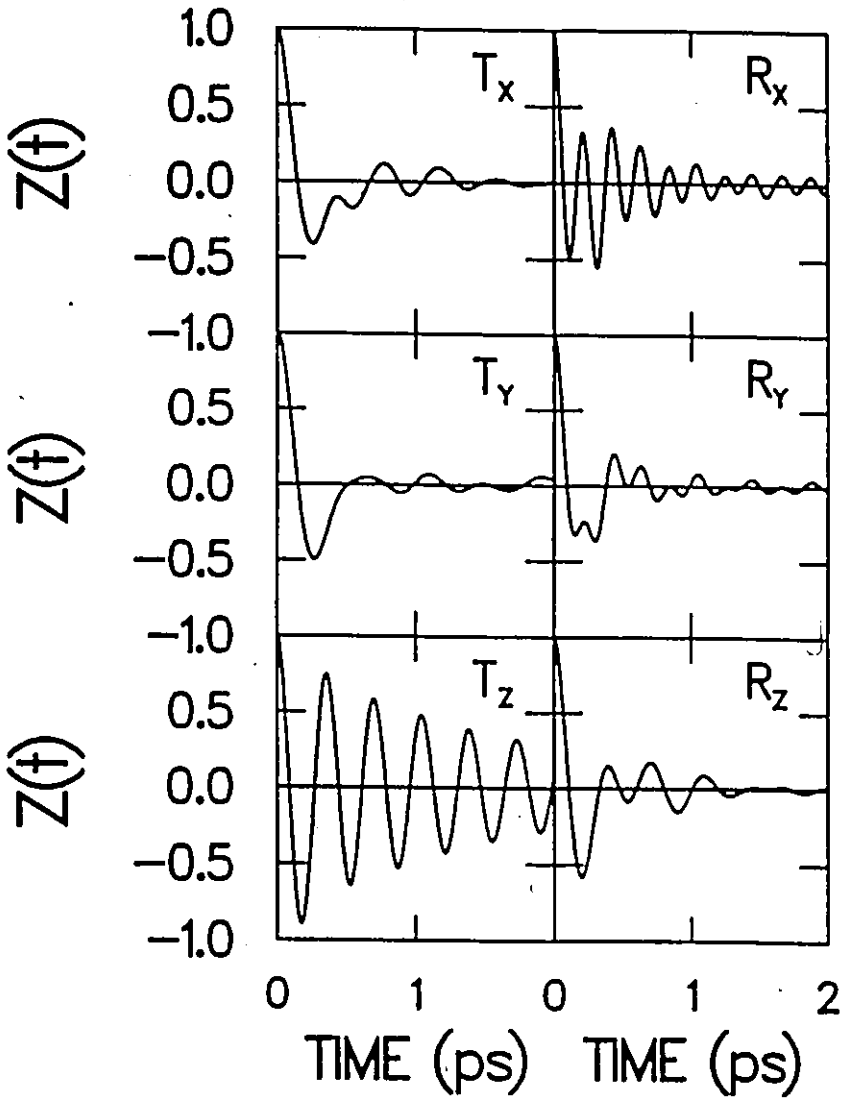

Figure 5.6:

Power spectra $Z(\omega)$ and $C(\omega)$ for the ethane molecular motions in the S1 phase on the corrugated surface. The symbols have the same meaning as in Figure 5.5.

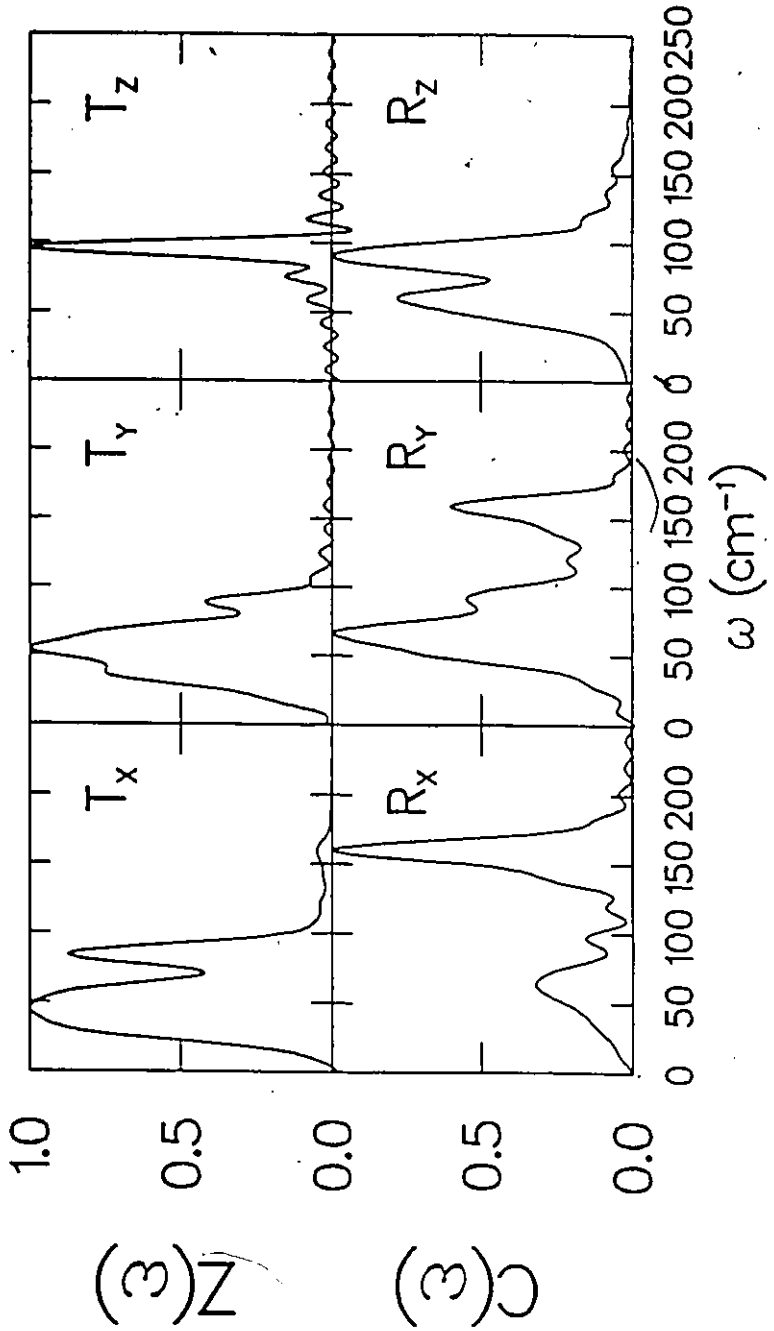

Figure 5.7:

Power spectra $Z(\omega)$ and $C(\omega)$ for the ethane molecular motions in the S2 phase on the corrugated surface. The symbols have the same meaning as in Figure 5.5.

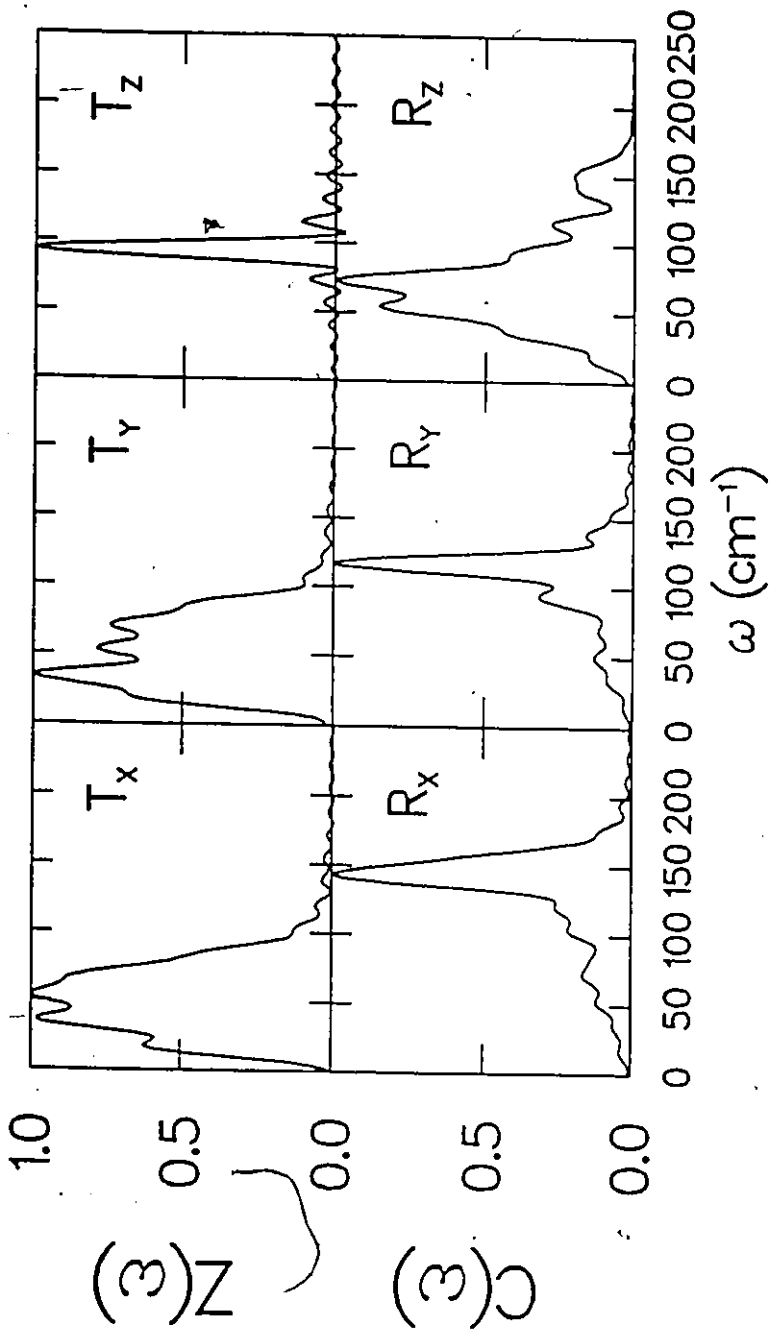

Figure 5.8:

Power spectra $Z(\omega)$ and $C(\omega)$ for the ethane molecular motions in the S3 phase on the corrugated surface. The symbols have the same meaning as in Figure 5.5.

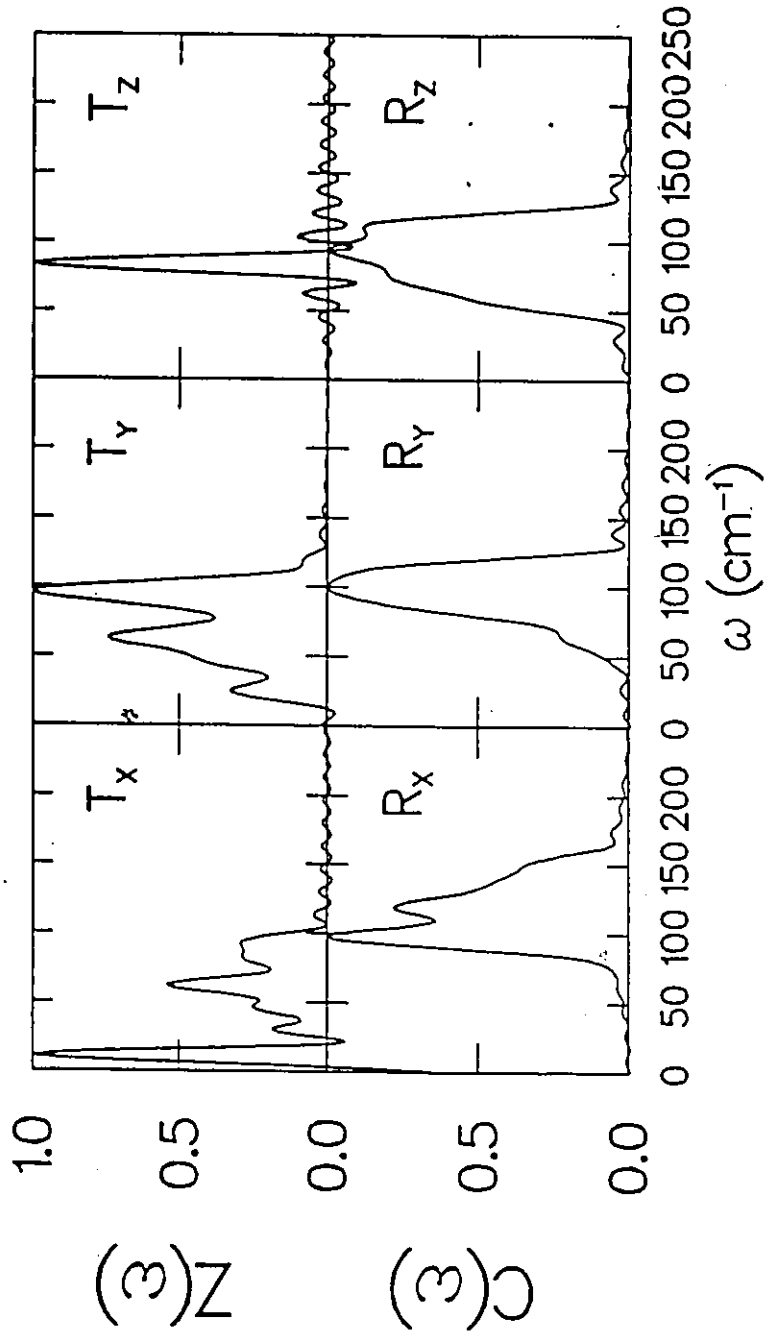

Figure 5.9:

Power spectra $Z_H(\omega)/\omega$ for hydrogen atom velocities in the S1 phase of ethane on corrugated graphite, both parallel (PARAL) and perpendicular (PERP) to the surface plane.

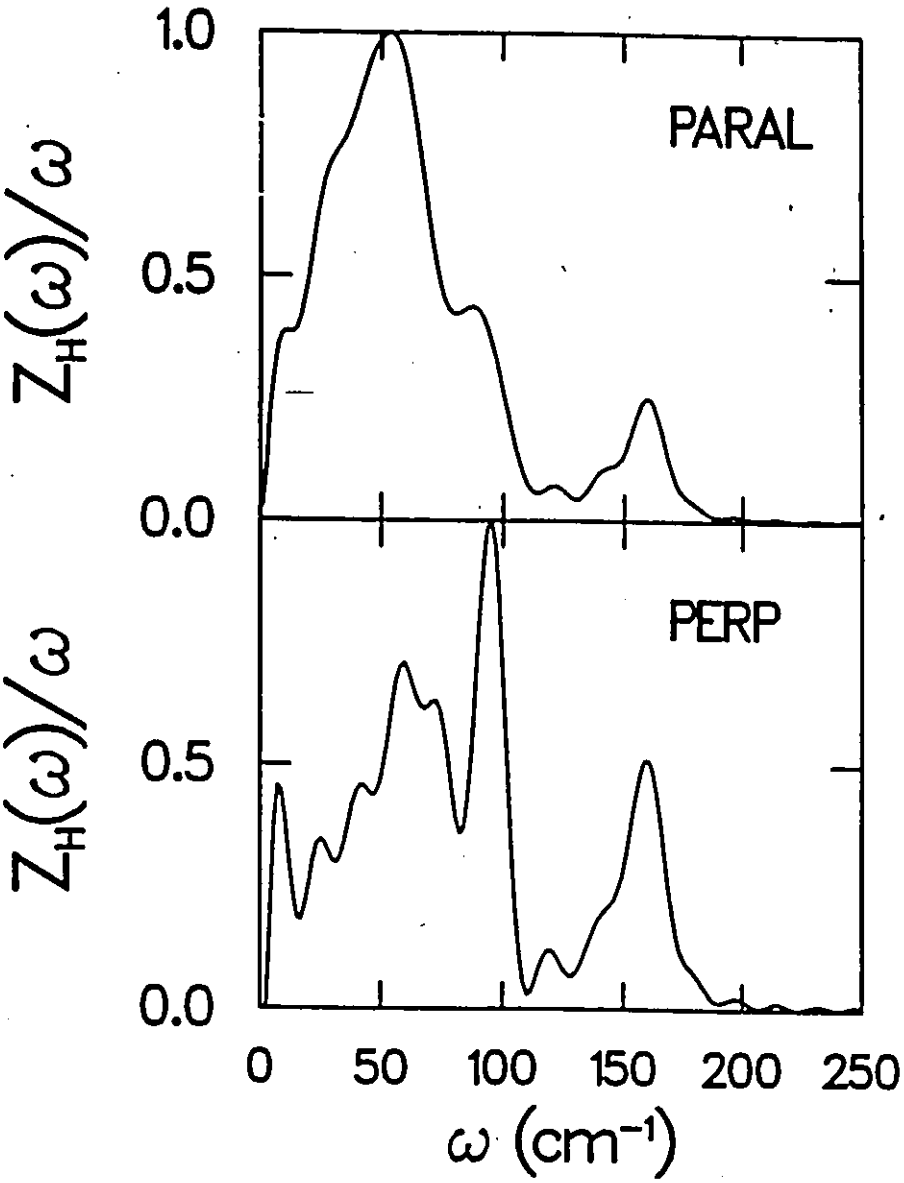

Figure 5.10:

Power spectra $Z_H(\omega)/\omega$ for hydrogen atom velocities in the S2 phase of ethane on corrugated graphite, both parallel (PARAL) and perpendicular (PERP) to the surface plane.

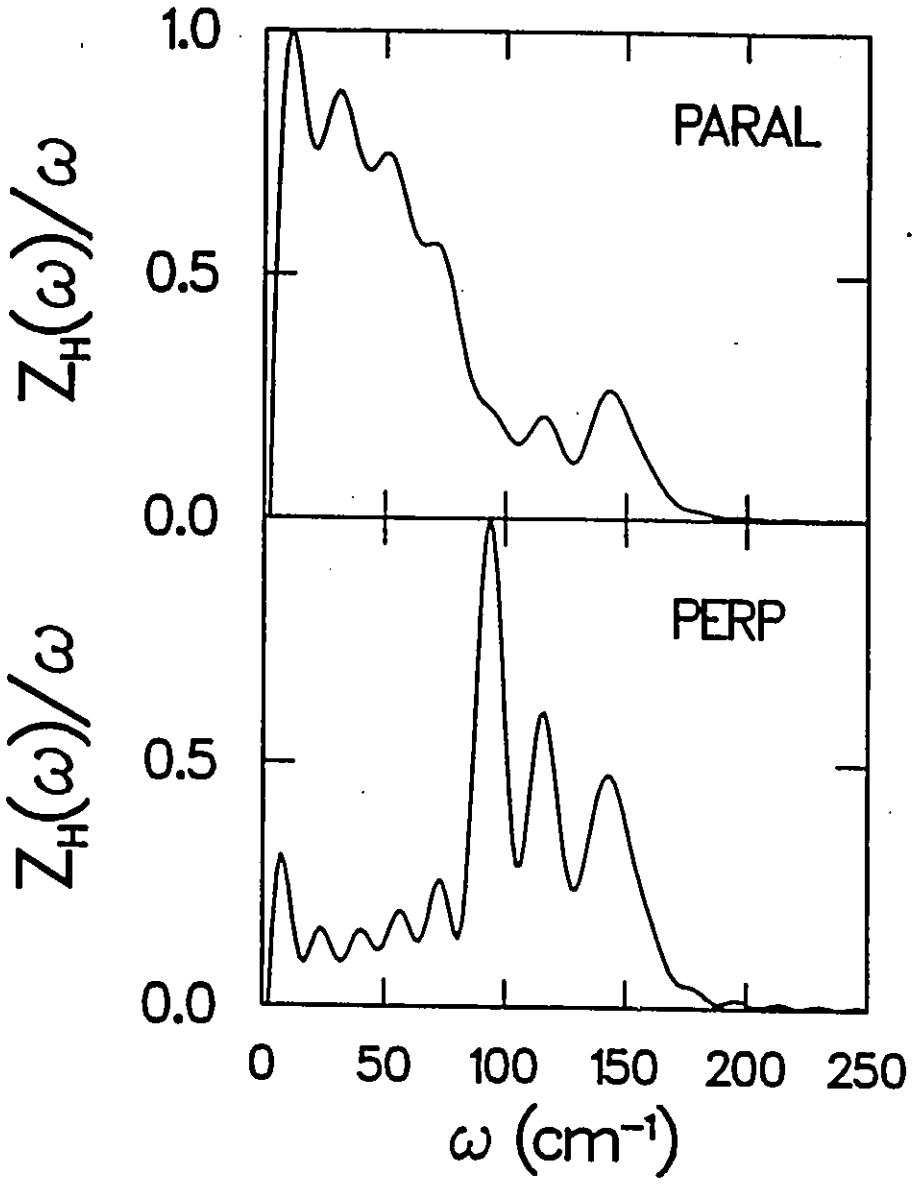

Figure 5.11:

Power spectra $Z_H(\omega)/\omega$ for hydrogen atom velocities in the S3 phase of ethane on corrugated graphite, both parallel (PARAL) and perpendicular (PERP) to the surface plane.

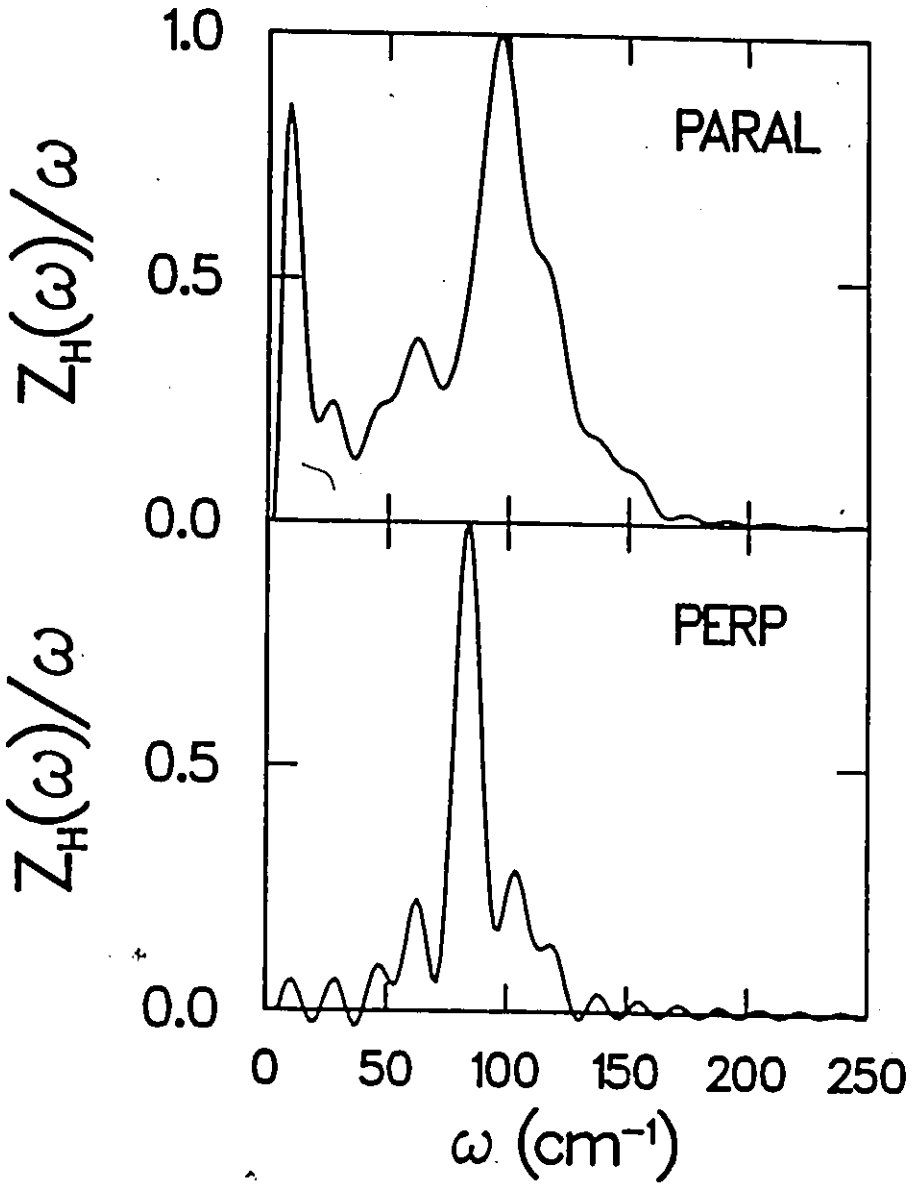

Figure 5.12:

Experimental inelastic neutron scattering spectra for ethylene on graphite, for momentum transfer parallel ($Q_{\|}$) and perpendicular ($Q_{\perp}$) to the basal plane. Taken from Reference[14].

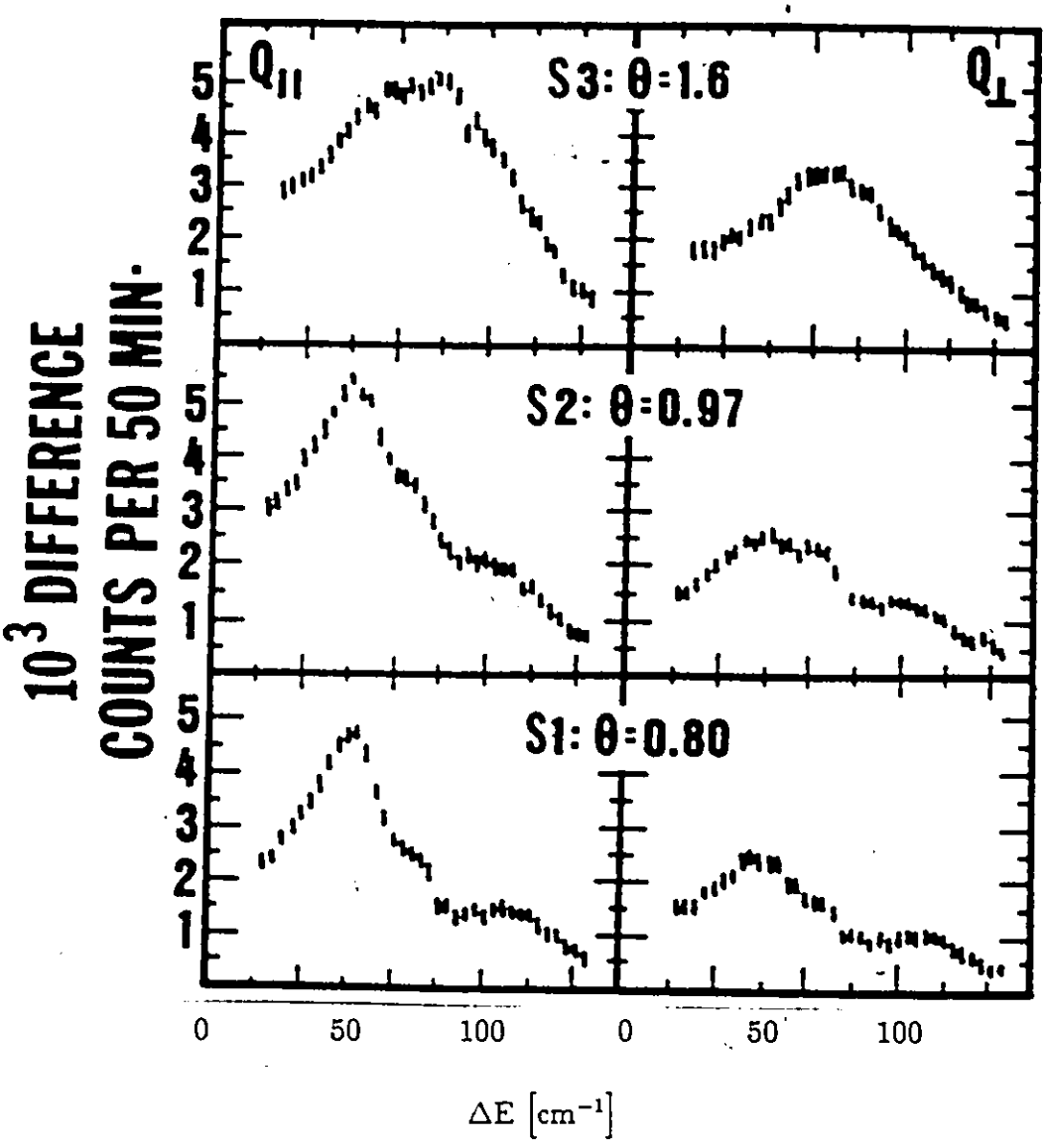

Figure 5.13:

Phonon density of states for S1 as determined by lattice dynamics calculations. Taken from Reference[103].

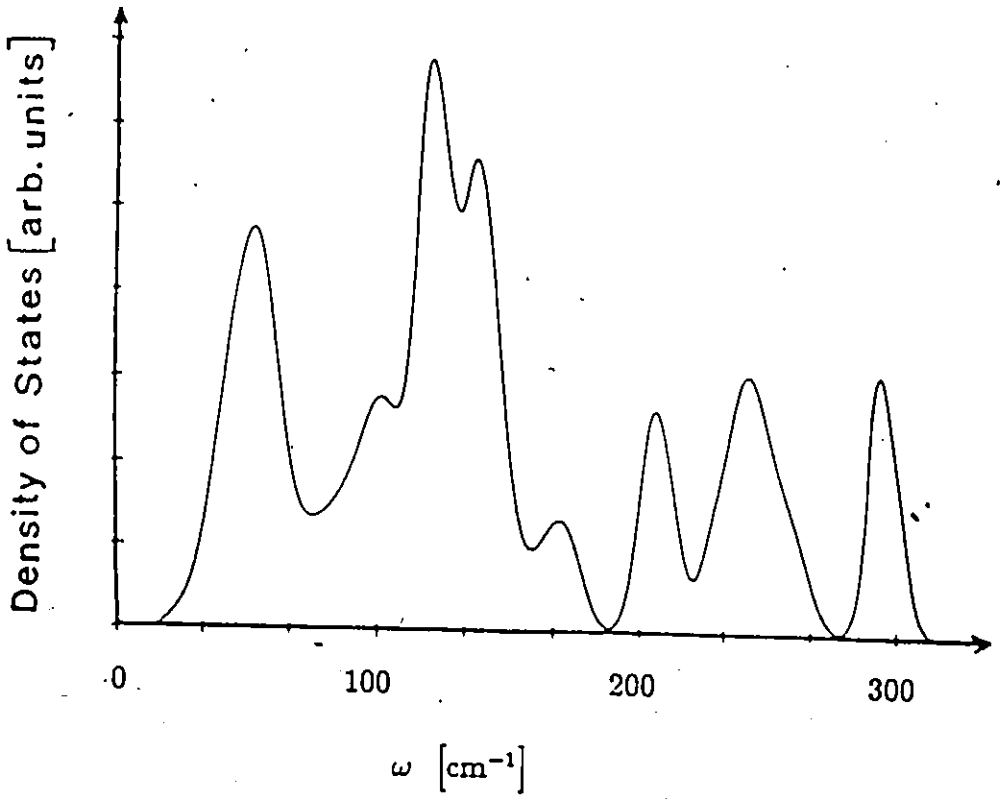

Figure 5.14:

Phonon density of states for S3 as determined by lattice dynamics calculations. Taken from Reference[103].

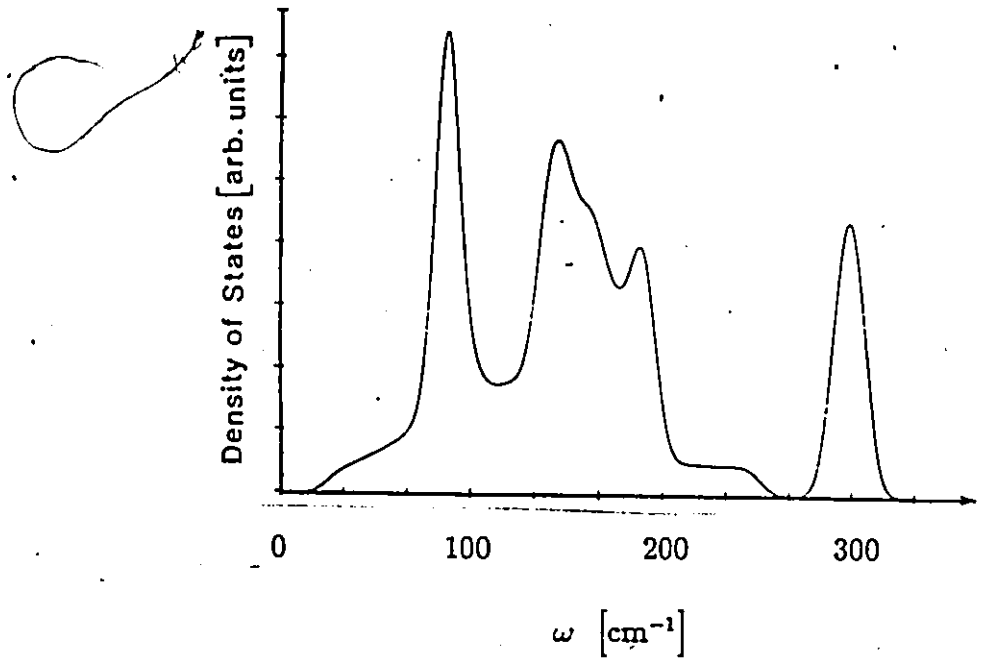

Chapter 6

Polar Molecules

6.1 Introduction

The results for ethane on graphite illustrated how the corrugation of the surface can have a strong influence on the spacing and orientation of the 2D unit cell of an adsorbed layer. Although the structures of the monolayers of a number of simple molecules on graphite have already been examined both by experiment and simulation, very little is known about the adsorbed phases of dipolar molecules on surfaces[117,118,119,120].

Accordingly, the structures of physisorbed layers of the dipolar molecules CH_3F and CH_3Cl were examined by MD simulation. These simulations were carried out in order to complement helium-beam elastic scattering experiments performed by Ruiz *et al*[121,122]. The experiments were performed on two surfaces: the graphite basal plane (Gr), and graphite covered by a complete monolayer of Xe atoms (Xe/Gr).

The Xe layer was adsorbed at at $T < 45$K in order to produce a commensurate $\sqrt{3} \times \sqrt{3}$ R30° layer. In this way, the effect of the size of the corrugation of the substrate on the monolayer structure of the dipolar molecules could be examined.

Helium-beam experiments do not easily give detail on the orientations of the adsorbed molecules, so the MD simulations were performed to suggest possible structures.

6.2 Potentials

6.2.1 Intermolecular Potentials

As in the previous work, the intermolecular potential was taken as the sum of individual atom-atom potentials. The potential parameters for the Xe atoms was taken from Steele[3], and converted to the exp-6 form (see Table 6.1).

The intermolecular potentials of CH_3F and CH_3Cl molecules in the liquid phase have recently been determined by Böhm *et al*[123]. This set of potentials is labelled (A) in the following discussion. The potentials were separated into the first order SCF contribution $E^{(1)}_{SCF}$, and the dispersion E_{disp}:

$$E = E^{(1)}_{SCF} + E_{disp}. \tag{6.1}$$

The form of $E^{(1)}_{SCF}$ is

$$E^{(1)}_{SCF} = \sum_{i,j} \left[\exp\left(-\frac{R_{ij} - \sigma_i - \sigma_j}{\rho_i + \rho_j} \right) + \frac{q_i q_j}{R_{ij}} \right], \tag{6.2}$$

and E_{disp} has the form

$$E_{disp} = -\frac{C_{ij}}{R^6_{ij}} F_{ij} \tag{6.3}$$

where F_{ij} is a damping function for the dispersion:

$$F_{ij} = \begin{cases} \exp[-(1.28R^0_{ij}/R_{ij} - 1)^2] & R_{ij} < 1.28R^0_{ij}; \\ 1 & \text{elsewhere.} \end{cases} \tag{6.4}$$

The parameters of $E^{(1)}_{SCF}$ were taken from *ab initio* SCF calculations, and the parameter C_{ij} of E_{disp} was fitted to the experimental virial coefficient $B(T)$. The values of the parameters σ, ρ and C_{ij} are given in Ref. [124]. The atomic van der Waals radii, R^0_{ij}, were taken from Bondi[125]. This potential was converted to a more convenient form similar to exp-6:

$$u(r) = A\exp(-Br) - \frac{C}{r^6}F_{ij} + \frac{q_iq_j}{r}, \tag{6.5}$$

the following relations were used:

$$A = \exp\left(\frac{\sigma_{ij}}{\rho_{ij}}\right) \tag{6.6}$$

$$B = \frac{1}{\rho_{ij}} \tag{6.7}$$

$$C = C_{ij} \tag{6.8}$$

where $\sigma_{ij} = \sigma_i + \sigma_j$ and $\rho_{ij} = \rho_i + \rho_j$. These parameters are provided in Tables 6.1 and 6.2. The mixing rules:

$$A_{ij} = \sqrt{A_{ii}A_{jj}} \tag{6.9}$$

$$B_{ij} = (B_{ii} + B_{jj})/2 \tag{6.10}$$

$$C_{ij} = \sqrt{C_{ii}C_{jj}} \tag{6.11}$$

$$R^0_{ij} = R^0_i + R^0_j \tag{6.12}$$

were used to calculate the cross-terms (Xe—C, C—F, etc.) for the interactions.

The potentials used partial charges, (q_i), located at the atomic positions, to reproduce the dipole moments. The values of these charges are given in Table 6.3. In the CH_3Cl potential, the charges were shifted slightly away from the atom positions. To incorporate this into the simulation would have required much effort, and so, in this study, the charges listed in Table 6.2 have been placed at the atom sites. This resulted in a different dipole moment (1.89D) from the original potential, so the charges were also scaled up by 4% to recover the original dipole moment of 1.96D. The various charge distributions, and the resulting dipole moments are summarized in Table 6.3.

Another set of potentials for CH_3F and CH_3Cl was constructed from parts of various potentials taken from the literature. In the following discussion, this set of potentials will be labelled (B). Here, the CH_3–CH_3 potential was taken from a methanol potential[126], the F–F potential was taken from a CF_4 potential[127], and the Cl–Cl potential was taken from a CCl_4 potential[128], using the average ϵ_{Cl-Cl} of models I and II. The parameters for this potential are listed in Table 6.4. The partial charges on the atoms were taken from Potential A above, also without the shift on the charges in CH_3Cl.

6.2.2 Molecule-Surface Potential

The graphite surface was modelled with the corrugation, using the isotropic potential form ($\gamma_R = \gamma_A = 0$). The potential parameters for the graphite atoms were taken from Williams[69], and modified by the mixing rules for the interactions with Xe, CH_3F, and CH_3Cl (see Table 6.5). The interaction between the molecular dipoles

Atoms	A(kJ/mol)	B($Å^{-1}$)	C(kJ$Å^6$/mol)	R^0_{ij} (Å)
Xe—Xe	1358000	2.9930	30930	4.32
C—C	6856300	5.2266	1562	3.40
F—F	251460	4.1816	651.5	2.94
H—H	4601	3.3932	193.3	2.40

Table 6.1: Exp-6 Parameters of Potential A for CH_3F

Atoms	A(kJ/mol)	B($Å^{-1}$)	C(kJ$Å^6$/mol)	R^0_{ij} (Å)
Xe—Xe	1358000	2.9930	30930	4.22
C—C	3597800	4.5439	1769	3.40
Cl—Cl	2192300	3.6997	8665	3.50
H—H	6957	3.4875	268	2.40

Table 6.2: Exp-6 Parameters of Potential A for CH_3Cl

Molecule	Atom	q_i	μ (D)
CH_3F[a]	C	-0.2469	
	F	-0.1950	
	H	+0.1473	2.03
CH_3F[b]			1.86
CH_3F[c]			2.04
CH_3Cl[a]	C	-0.3374[d]	
	Cl	-0.1318[e]	
	H	+0.1564[f]	1.96
CH_3Cl[g]			1.89
CH_3Cl[h]	C	-0.3499	
	Cl	-0.1367	
	H	+0.1622	1.96
CH_3Cl[b]			1.86
CH_3Cl[c]			1.98

[a] From Ref.[123].

[b] Experimental value.

[c] SCF value.

[d] Charge shifted by 0.106Å into C—Cl bond.

[e] Charge shifted by 0.074Å into C—Cl bond.

[f] Charge shifted by 0.079Å into C—H bond.

[g] Charges of Ref.[123] on atom sites.

[h] Charge distribution used in this work.

Table 6.3: Charge Distributions Used for CH_3F and CH_3Cl

and their images in the substrate was ignored. However, since the molecules are above the Xe atoms, and thus more than 6Å above the graphite surface, this interaction is probably small. Also, in order to simplify the calculations of the electrostatic interactions, a patch of molecules was employed, rather than a full simulation box.

In all of the simulations, the Xe layer was started in the commensurate $\sqrt{3} \times \sqrt{3}$ R30° structure, and the atom motions were calculated with the same MD algorithm as the CH_3Cl and CH_3F molecules. The atoms of the graphite surface, however, were kept fixed in their equilibrium positions.

6.3 Calculations

The model and integration algorithm used for the equations of motion were the same as for the previous simulations of C_2H_4 and C_2H_6, though with different potential parameters, as described in Sec. 6.2. The simulations were performed on a patch of 168 molecules on top of a layer of 504 Xe atoms, which in turn were placed commensurate with the graphite, in a box which was 89.46Å × 88.54Å. As in the previous simulations, the molecules were assumed to be rigid. Both CH_3F and CH_3Cl have very small moments of inertia (3.25 g/molÅ^2) about their molecular axes (C—F and C—Cl) which would have necessitated a small time step to accurately calculate the resulting rapid rotational motion. Therefore, the H-atoms were replaced by D atoms (of mass 2) in the simulations, increasing the moment of inertia about the molecular axes to 6.5 g/molÅ^2. In this way, the time step could be increased to 2fs without loss of energy conservation, thereby reducing the length of the calculations. This

Atoms	A(kJ/mol)	B($Å^{-1}$)	C(kJ$Å^6$/mol)
Xe—Xe	1358000	2.993	30930
CH_3—CH_3	560300	3.178	8899
Cl—Cl	755900	3.506	6663
F—F	227400	4.159	719

Table 6.4: Exp-6 Parameters of Potential B for Xe, CH_3F and CH_3Cl

Potl	Atoms	ϵ(kJ/mol)	σ(Å)
A	Xe—C(Gr)	0.84580	3.765
A	C—C(Gr)	0.54320	3.646
A	H—C(Gr)	0.23436	2.922
A	F—C(Gr)	0.34600	3.190
A	Cl—C(Gr)	0.63100	3.465
B	Xe—C(Gr)	0.84580	3.765
B	CH_3—C(Gr)	0.54320	3.646
B	Cl—C(Gr)	0.63100	3.465
B	F—C(Gr)	0.34600	3.190

Table 6.5: Lennard-Jones Parameters for the Surface Interactions

did not affect the potential (and thus the structure determined by the simulations), since it only affected the time taken to form the structures. The translational phonon frequencies were shifted by the ratio of the square root of the masses of the deuterated and undeuterated forms. This amounted to a decrease in the frequencies of 4% for CH_3F and 3% for CH_3Cl, shifts which would be undetectable in the calculated spectra. The frequency of rotation about the molecular axes (R_Z) was reduced to half of the value expected for undeuterated molecules.

The simulations were run for some 4000 steps (8ps), and the given data are averages over the last 4ps. The large number of particles in the system (504 atoms and 168 molecules) meant that even such short runs needed a large amount of computer time. These runs were long enough that the molecules could relax to their locally preferred spacings and orientations, but not long enough to determine the equilibrium structure of the patch. The systems were started at 20K by velocity scaling for about 1000 steps (2ps).

6.4 CH_3Cl and CH_3F Bulk Structures

Both potential A and B were tested by investigating the properties of bulk solid CH_3Cl. The MD algorithm was the same is in the above simulations, but extended to three dimensions. The simulations were started in the known crystal structure for CH_3Cl[129]. This structure is isomorphous to the α phase of CH_3Br, in which the molecules are arranged in ferroelectric-aligned inclined chains. This structure, shown in Figure 6.1, has the space group $Cmc2_1$, with two molecules per unit cell.

CH_3Br also forms a second (β) phase at low temperature, shown in Figure 6.2, which is isomorphous with the structure of CH_3I. This phase consists of chains of molecules arranged in antiferroelectric order. The space group is *Pnma*, with four molecules per unit cell. A simulation was also performed on CH_3Cl arranged in this structure, as a check of the potentials.

For the simulations in the α–structure, the values of the unit cell lengths were taken from the X-ray diffraction data of Burbank[129], while keeping the gas-phase values for the bond lengths and angles in the molecule. Since CH_3Cl does not form the β–structure, the appropriate unit cell lengths and molecular orientations are unknown. Therefore, the simulation done on CH_3Cl in the β–structure started with the CH_3Cl molecules arranged with the experimentally determined spacing and orientation for CH_3Br molecules. The simulation was originally set up with the CH_3Br unit cell lengths, and then they were adjusted until they gave small positive stress tensor values in the simulated solid. The simulations of both solid structures were run for 6ps at constant pressure, after a short equilibration (1ps) to 100K at constant volume.

For the α–structure, the average potential energy in the simulations was found to be -33kJ/mol for potential A and -23kJ/mol for potential B. The estimated experimental value is -27kJ/mol. For the β–structure, the potential energy was -32kJ/mol for potential A, and -22kJ/mol for potential B. In the case of the α–phase simulations, the molecules retained the starting structure (with orthorhombic unit cell 6.5Å×5.1Å×7.5Å) throughout the length of the constant pressure runs. However, in the β–phase, the unit cell spontaneously deformed from 4.4Å×6.3Å×9.0Å to

4.1Å×6.5Å×9.5Å, while staying orthorhombic.

The α–structure is more stable for CH_3Cl for both potentials. Also the potential energy for A was 20% too low, and for potential B was 15% too high. However, substrate-mediated effects will reduce the interactions of the adsorbed molecules by about 15%[42,43,44]. This effect was not included in the simulations, so that potential B is perhaps more realistic than potential A for simulations of an adsorbed layer.

Simulations were also attempted on solid CH_3F. However, the crystal structure of solid CH_3F has never been determined by X-ray crystallography. In fact, only IR and Raman spectroscopy experiments have so far been performed on solid CH_3F. From these spectra, it was concluded[130] that solid CH_3Cl has the β–form of CH_3Br (unlike CH_3Cl), or some variant, possibly with eight molecules per unit cell. Therefore, the CH_3F molecules were started in both the α and β structures as described above, after adjustment of the unit cell vectors to give small positive stress tensors. The resulting starting (orthorhombic) unit cells were: 5.9Å×5.1Å×6.8Å for the α-configuration, and 4.4Å×6.8Å×7.4Å for the β-configuration.

As above, the simulations were performed at constant pressure, after a short equilibration run at constant volume. In the simulations of the α–phase with potential B, the system spontaneously deformed into a nearly cubic unit cell of lengths 6.0Å×6.0Å×5.9Å, with all three cell angles equal to 90°. The average potential energy was -19.7kJ/mol at 96K. In the β–structure, the system kept essentially the same unit cell as it began with. In this case, the average potential energy was -18.5kJ/mol at 105K. Since neither potential reproduced the potential energy of the

CH_3Cl structure, it cannot be concluded that either of these structures represents the true structure of CH_3F.

6.5 Methyl Fluoride on Xe/Gr

Helium-beam diffraction experiments have indicated that a layer of solid CH_3F on graphite forms a commensurate $\sqrt{3} \times \sqrt{3}$ R30° (unit cell lengths: 4.26Å×7.38Å) monolayer structure with only one molecule per unit cell[121]. This means that the CH_3F molecules are either all aligned in the same direction, or that they are randomly oriented in the plane of the surface. Experiments on CH_3F/Xe/Gr show that it is also $\sqrt{3} \times \sqrt{3}$ R30° commensurate, but with two molecules per unit cell.

The simulations of CH_3F/Xe/Gr were started in the commensurate structure, and with two different starting orientations: either all standing vertically (C—F bond aligned perpendicular to the surface) arranged in antiferro ordered chains, or all lying down (C—F bond aligned parallel to the surface) in a herringbone. In both cases, the molecules evolved to a structure in which they were all lying down, with their CH_3 ends arranged commensurate with the Xe (in the site between three adjacent Xe atoms). Figures 6.3 and 6.4 show that the molecules were arranged in ferro-ordered zig-zag chains, which is a not uncommon structure for dipolar molecules in 3D. This structure was found to be energetically favored over the vertical antiferro structure. These results perhaps suggest that the structure observed experimentally for CH_3F/Gr is orientationally disordered, accounting for the single molecule per unit cell. Apparently, the corrugation of the graphite is too small to induce orientational

ordering of the CH_3F molecules, but the corrugation of a Xe layer is large enough. This is a possible example of substrate-induced ordering of an overlayer.

The dynamics of the CH_3F/Xe/Gr system was examined by the calculation of the velocity autocorrelation functions for translation and rotation of the Xe atoms and the CH_3F molecules. Figure 6.5 shows the power spectrum for Xe translational motion, and Figure 6.6 shows the power spectra for the motions of the CH_3F molecules. Here, R_Z corresponds to rotation of the molecules about their C—F axes, R_X is rotation about an axis normal to R_Z and in the plane of a C—H bond, and R_Y is rotation about an axis normal to the other two. Analysis of these power spectra shows that the molecular motions are strongly coupled to the Xe layer motions, particularly T_X and T_Z. There is also evidence for translation-rotation coupling between many of the modes. The two most prominent peaks in T_X are also the dominant peaks in R_Z, implying a coupling between rotation about the molecular axis and translation along the direction of the zig-zag chains. Also, the high frequency structure in T_Z is a combination of R_X and R_Y. Since the X and Y axes of the molecules were not constrained to any particular orientation relative to the surface, both contributed to the coupling of the rotation of the molecules about an axis perpendicular to R_Z and parallel to the surface, with T_Z.

6.6 Methyl Chloride on Xe/Gr

Helium-beam diffraction experiments suggest that a solid CH_3Cl forms an uniaxial incommensurate structure on graphite[121,122]. That is, it is commensurate in

one direction, and incommensurate in the other. The lattice constants calculated from the spectrum were: $a = 4.26$Å and $b = 6.38$Å[121,122]. The same experiment on CH_3Cl/Xe/Gr showed no change in the structure from CH_3Cl/Gr[121,122]. This suggests that the relative strengths of the CH_3Cl–CH_3Cl and CH_3Cl-substrate interactions are different than for CH_3F. Apparently, the greater intermolecular interaction for CH_3Cl influences the structure more than the weaker interaction of CH_3F. Indeed, while the dipole moments of CH_3F and CH_3Cl are very similar, the polarizibility of Cl is much larger than F, accounting for this increased strength. As a result, the CH_3Cl molecules form a structure in which they are closer together than the CH_3F molecules, even though CH_3Cl is larger than CH_3F. In the case of CH_3F, the weaker intermolecular potential allows the molecules to be commensurate, even though the equilibrium spacing would be smaller in the absence of the substrate.

The simulations of CH_3Cl/Xe/Gr were also started in two different orientations: either all standing vertically in antiferro-ordered chains, or all lying down in a herringbone. In both cases, the molecules evolved to the antiferro standing structure shown in Figure 6.7, with their CH_3 ends commensurate only in the X-direction. The lattice constants were calculated to be: $a = 4.25$Å and $b = 6.75$Å. Moreover, Figure 6.8 shows that the molecules were tilted about 72° away from the surface, and in the a direction. Except for the large value of b, this structure corresponds well to the experimental spectrum[121,122]. There is also a strong correspondence with the experimental structure of bulk CH_3Cl. The rows of CH_3Cl molecules seen in the 2-D simulations are very similar to the antiferro-ordered chains of the bulk solid. In the bulk, the molecules are aligned 44° from the line of the chains.

As in the CH_3F simulations, the dynamics of the CH_3Cl system was examined by calculation of the appropriate velocity autocorrelation functions for both rotational and center of mass motion. Figure 6.9 shows the power spectrum for Xe atom motions. These spectra are identical to those in Figure 6.5, for the Xe atoms in the CH_3F simulation. The motion of the Xe atoms does not appear to be affected by either the composition or structure of the overlayer. Figure 6.10 shows the power spectra for CH_3Cl motions. Again, the molecular motions were strongly coupled to the motion of the Xe layer, particularly T_Z. The plots also suggest a coupling of T_Y, for $\omega > 20\text{cm}^{-1}$, and T_X, for $\omega < 50\text{cm}^{-1}$ between the Xe and CH_3Cl. The spectra are also very similar to the spectra for CH_3F, in the previous section, but the frequencies are, in general, shifted to lower values. The exceptions are: T_Z, which is coupled to the Z-motion of the Xe layer, and R_Z, rotation about the molecular axis, which has the same moment of inertia for both CH_3F and CH_3Cl. This axis undergoes significant rotational diffusion in both molecules. The values of D_{rotz} were $2.2 \times 10^{-11}\text{s}^{-1}$ for CH_3F, and $3.4 \times 10^{-11}\text{s}^{-1}$ for CH_3Cl, with errors of $\pm 25\%$.

Translational-rotational coupling was similar to that found in CH_3F. The T_Z peak appears in both R_X and R_Y, suggesting a coupling between the rotation of the molecules about axes parallel to the surface, and translation perpendicular to the surface. There is also a correspondence between the spectra for T_X, T_Y, R_X and R_Y near 80cm^{-1}, suggesting that these rotations are also coupled to the translations of the molecule in the plane of the surface.

6.7 Conclusion

The MD simulations have demonstrated that, as in the case for ethane, the corrugation of the substrate can play a major role in the formation of an overlayer structure. In this case, the Xe layers produced a surface with much larger corrugation than bare graphite, and this was enough to overcome the intermolecular attraction of the CH_3F molecules, to force a commensurate structure. For the case of CH_3Cl, the greater interaction energy was enough to overcome the effect of the corrugation, and an incommensurate anti-ferro ordered layer was the result.

Figure 6.1:

View along the a axis of the α-phase structure for CH_3Br. The dashed molecules are separated from the solid molecules by .5a in the direction normal to the plane of the figure. Taken from Reference [131].

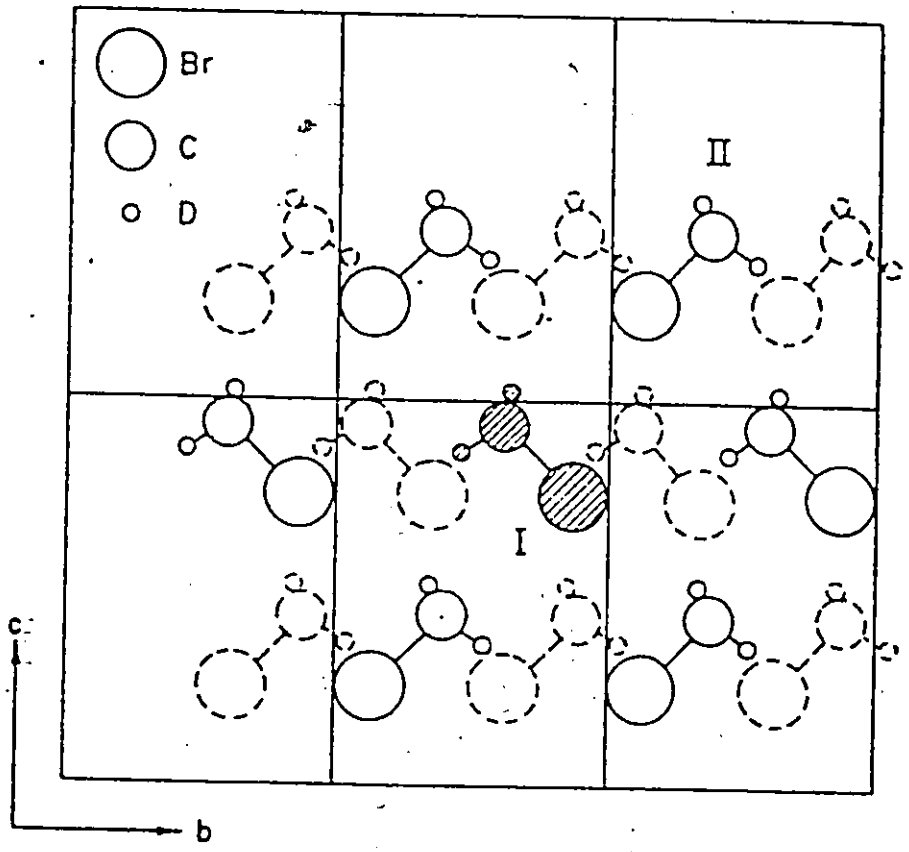

Figure 6.2:

View along the b axis of the β-phase structure for CH_3Br. The dashed molecules are separated from the solid molecules by .5b in the direction normal to the plane of the figure. Taken from Reference [131].

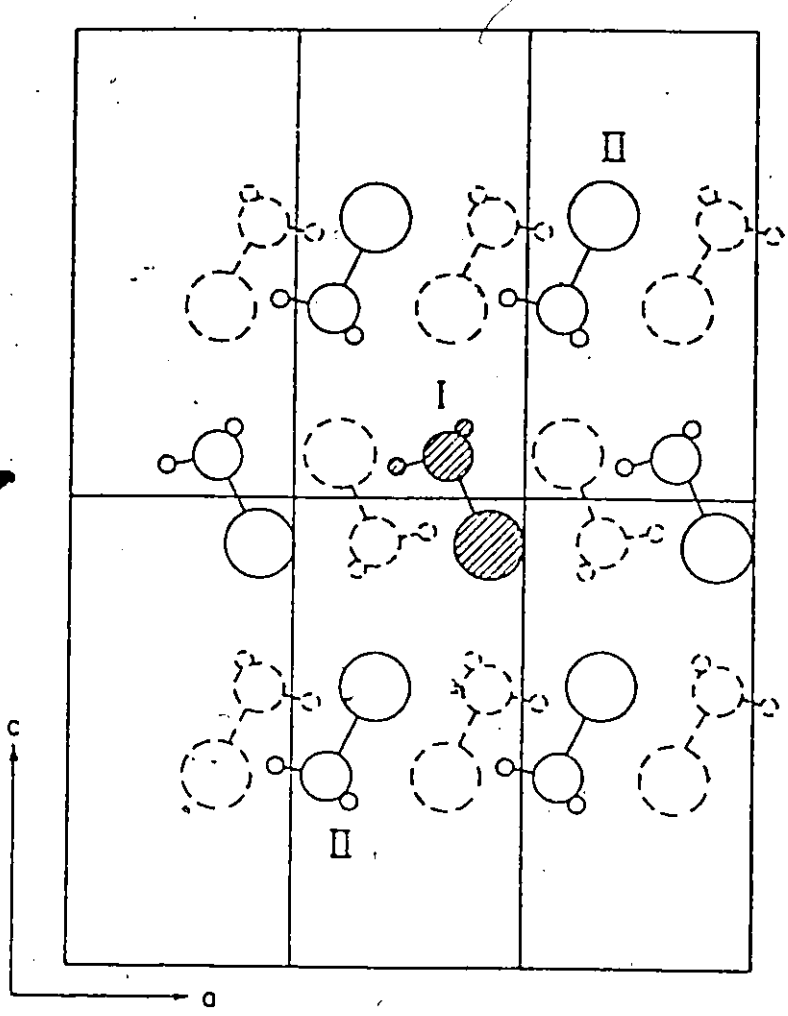

Figure 6.3:

Snapshot (top view) of CH_3F/Xe/Gr system and the end of the simulation. The large circles represent the Xe atoms, and the small circles serve to mark the ends of the molecules containing the F atoms, but are not intended to represent the size of the F atoms.

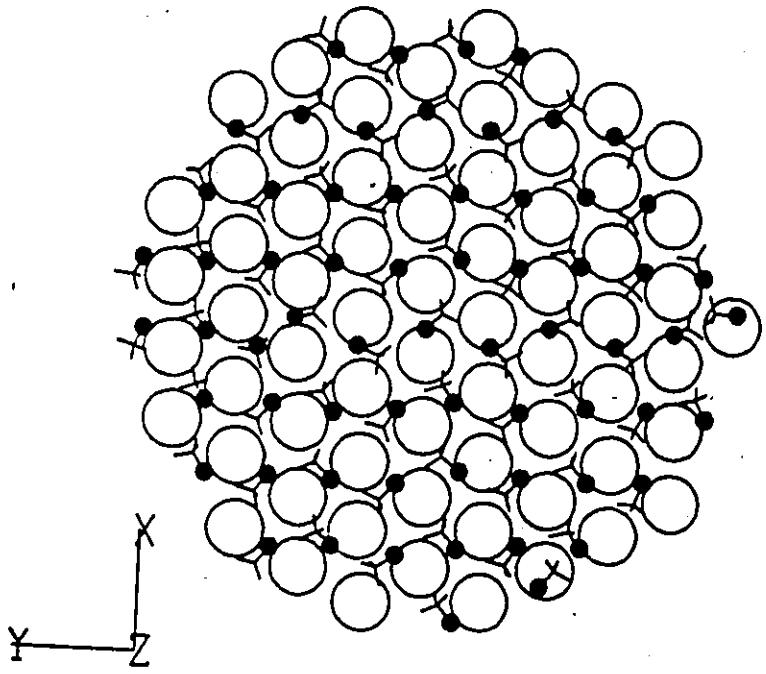

Figure 6.4:

Snapshots (side views) of the CH_3F/Xe/Gr system (a) along X and (b) along Y at the end of the simulation. The large circles represent the Xe atoms, and the small circles serve to mark the ends of the molecules containing the F atoms, but are not intended to represent the size of the F atom. The dots represent the positions of the carbon atoms of the first graphite layer.

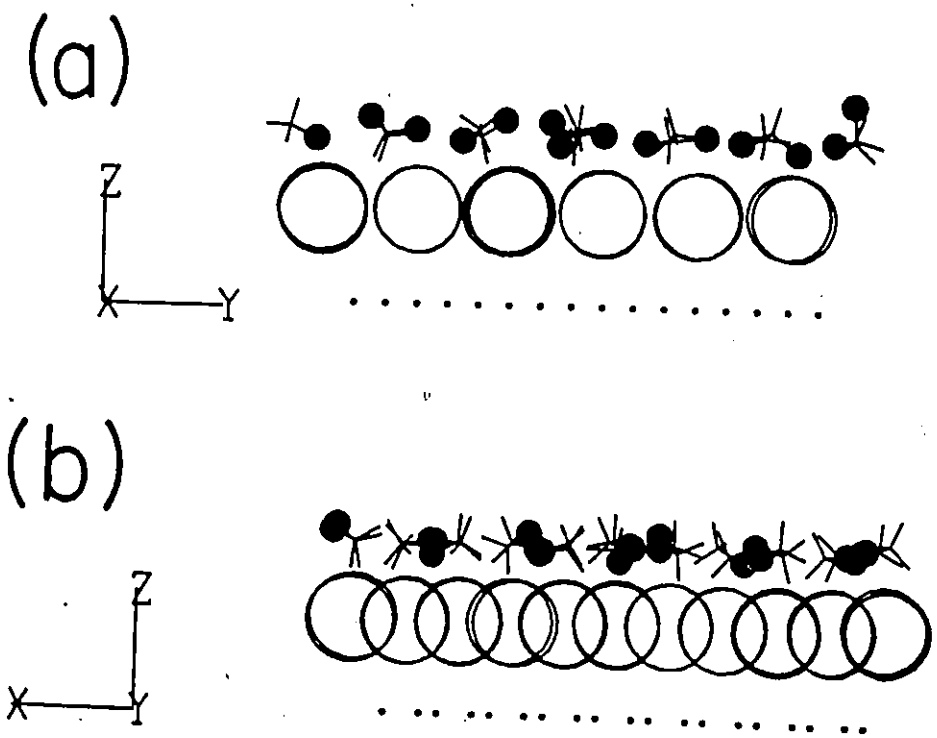

Figure 6.5:

Power spectra for Xe atom motions in the CH_3F/Xe/graphite system. The symbols designate translational motion either parallel (T_X, T_Y) or perpendicular (T_Z) to the graphite basal plane.

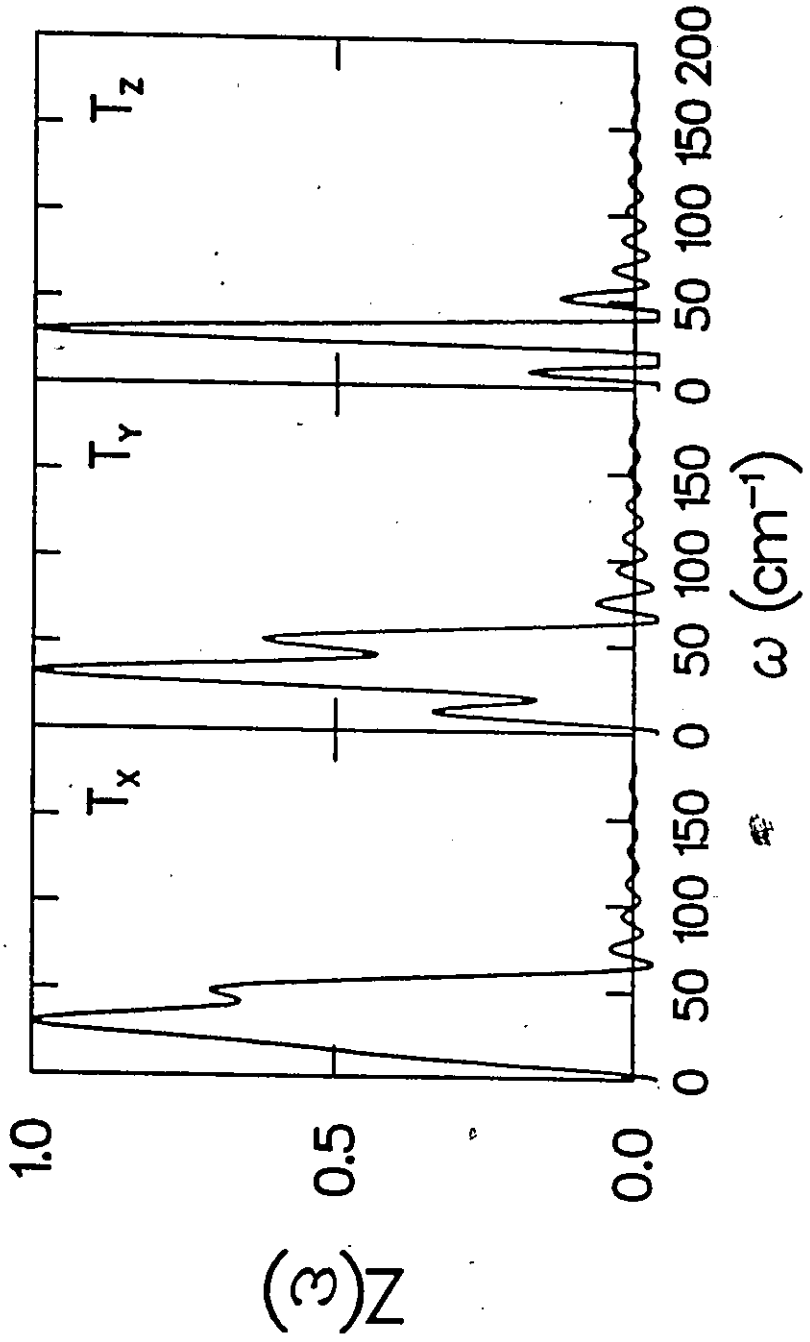

Figure 6.6:

Power spectra for CH_3F molecular motions in the CH_3F/Xe/graphite system. The symbols designate translational motion either parallel (T_X, T_Y) or perpendicular (T_Z) to the graphite basal plane, rotation about the C—F axis (R_Z), about an axis normal to R_Z an in the plane of a C—H bond (R_X), and about a mutually orthogonal axis (R_Y).

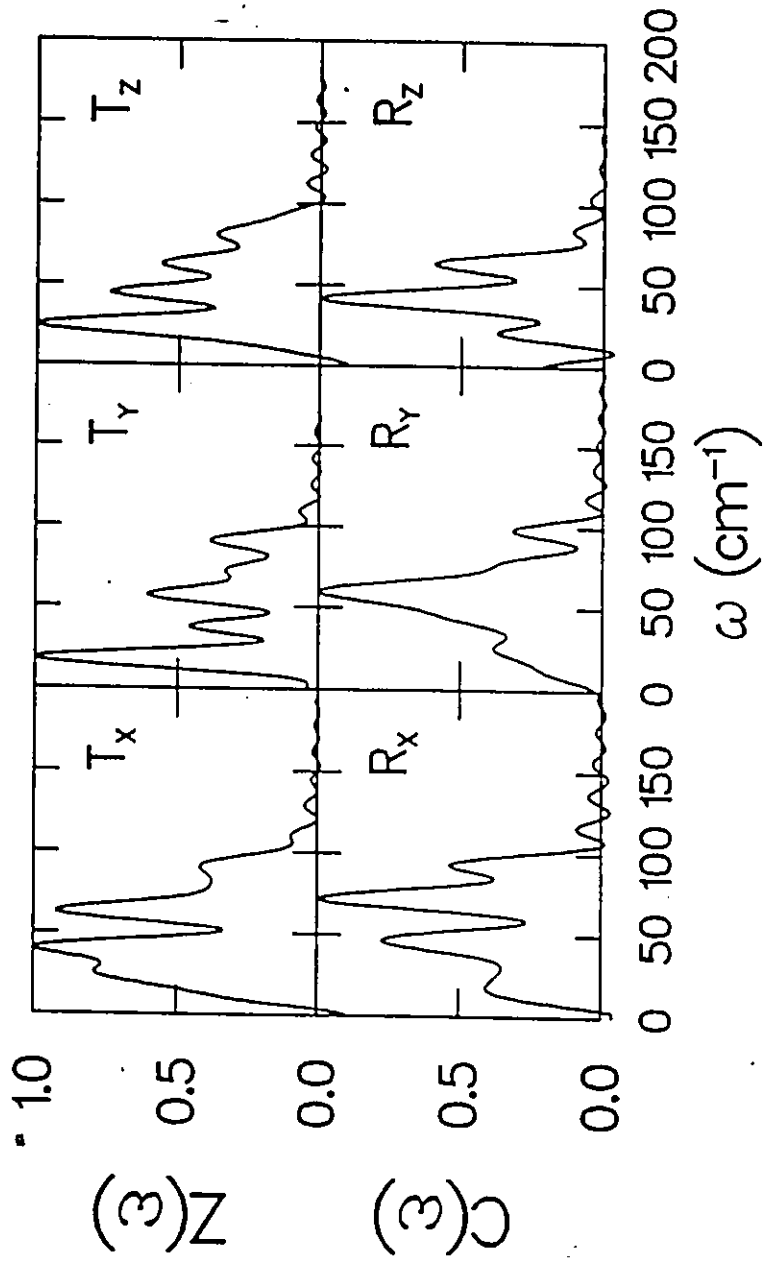

Figure 6.7:

Snapshot (top view) of CH_3Cl/Xe/Gr system and the end of the simulation. The large circles represent the Xe atoms, and the small circles serve to mark the ends of the molecules containing the Cl atoms, but are not intended to represent the size of the Cl atoms.

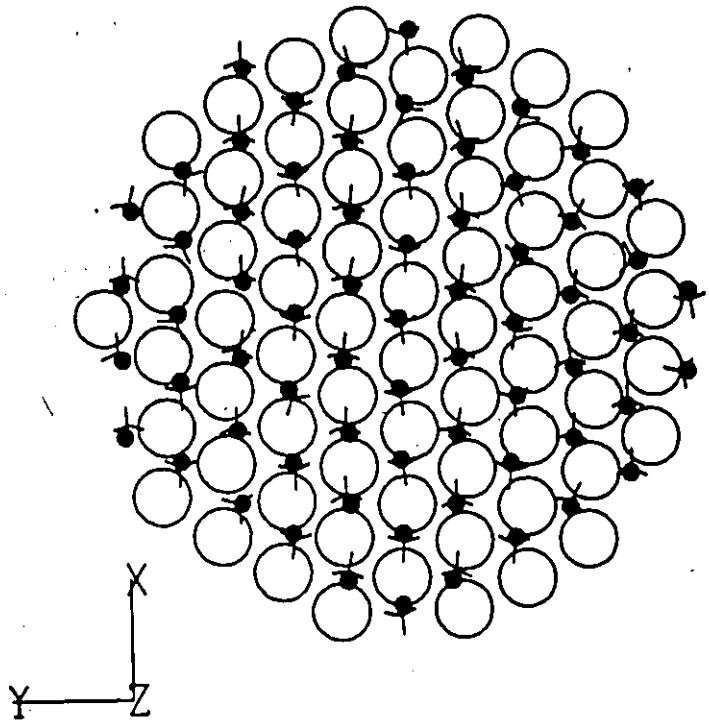

Figure 6.8:

Snapshots (side views) of the CH_3Cl/Xe/Gr system (a) along X and (b) along Y at the end of the simulation. The large circles represent the Xe atoms, and the small circles serve to mark the ends of the molecules containing the Cl atoms, but are not intended to represent the size of the Cl atom. The dots represent the positions of the carbon atoms of the first graphite layer.

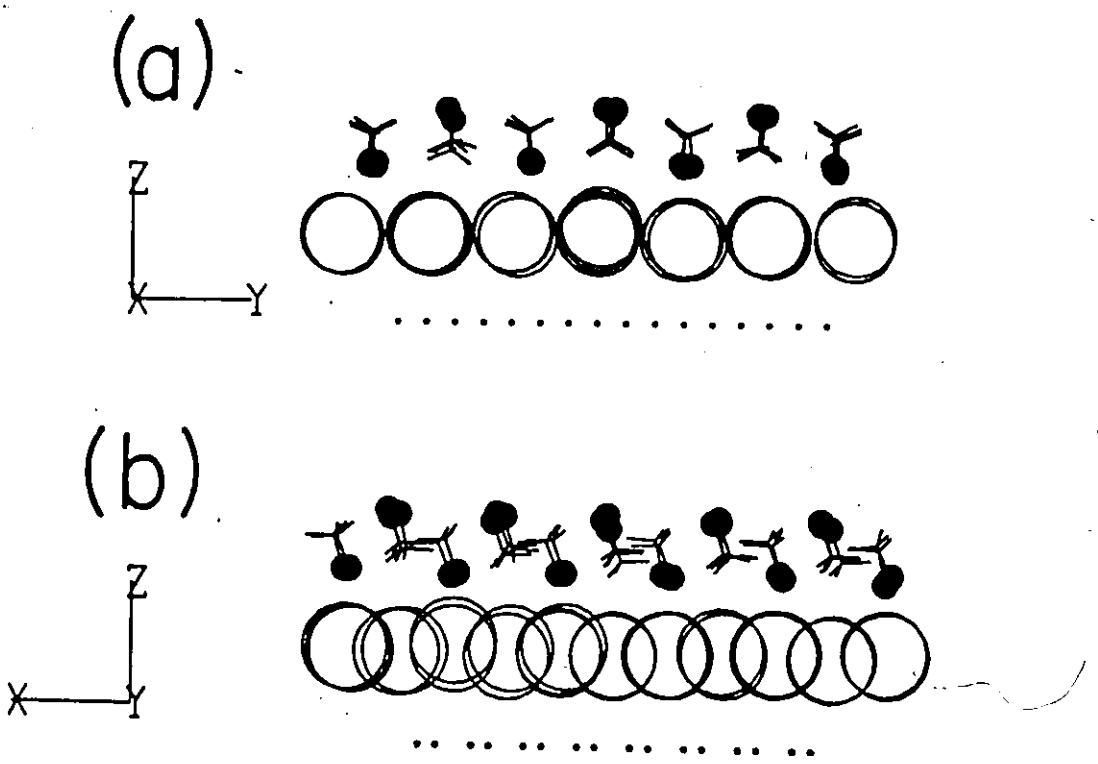

Figure 6.9:

Power spectra for Xe atom motions in the CH_3Cl/Xe/graphite system. The symbols designate translational motion either parallel (T_X, T_Y) or perpendicular (T_Z) to the graphite basal plane.

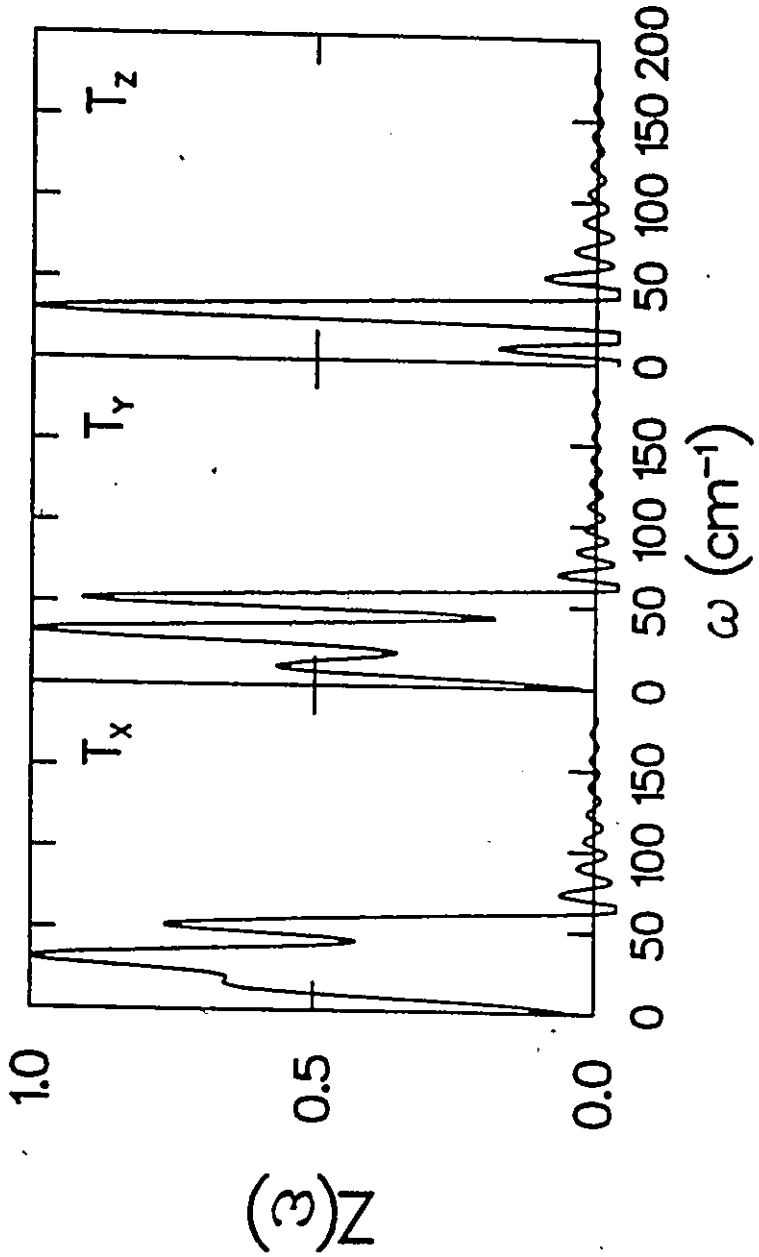

Figure 6.10:

Power spectra for CH_3Cl molecular motions in the CH_3Cl/Xe/graphite system. The symbols designate translational motion either parallel (T_X, T_Y) or perpendicular (T_Z) to the graphite basal plane, rotation about the C—Cl axis (R_Z), about an axis normal to R_Z an in the plane of a C—H bond (R_X), and about a mutually orthogonal axis (R_Y).

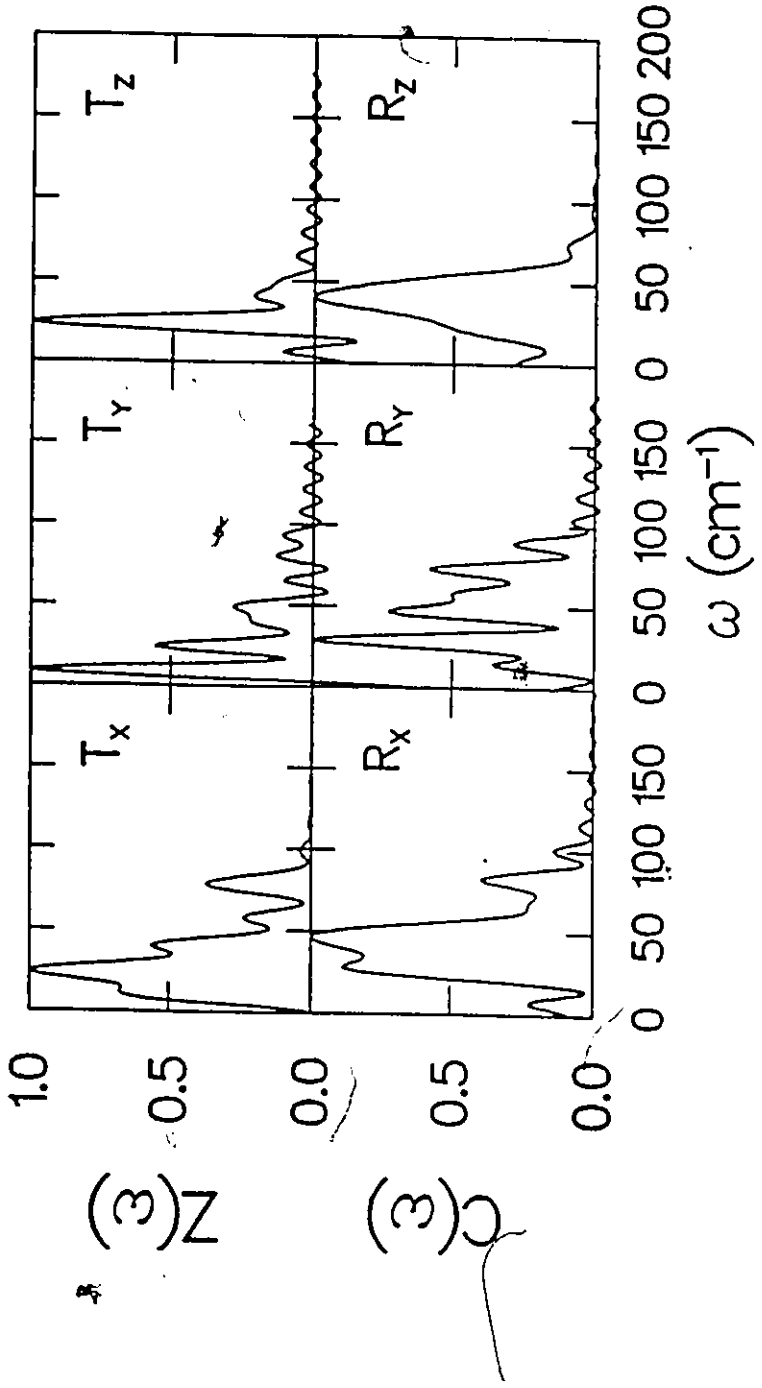

Chapter 7

Conclusions

7.1 Physisorption of Simple Molecules

To help understand the structure and dynamics of single layers of simple molecules adsorbed on graphite, molecular dynamics simulations have been performed on several different systems. The molecules in question were all small hydrocarbons, and their structures on graphite were indeed similar, but differed in detail. The results of the simulations were found to be in excellent agreement with available experimental data.

The translational diffusion coefficient of methane on graphite, which was found to be strongly temperature dependent, agreed well with the experimental data. The components of the rotational diffusion coefficient were equal, indicating that methane is a free rotor in the liquid phase.

In simulations of ethylene on graphite, the corrugation had little effect on

its structures, and the structure in the model was a rectangular solid, in agreement with subsequent experiments. The simulations of the melting suggested that there is a novel effect at the transition, which makes it appear continuous, namely, the standing up of molecules to form local density fluctuations. The melting temperature of the model was too low, and this was attributed to neglect of the anisotropic form of the potential. KTNHY-type melting was apparently not observed in the simulations.

Simulations of ethane on graphite, in contrast to the case of ethylene, found that the structure is stabilized by the corrugation for the S1 phase, and perhaps for the S3 phase. The simulated S2 phase did not form the experimental structure, but one which was very similar. The calculated power spectra for the S1 and S3 phases were in good agreement with neutron scattering experiments, though the S2 frequencies were a bit lower than the experimental values, possibly due to the incorrect structure found.

Simulations of the polar molecules methyl fluoride and methyl chloride complemented helium-beam scattering experiments, by indicating the orientations of the molecular layers, when adsorbed on a Xe layer. The results were unexpected, in that methyl fluoride was found to lie down on the surface, in a series of ferro-aligned zig-zag chains, while the methyl chloride formed a completely different structure: the molecules stood almost vertical to the surface (18° tilt away from the vertical) and formed antiferro-ordered pairs arranged in rows. Here, the corrugation had a profound effect on the structures: it forced the methyl fluoride molecules into a commensurate structure, while the methyl chloride was incommensurate. Somewhat surprisingly, CH_3Cl packed even closer together than methyl fluoride (a smaller

molecule), because of stronger intermolecular interactions relative to the corrugation.

7.2 Suggestions for Future Work

7.2.1 Potentials

Clearly, better potentials are required in order to predict more accurately the properties of the systems studied herein. Also, one of the most pressing needs is for an efficient technique for the summation of long-ranged electrostatic interactions in a pseudo-2D layer. The theory of the McLachlan interaction needs to be extended to molecular systems, for the results presented herein suggest that this interaction is necessary in order to obtain the correct structure and dynamics.

7.2.2 Simulations

Calculations presented in this thesis suggest several areas for future work. Calculations which could be attempted include the simulation of the S_{II} phase of methane, including its "floating" transition, and the lattice fluid phases (I1 and I2) of ethane. Also of importance would be the examination of the melting mechanism for ethane to see if it is similar to ethylene, and simulations of other polar molecules, such as NH_3 or HCl, both on Xe-plated and on bare graphite, to explore the various structural phases exhibited by these systems. It would also be of interest to simulate physisorbed multilayers.

Finally, this thesis has shown that MD is an invaluable complement to "real" experiments (see the results for C_2H_4/graphite and CH_3Cl/Xe/graphite), and it is

certain that this combination will continue to increase in use and importance.

Bibliography

[1] J. G. Dash. *Films on Solid Surfaces.* Academic Press, New York, 1975.

[2] J. G. Dash and J. Ruvald, editors. *Phase Transitions in Surface Films.* Plenum Press, New York, 1979.

[3] W. A. Steele. *The Interaction of Gases with Solid Surfaces.* Oxford Pergamon Press, 1974.

[4] F. F. Abraham, W. E. Rudge, D. J. Auerbach, and S. W. Koch. *Phys. Rev. Lett.*, 52:445, 1984.

[5] F. F. Abraham. *Phys. Rev. Lett.*, 50:978, 1983.

[6] F. F. Abraham. *J. Vac. Sci. Technol.*, B 2:534, 1984.

[7] C. J. Peters. *Physical Adsorption of Simple Linear Molecules on Graphite.* PhD thesis, McMaster University, 1984. (unpublished).

[8] V. R. Bhethanabotla and W. A. Steele. *Langmuir*, 3:581, 1987.

[9] R. D. Diehl, M. F. Toney, and S. C. Fain, Jr. *Phys. Rev. Lett.*, 48:177, 1982.

[10] S. Nosé and M. L. Klein. *Phys. Rev. Lett.*, 53:818, 1984.

[11] J. Suzanne, J. L. Seguin, H. Taub, and J. P. Biberian. *Surf. Sci.*, 125:153, 1983.

[12] A. Terlain, Y. Larher, F. Angerand, G. Parette, H. Lauter, and I. C. Bassignana. *Mol. Phys.*, 58:799, 1986.

[13] J. Krim, J. Suzanne, H. Schechter, R. Wang, and H. Taub. *Surf. Sci.*, 162:446, 1985.

[14] H. Taub. In G. J. Long and F. Grandejean, editors, *The Time Domain in Surface and Structural Dynamics (NATO ASI Series. Series C. Mathematical and Physical Sciences ; Vol. 228)*, page 467, Kluwer Academic Publishers, Dordrecht, 1988.

[15] J. Kushick and B. J. Berne. Molecular dynamics methods: continuous potentials. *Mod. Theor. Chem.*, 6 (Stat Mech Part B):41, 1977.

[16] W. F. van Gunsteren and H. J. C. Berendsen. *Mol. Phys.*, 34:1311, 1977.

[17] M. L. Klein. *Ann. Rev. Phys. Chem.*, 36:525, 1985.

[18] F. F. Abraham. *Adv. Phys.*, 35:1, 1986.

[19] H. J. C. Berendsen and W. F. van Gunsteren. In G. Ciccotti and W. G. Hoover, editors, *Molecular Dynamics Simulation of Statistical-Mechanical Systems*, page 43, North-Holland, Amsterdam, 1986.

[20] M. P. Allen and D. J. Tildesley. *Computer Simulation of Liquids.* Clarendon Press, Oxford, 1987.

[21] L. Verlet. *Phys. Rev.*, 159:98, 1967.

[22] J. P. Ryckaert and G. Ciccotti. *J. Chem. Phys.*, 78:7368, 1983.

[23] M. Ferrario and J. P. Ryckaert. *Mol. Phys.*, 54:587, 1985.

[24] C. W. Gear. *Numerical Initial Value Problems in Ordinary Differential Equations.* Prentice-Hall, Englewood Cliffs, N.J., 1971.

[25] D. J. Evans and S. Murad. *Mol. Phys.*, 34:327, 1977.

[26] H. Goldstein. *Classical Mechanics, 2nd Ed.* Addison-Wesley, Reading, Mass., 1980.

[27] D. Frenkel. In G. Ciccotti and W. G. Hoover, editors, *Molecular Dynamics Simulation of Statistical-Mechanical Systems*, page 151, North-Holland, Amsterdam, 1986.

[28] H. C. Andersen. *J. Chem. Phys.*, 72:2384, 1980.

[29] M. Parrinello and A. Rahman. *Phys. Rev. Lett.*, 45:1196, 1980.

[30] M. Parrinello and A. Rahman. *J. Appl. Phys.*, 52:7182, 1981.

[31] M. Parrinello and A. Rahman. *J. Chem. Phys.*, 76:2662, 1982.

[32] M. Parrinello, A. Rahman, and P. Vashishta. *Phys. Rev. Lett.*, 50:1073, 1983.

[33] S. Nosé. *Mol. Phys.*, 52:255, 1984.

[34] S. Nosé. *J. Chem. Phys.*, 81:511, 1984.

[35] W. G. Hoover. *Molecular Dynamics*, page 1. Springer-Verlag, Berlin, 1986.

[36] J. L. Lebowitz, J. K. Percus, and L. Verlet. *Phys. Rev.*, 153:250, 1967.

[37] W. A. Steele. *Surf. Sci.*, 36:317, 1973.

[38] M. Abramowitz and I. A. Stegun. *Handbook of Mathematical Functions*. Dover Publications, New York, 1964.

[39] J. Belak, K. Kobashi, and R. D. Etters. *Surf. Sci.*, 161:390, 1985.

[40] G. Vidali and M. W. Cole. *Phys. Rev.*, B29:6736, 1984.

[41] Y. P. Joshi and D. J. Tildesley. *Mol. Phys.*, 55:999, 1985.

[42] A. D. McLachlan. *Mol. Phys.*, 7:381, 1964.

[43] S. Rauber, J. R. Klein, M. W. Cole, and L. W. Bruch. *Surf. Sci.*, 123:173, 1982.

[44] L. W. Bruch and J. M. Phillips. *Surf. Sci.*, 91:1, 1980.

[45] F. Y. Hansen. In G. J. Long and F. Grandejean, editors, *The Time Domain in Surface and Structural Dynamics (NATO ASI Series. Series C. Mathematical and Physical Sciences ; Vol. 228)*, page 499, Kluwer Academic Publishers, Dordrecht, 1988.

[46] I. Marlow, R. K. Thomas, and T: D. Trewern. *J. Phys. (Paris)*, 38:C4–19, 1977.

[47] P. Vora, S. K. Sinha, and R. K. Crawford. *Phys. Rev. Lett.*, 43:704, 1979.

[48] A. Glachant, J. P. Coulomb, , M. Bienfait, and J. G. Dash. *J. Phys. (Paris)*, 40:L–453, 1979.

[49] R. Beaume, J. Suzanne, J. P. Coulomb, A. Glachant, and G. Bomchil. *Surf. Sci.*, 137:L117, 1984.

[50] J. M. Gay, A. Dutheil, J. Krim, and J. Suzanne. *Surf. Sci.*, 177:25, 1986.

[51] S. F. O'Shea and M. L. Klein. *J. Chem. Phys.*, 71:2399, 1979.

[52] H. K. Kim, Q. M. Zhang, and M. H. W. Chan. *J. Chem. Soc., Faraday Trans. 2*, to be published, 1988.

[53] J. J. Hamilton and D. L. Goodstein. *Phys. Rev.*, B28:3838, 1983.

[54] J. Piper and J. A. Morrison. *Phys. Rev.*, B30:3486, 1984.

[55] A. Inaba, Y. Koga, and J. A. Morrison. *J. Chem. Soc., Faraday Trans. 2*, 82:1635, 1986.

[56] A. Inaba and J. A. Morrison. *Chem. Phys. Lett.*, 124:361, 1986.

[57] J. Z. Larese, M. Harada, L. Passell, J. Krim, and S. Satija. *Phys. Rev.*, B37:4735, 1988.

[58] M. S. Pettersen, M. J. Lysek, and D. L. Goodstein. *Surf. Sci.*, 175:141, 1986.

[59] S. J. Wang and Y. C. Jean. *Phys. Rev.*, B37:4869, 1988.

[60] J. M. Phillips. *Phys. Rev.*, B34:2823, 1986.

[61] K. Maki and M. L. Klein. *J. Chem. Phys.*, 74:1488, 1981.

[62] E. S. Severin and D. J. Tildesley. *Mol. Phys.*, 41:1401, 1980.

[63] J. M. Phillips. *Phys. Rev.*, B29:5865, 1984.

[64] J. M. Phillips and M. D. Hammerbacher. *Phys. Rev.*, B29:5859, 1984.

[65] J. M. Phillips. *Phys. Rev.*, B29:4821, 1984.

[66] L. W. Bruch. *J. Chem. Phys.*, 87:5518, 1987.

[67] J. Bruno and M. R. Giri. *Phys. Rev.*, B29:5190, 1984.

[68] P. Thorel, J. P. Coulomb, and M. Bienfait. *Surf. Sci.*, 114:L143, 1982.

[69] D. E. Williams. *J. Chem. Phys.*, 45:3770, 1966; "the potential set IV".

[70] J. Suzanne, J. P. Coulomb, and M. Bienfait. *Surf. Sci.*, 44:141, 1974.

[71] J. P. Coulomb, M. Bienfait, and P. Thorel. *J. Phys. (Paris)*, 42:293, 1981.

[72] J. Z. Larese, L. Passell, J. P. Wicksted, A. D. Heidemann, and D. Richter. *Phys. Rev. Lett.*, to be published, 1988.

[73] J. Menaucourt, A. Thomy, and X. Duval. *J. Phys. (Paris) Colloq.*, 38:C4–195, 1977.

[74] H. K. Kim, Q. M. Zhang, and M. H. W. Chan. *Phys. Rev. Lett.*, 56:1579, 1986.

[75] S. K. Satija, L. Passell, J. Eckert, W. Ellenson, and H. Patterson. *Phys. Rev. Lett.*, 51:411, 1983.

[76] B. H. Grier, L. Passell, J. Eckert, H. Patterson, D. Richter, and R. J. Rollefson. *Phys. Rev. Lett.*, 53:814, 1984.

[77] M. Sutton, S. G. J. Mochrie, and R. J. Birgeneau. *Phys. Rev. Lett.*, 51:407, 1983.

[78] S. G. J. Mochrie, M. Sutton, R. J. Birgeneau, D. E. Moncton, and P. M. Horn. *Phys. Rev.*, B30:263, 1984.

[79] Q. M. Zhang, Y. P. Feng, H. K. Kim, and M. H. W. Chan. *Phys. Rev. Lett.*, 57:1456, 1986.

[80] A. Inaba and J. A, Morrison. *Phys. Rev.*, B34:3238, 1986.

[81] J. Z. Larese and R. J. Rollefson. *Surf. Sci.*, 127:L172, 1983.

[82] J. Z. Larese and R. J. Rollefson. *Phys. Rev.*, B31:3048, 1985.

[83] J. Z. Larese, L. Passell, and B. Ravel. *Can. J. Chem.*, 66:633, 1988.

[84] M. L. Klein and J. A. Morrison. *Carbon*, 25:23, 1987.

[85] S. Nosé and M. L. Klein. *Phys. Rev. Lett.*, 50:1207, 1983.

[86] S. Nosé and M. L. Klein. *Mol. Phys.*, 50:1055, 1983.

[87] J. M. Kosterlitz and D. J. Thouless. *J. Phys. C.*, 6:1181, 1972.

[88] D. R. Nelson and B. I. Halperin. *Phys. Rev.*, B19:2457, 1979.

[89] D. A. Young. *Phys. Rev.*, B19:1855, 1979.

[90] K. T. Strandburg. *Rev. Mod. Phys.*, 60:161, 1988.

[91] H. K. Kim and M. H. W. Chan. *Phys. Rev. Lett.*, 53:170, 1984.

[92] A. D. Migone, Z. R. Li, and M. H. W. Chan. *Phys. Rev. Lett.*, 53:810, 1984.

[93] E. D. Specht, R. J. Birgeneau, K. L. D'Amico, D. E. Moncton, S. E. Nagler, and P. M. Horn. *J. Phys. Lett.*, 46:L561, 1985.

[94] S. E. Nagler, P. M. Horn, T. F. Rosenbaum, R. J. Birgeneau, M. Sutton, S. G. J. Mochrie, D. E. Moncton, and R. Clarke. *Phys. Rev.*, B32:7373, 1985.

[95] S. Zhang and A. D. Migone. *Private Communication*, 1988.

[96] H. Taub, G. J. Trott, H. R. Danner F. Y. Hansen, J. P. Coulomb, J. P. Biberian, J. Suzanne, and A. Thomy. In S. K. Sinha, editor, *Ordering in Two Dimensions*, page 91, North-Holland, New York, 1980.

[97] J. P. Biberian, J. P. Coulomb, J. Suzanne, G. J. Trott, H. Taub, F. Y. Hansen, and H. R. Danner. In D. A. Degras and M. Costa, editors, *Proceedings of the Fourth International Conference on Solid Surfaces and Third European Conference on Surface Science, Cannes, France*, 1980. [Le Vide Les Couches Minces **201**, 126 (1980)].

[98] J. P. Coulomb. PhD thesis, l'Université D'Aix Marseille II, 1981. (unpublished).

[99] G. J. Trott. PhD thesis, University of Missouri-Columbia, 1981. (unpublished).

[100] J. P. Coulomb and M. Bienfait. *Discuss. Faraday Soc.*, 80:79, 1985.

[101] M. Bienfait. In Jean Lascombe, editor, *Proceedings of the 41st International Meeting of the Societe Francaise de Chemie, Division de Chemie Physique, Grenoble*, page 353, Elsevier, Amsterdam, 1986.

[102] J. P. Coulomb and M. Bienfait. *J. Phys. (Paris)*, 47:89, 1986.

[103] F. Y. Hansen and H. Taub. *J. Chem. Phys.*, 87:3232, 1987.

[104] J. Suzanne, J. M. Gay, and R. Wang. *Surf. Sci.*, 162:439, 1985.

[105] J. M. Gay, J. Suzanne, and R. Wang. *J. Chem. Soc., Faraday Trans. 2*, 82:1669, 1986.

[106] J. W. Osen and S. C. Fain, Jr. *Phys. Rev.*, B36:4074, 1987.

[107] J. Talbot, D. J. Tildesley, and W. A. Steele. *Mol. Phys.*, 51:1331, 1984.

[108] S. C. Fain, Jr. *Private Communication*, 1988.

[109] A. D. Buckingham, C. Graham, and J. H. Williams. *Mol. Phys.*, 49:703, 1983.

[110] J. W. Osen and S. C. Fain, Jr. *J. Vac. Sci. Technol.*, A6:768, 1988.

[111] L. Battezzati, C. Pisani, and F. Ricca. *J. Chem. Soc., Faraday Trans. 2*, 71:1629, 1975.

[112] S. C. Fain, Jr., M. F. Toney, and R. D. Diehl. In J. L. deSegovia, editor, *Proceedings of the Ninth International Vacuum Congress and Fifth International Conference on Solid Surfaces*, page 129, Imprenta Moderna, Madrid, 1983.

[113] A. G. Bezus, V. P. Dreving, and A. V. Kiselev. *Russ. J. Phys. Chem.*, 38:30, 1964.

[114] J. M. Gay. PhD thesis, l'Université D'Aix-Marseille II, 1987. (unpublished).

[115] A. D. Buckingham, M. P. Bogaard, D. A. Dunmur, C. P. Hobbs, and B. J. Orr. *Trans. Faraday Soc.*, 66:1548, 1970.

[116] M. A. Moller and M. L. Klein. *Can. J. Chem.*, 66:774, 1988.

[117] B. F. Mason and B. R. Williams. *J. Chem. Phys.*, 56:1895, 1971.

[118] H. Weichert, E. Maus, and K. Knorr. *Jap. Jour. Appl. Phys.*, 26.3:889, 1987.

[119] K. Knorr and H. Weichert. *Phys. Rev.*, B37:3524, 1988.

[120] S. M. Clarke and R. K. Thomas. Studies in physical and theoretical chemistry. In *Dynamics of Molecular Crystals*, page 365, Elsevier, Amsterdam, 1987.

[121] J. C. Ruiz-Suarez. *Low Energy He Diffraction From Physisorbed Overlayers.* PhD thesis, University of Waterloo, 1987. (unpublished).

[122] J. C. Ruiz-Suarez, M. L. Klein, M. A. Moller, P. A. Rowntree, G. Scoles, and J. Xu. *Phys. Rev. Lett.*, 61:710, 1988.

[123] H. J. Böhm, R. Ahlrichs, P. Scharf, and H. Schiffer. *J. Chem. Phys.*, 81:1389, 1984.

[124] H. J. Böhm, C. Meissner, and R. Ahlrichs. *Mol. Phys.*, 53:651, 1984.

[125] A. Bondi. *J. Phys. Chem.*, 68:441, 1964.

[126] W. L. Jorgensen. *J. Am. Chem. Soc.*, 103:335, 1981.

[127] S. Nosé and M. L. Klein. *J. Chem. Phys.*, 78:6928, 1983.

[128] I. R. McDonald, D. G. Bounds, and M. L. Klein. *Mol. Phys.*, 45:521, 1982.

[129] R. D. Burbank. *J. Am. Chem. Soc.*, 75:1211, 1953.

[130] O. S. Binbrek, A. Anderson, and B. H. Torrie. *J. Raman Spectr.*, 16:185, 1985.

[131] P. N. Gerlach, B. H. Torrie, and B. M. Powell. *Mol. Phys.*, 57:919, 1986.